Computational Fluid Dynamic and Rotordynamic Study on the Labyrinth Seal

Rui Gao

Dissertation submitted to the faculty of the Virginia Polytechnic Institute and State University in partial fulfillment of the requirements for the degree of

Doctor of Philosophy
In
Mechanical Engineering

Robley G. Kirk, Chair
Mary E. Kasarda
Luther G. Kraige
Brian Vick
Robert L. West

June 14, 2012
Blacksburg, VA

Keywords: CFD, rotordynamics, pre-swirl, labyrinth seal

Computational Fluid Dynamic and Rotordynamic Study on the Labyrinth Seal

Rui Gao

Abstract

The labyrinth seal is widely used in turbo machines to reduce leakage flow. The stability of the rotor is influenced by the labyrinth seal because of the driving forces generated in the seal. The working fluid usually has a circumferential velocity component before entering the seal; the ratio of circumferential velocity and shaft synchronous surface velocity is defined as pre-swirl rate. It has been observed that pre-swirl rate is an important factor affecting driving forces in the labyrinth seal thus affecting the stability of the rotor. Besides the pre-swirl, the eccentricity, the clearance, and the configuration of tooth locations are all factors affecting the rotordynamic properties of the labyrinth seal. So it is of interest to investigate the exact relationships between those factors and the seal's rotordynamic properties.

In this research, three types of labyrinth seals have been modeled: the straight eye seal, the stepped eye seal, and the balance drum seal. For the straight eye seal, a series of models were built to study the influence of eccentricity and clearance. The other two seals each have only one model. All models were built with Solid Works and meshed with ANSYS-ICEM. Flows in those models were simulated by numerically solving the Reynolds-Averaged Navier-Stokes (RANS) equations in the ANSYS-CFX and then rotordynamic coefficients for each seal were calculated based on the numerical results.

It had previously been very difficult to generate a pre-swirl rate higher than 60% in a numerical simulation. So three ways to create pre-swirl in ANSYS-CFX were studied and finally the method by specifying the inlet velocity ratio was employed. Numerical methods used in this research were introduced including the frame transfer, the k-ε turbulence model with curvature correction, and the scalable wall function. To obtain the optimal mesh and minimize the

discretization error, a systematical grid study was conducted including grid independence studies and discretization error estimations. Some of the results were compared with previous bulk-flow or experimental results to validate the numerical model and method.

The fluid field in the labyrinth seal must be analyzed before conducting rotordynamic analysis. The predicted pressure distributions and leakages were compared with bulk-flow results. A second small vortex at the downstream edge of each tooth was found in the straight eye seal. This has never been reported before and the discovery of this small vortex will help to improve seal designs in the future. The detailed flows in discharged region and in chambers were also discussed.

Radial and tangential forces on the rotor were solved based on the fluid field results. It is shown that the traditional first-order rotordynamic model works well for low pre-swirl cases but does not accurately reflect the characteristics for high pre-swirl cases. For example compressor eye seals usually have pre-swirl rates bigger than 70% and the second order model is required. Thus a second-order model including inertia terms was built and applied to the rotordynamic analysis in this research. The influence of pre-swirl, eccentricity and clearance were studied using the straight eye seal model. The rotordynamic characteristics of the stepped eye seal and the balance drum seal were studied considering high pre-swirl rates. Some relationships between influencing factors and the four rotordynamic coefficients were concluded. The results also showed that for all the three seals higher pre-swirl leads to higher cross-coupled stiffness which is one of the main factors causing rotor instability.

The rotor stability analysis was conducted to study the influence of drum balance seal on the stability. The rotor was designed with typical dimensions and natural frequencies for a centrifugal compressor rotor. The parameters for bearing and aerodynamic force were also set according to general case in compressors to minimize the effects from them. The result shows that the high pre-swirl rate in balance drum seal leads to rotor instability, which confirmed the significant effect of pre-swirl on the seal and the rotor system.

Acknowledgements

I would like to thank my advisor Dr. R. Gordon Kirk for his support during the entire study for my PhD and his guidance on my research. Also thanks to his imparting vast rotordynamic knowledge and industrial experience on me.

I am also very grateful to Dr. Mary Kasarda, Dr. Robert West, Dr. Brian Vick, and Dr. Glenn Kraige for serving in my degree committee and their advices on my dissertation. This dissertation would not have been possible without the encouragement and guidance of my advisor and other professors in my committees.

In addition, I am very thankful to the faculty and staff in the Mechanical Engineering Department, such as Ben Poe, Cathy Hill, and many others, for their support and help in different aspects.

Table of Contents

Abstract ..... **ii**

Acknowledgements ..... **iv**

Table of Contents ..... **v**

List of Figures ..... **viii**

List of Tables ..... **xiv**

Nomenclature ..... **xvi**

1 Introduction **1**

1.1 Background and Motivation 1

1.1.1 Introduction to the Labyrinth Seal 1

1.1.2 Motivation of the Research 2

1.1.3 Definition of Pre-swirl Rate 3

1.1.4 Labyrinth Seals to Study 4

1.2 Literature Review 5

1.3 Aims and Objects 11

1.4 Dissertation Outline 11

2 Numerical Method and Model **14**

2.1 Frame Transfer 14

2.2 Numerical Methods 15

2.2.1 The k-ε Turbulence Model 15

2.2.2 Curvature Correction 17

2.2.3 Scalable Wall Function 18

2.2.4 Assumptions 21

2.3 Generation of Pre-swirl 22

2.3.1 Inlet Path with Special Shapes or Extra Teeth 22
2.3.2 Rough and Long Inlet Path 23
2.3.3 Ratio of Inlet Velocities 24
2.4 Computational Models 25
2.4.1 Straight Labyrinth Eye Seal 25
2.4.2 Stepped Labyrinth Eye Seal 27
2.4.3 Balance Drum Labyrinth Seal 29
2.5 Meshing Scheme 31
2.5.1 Grid Independence Study 31
2.5.2 Discretization Error Estimation 34
2.6 Verification of Model and Method 38
2.6.1 Comparison for the Straight Eye Seal 38
2.6.2 Comparison for the Stepped Eye Seal 40
2.7 Summary 43

3 Fluid Field Result Analysis 44
3.1 Pressure Distribution 44
3.2 Leakage 46
3.3 Flow Details 48
3.3.1 The Small Vortex 48
3.3.2 The Discharge Region 50
3.3.3 The Spiral Flow in Chambers 51
3.4 Summary 52

4 Rotordynamic Coefficients Prediction 53
4.1 The First-Order Rotordynamic Model 53
4.2 The Second-Order Rotordynamic Model 54
4.3 Q-Factor 56
4.4 Tooth-on-Stator Straight Eye Seal 57
4.4.1 Pre-Swirl 57
4.4.2 Eccentricity 60
4.4.3 Clearance 65

4.5 Tooth-on-Rotor Straight Eye Seal 70
4.6 Stepped Eye Seal 73
4.7 Balance Drum Seal 76
4.8 Summary 79

5 Rotor Stability Analysis 81
5.1 Equation of Motion and Logarithmic Decrement 81
5.2 The Rotor-Bearing-Seal System 83
5.2.1 The Compressor Rotor 83
5.2.2 The Tilting Pad Bearing 83
5.2.3 The Aerodynamic Force 84
5.2.4 The Balance Drum Seal 85
5.3 Stability Analysis 85
5.4 Summary 87

6 Conclusions 88
6.1 Summary of Results 88
6.2 Future Work 89

References 90

Appendix A—Grid Study 95
A1.1 Grid Study on the Stepped Eye Seal 95
A1.2 Grid Study on the Balance drum Seal 99

Appendix B—Predicted Seal Coefficients 104

List of Figures

Page

Figure 1-1 Cross section view of a centrifugal compressor 1

Figure 1-2 Labyrinth Types 2

Figure 1-3 Illustration of pre-swirl rate 4

Figure 1-4 Typical compressor eye seal and balance drum seal 4

Figure 2-1 Frame transfer from stationary to rotating 14

Figure 2-2 Law of the wall 19

Figure 2-3 A combined application of reducing diameter inlet and extra teeth 23

Figure 2-4 Pre-swirl rate *vs*. length of inlet path at different roughness 23

Figure 2-5 Illustration of specifying inlet velocities 24

Figure 2-6 Dimensions of the straight labyrinth seal (tooth on stator) 25

Figure 2-7 3-D model of the straight eye seal 26

Figure 2-8 Dimension of the stepped labyrinth seal 27

Figure 2-9 3-D model of the stepped eye seal 28

Figure 2-10 Dimension of the balance drum seal 29

Figure 2-11 3-D model of the balance drum seal 30

Figure 2-12 Node numbers in radial and axial direction 32

Figure 2-13 Grid independence study of nodes at tooth tip for the stepped eye seal 33

Figure 2-14 Grid independence study of nodes at chamber for the stepped eye seal 33

Figure 2-15 Mesh used for straight labyrinth eye seal 34

Figure 2-16 Axial velocity profile at the 1st tooth and errors 36

Figure 2-17 Radial velocity profile at the 1st tooth and errors 36

Figure 2-18 Tangential velocity profile at the 1st tooth and errors 37

Figure 2-19 Pressure profile at the 1st tooth and errors 37

Figure 2-20 Comparison of predicted pressure distribution 39

Figure 2-21 Comparison of predicted radial force with previous work (tooth-on-stator, 10% eccentricity, 3% pre-swirl) 39

Figure 2-22 Comparison of predicted tangential force with previous work (tooth-on-stator, 10% eccentricity, 3% pre-swirl) 40

Figure 2-23 Comparison of leakage for the stepped eye seal 41

Figure 2-24 Comparison direct stiffness for the stepped eye seal 42

Figure 2-25 Comparison of cross-coupled stiffness for the stepped eye seal 42

Figure 3-1 Comparison of predicted pressure distribution for the stepped seal 45

Figure 3-2 Comparison of predicted pressure distribution for the balance drum seal 45

Figure 3-3 Predicted leakage *vs*. pre-swirl at different whirl speeds for the straight eye seal (tooth-on-stator, 0.1 eccentricity, 292 μm clearance) 46

Figure 3-4 Predicted leakage *vs*. pre-swirl at different whirl speed for the straight eye seal (tooth-on-rotor, 0.1 eccentricity, 292 μm clearance) 47

Figure 3-5 Predicted stream lines and vectors in the last chamber (tooth-on-stator, 73.6% pre-swirl rate) 48

Figure 3-6 Predicted stream lines and vectors in the last chamber (tooth-on-rotor, 75.3% pre-swirl rate) 49

Figure 3-7 Predicted vectors in the last chamber for the stepped and balance drum seals..... 49

Figure 3-8 The difference of velocities leaving the seal at high eccentricity 50

Figure 3-9 3-D Stream lines in chambers (tooth-on-stator, 73.6% pre-swirl rate) 51

Figure 3-10 3-D Stream lines in chambers (tooth-on-rotor, 75.3% pre-swirl rate) 51

Figure 4-1 Whirl of the rotor 53

Figure 4-2 Predicted radial seal force *vs*. whirl speed at different pre-swirl rates (tooth-on-stator, 0.1 eccentricity)..... 55

Figure 4-3 Predicted tangential seal force *vs*. whirl speed at different pre-swirl rates (tooth-on-stator, 0.1 eccentricity)..... 55

Figure 4-4 Predicted radial seal force *vs*. whirl speed at different pre-swirl rates (tooth-on-stator, 0.1 eccentricity)..... 58

Figure 4-5 Predicted tangential seal force *vs*. whirl speed at different pre-swirl rates (tooth-on-stator, 0.1 eccentricity)..... 58

Figure 4-6 Predicted stiffness *vs*. pre-swirl rate (tooth-on-stator, 0.1 eccentricity) 59

Figure 4-7 Predicted damping *vs*. pre-swirl rate (tooth-on-stator, 0.1 eccentricity)..... 59

Figure 4-8 Q-Factor *vs*. pre-swirl rate (tooth-on-stator, 0.1 eccentricity) 60

Figure 4-9 Predicted radial seal force *vs*. whirl speed at different eccentricities (tooth-on-stator, 3.0% pre-swirl rate) 61

Figure 4-10 Predicted tangential seal force *vs*. whirl speed at different eccentricities (tooth-on-stator, 3.0% pre-swirl rate)..... 61

Figure 4-11 Predicted radial seal force *vs*. whirl speed at different eccentricities (tooth-on-stator, 73.6% pre-swirl rate) 62

Figure 4-12 Predicted tangential seal force *vs*. whirl speed at different eccentricities (tooth-on-stator, 73.6% pre-swirl rate)..... 62

Figure 4-13 Predicted direct stiffness vs. eccentricity (tooth-on-stator)..... 63

Figure 4-14 Predicted cross-coupled stiffness *vs*. eccentricity (tooth-on-stator)..... 63

Figure 4-15 Predicted cross-coupled damping *vs*. eccentricity (tooth-on-stator)..... 64

Figure 4-16 Predicted direct damping *vs*. eccentricity (tooth-on-stator)..... 64

Figure 4-17 Predicted radial seal force *vs*. whirl speed at different clearance (tooth-on-stator, 0.1 eccentricity, 9.7% pre-swirl rate)..... 66

Figure 4-18 Predicted tangential seal force *vs*. whirl speed at different clearance (tooth-on-stator, 0.1 eccentricity, 9.7% pre-swirl rate)..... 66

Figure 4-19 Predicted radial seal force *vs*. whirl speed at different clearance (tooth-on-stator, 0.1 eccentricity, 73.6% pre-swirl rate)..... 67

Figure 4-20 Predicted tangential seal force *vs*. whirl speed at different clearance (tooth-on-stator, 0.1 eccentricity, 73.6% pre-swirl rate)..... 67

Figure 4-21 Predicted direct stiffness *vs*. clearance (tooth-on-stator, 0.1 eccentricity)..... 68

Figure 4-22 Predicted cross-coupled stiffness *vs*. clearance (tooth-on-stator, 0.1 eccentricity).. 68

Figure 4-23 Predicted direct damping *vs*. clearance (tooth-on-stator, 0.1 eccentricity)..... 69

Figure 4-24 Predicted cross-coupled damping *vs*. clearance (tooth-on-stator, 0.1 eccentricity). 69

Figure 4-25 Predicted radial seal force *vs*. whirl speed at different pre-swirl rates (tooth-on-rotor, 0.1 eccentricity)..... 71

Figure 4-26 Predicted tangential seal force *vs*. whirl speed at different pre-swirl rates (tooth-on-rotor, 0.1 eccentricity)..... 71

Figure 4-27 Predicted stiffness *vs*. pre-swirl rate (0.1 eccentricity)..... 72

Figure 4-28 Predicted damping *vs*. pre-swirl rate (0.1 eccentricity)..... 72

Figure 4-29 Q-Factor *vs*. pre-swirl rate (0.1 eccentricity) 73

Figure 4-30 Predicted direct stiffness *vs*. pre-swirl rate (stepped eye seal, 0.1 eccentricity) 74

Figure 4-31 Predicted cross-coupled stiffness *vs*. pre-swirl rate (stepped eye seal, 0.1 eccentricity)..... 74

Figure 4-32 Predicted stiffness *vs*. pre-swirl rate (stepped eye seal, 0.1 eccentricity) 75

Figure 4-33 Predicted damping *vs*. pre-swirl rate (stepped eye seal, 0.1 eccentricity)..... 75

Figure 4-34 Predicted direct stiffness *vs*. pre-swirl rate (balance drum seal 0.1 eccentricity) 77

Figure 4-35 Predicted cross-coupled stiffness *vs*. pre-swirl rate (balance drum seal 0.1 eccentricity)..... 77

Figure 4-36 Predicted stiffness *vs*. pre-swirl rate (balance drum seal, 0.1 eccentricity) 78

Figure 4-37 Predicted damping *vs*. pre-swirl rate (balance drum seal, 0.1 eccentricity)..... 78

Figure 4-38 Q-Factor *vs*. pre-swirl rate (balance drum seal, 0.1 eccentricity) 79

Figure 5-1 Finite element model of the rotor-bearing-seal system..... 83

Figure 5-2 The tilting pad bearing 84

Figure 5-3 Stability map of the rotor system with 13.6% pre-swirl balance drum seal 86

Figure 5-4 Stability map of the rotor system with 75.0% pre-swirl balance drum seal 86

Figure 5-5 Unstable mode (1^{st} mode, forward precession)..... 87

Figure A1-1 Grid independence study of nodes at tooth tip for the stepped eye seal 95

Figure A1-2 Grid independence study of nodes at chamber for the stepped eye seal..... 96

Figure A1-3 Axial velocity profile at the 1^{st} tooth and errors for the stepped eye seal..... 97

Figure A1-4 Radial velocity profile at the 1^{st} tooth and errors for the stepped eye seal 97

Figure A1-5 Tangential velocity profile at the 1st tooth and errors for the stepped eye seal..... 98

Figure A1-6 Pressure profile at the 1st tooth and errors for the stepped eye seal 98

Figure A1-7 Mesh used for the stepped eye seal 99

Figure A1-8 Grid independence study of nodes at tip for the balance drum seal..... 99

Figure A1-9 Grid independence study of nodes at chamber for the balance drum seal 100

Figure A1-10 Axial velocity profile at the 1st tooth and errors for the balance drum seal 101

Figure A1-11 Radial velocity profile at the 1st tooth and errors for the balance drum seal..... 101

Figure A1-12 Tangential velocity profile at the 1st tooth and errors for the balance drum seal 102

Figure A1-13 Pressure profile at the 1st tooth and errors for the balance drum seal 102

Figure A1-14 Mesh used for the balance drum seal for the balance drum seal..... 103

List of Tables

Page

Table 2-1 Assumptions and models in the simulation 22

Table 2-2 Boundary conditions for the straight eye seal 26

Table 2-3 Boundary conditions for the stepped eye seal 28

Table 2-4 Boundary conditions for the balance drum seal 30

Table 2-5 Nodes in circumferential direction required to converge 31

Table 2-6 Comparison of the three meshes in each chamber for the straight eye seal 34

Table 2-7 Summary on the error estimation results 38

Table 3-1 Comparison of predicted leakage with bulk-flow result 47

Table 4-1 Rotordynamic coefficients for the straight eye seal (0.1 eccentricity and 292μm clearance) 56

Table 5-1 Rotordynamic coefficients input for the aerodynamic force 84

Table 5-2 Rotordynamic coefficients input for the balance drum seal 85

Table A1-1 Comparison of the three meshes in each chamber for the stepped eye seal 96

Table A1-2 Comparison of the three meshed in each chamber for the balance drum seal 100

Table A2-1 Predicted rotordynamic coefficients at different pre-swirl rates (tooth-on-stator, 0.1 eccentricity) 104

Table A2-2 Predicted rotordynamic coefficients at different eccentricities (tooth-on-stator) 104

Table A2-3 Predicted rotordynamic coefficients at different clearances (tooth-on-stator, 0.1 eccentricity).....105

Table A2-4 Predicted rotordynamic coefficients at different pre-swirl rates (tooth-on-rotor, 0.1 eccentricity).....105

Table A2-5 Predicted rotordynamic coefficients at different pre-swirl rates (Stepped Eye Seal) 106

Table A2-6 Predicted rotordynamic coefficients at different pre-swirl rates (Balance Drum Seal) 106

Nomenclature

English Symbols

C	direct damping
$C_{\varepsilon 1}$	k-ε turbulence model constant, 1.44
$C_{\varepsilon 2}$	k-ε turbulence model constant, 1.92
C_{μ}	k-ε turbulence model constant, 0.09
c	cross-coupled damping
c_{r1}, c_{r2}, c_{r3}	empirical constants for curvature correction, 1.0, 2.0, and 1.0 respectively
$[C]$	damping matrix of rotor system
F, F_{x}, F_{y}	forces on the rotor from seal
$\{F\}$	force vector on the rotor system
h	average grid size
K	direct stiffness
k	cross-coupled stiffness; kinetic energy of turbulence per unit mass
$[K]$	stiffness matrix of rotor system
M	direct inertia coefficient
m	cross-coupled inertia coefficient
$[M]$	mass matrix of rotor system
P_k	production per unit dissipation of k
p	static pressure
Q	Q-Factor
r	grid refinement factor
S_M	sum of body forces
t	time
U	mean velocity of flow
u, v, w	instantaneous velocities of flow
u_{τ}	friction velocity
u^{+}	dimensionless near wall velocity

X, Y	displacements of rotor
y^+	dimensionless sublayer-scaled distance from the wall

Greek Symbols

ε	eccentricity; turbulence eddy dissipation per unit mass
δ	offset of the shaft, logarithmic decrement
Δn	the distance between the first and second grid points off the wall
Δy	$\Delta n/4$
κ	von Kármán's constant, 0.41
μ	dynamic viscosity
ν	kinematic viscosity
ρ	mass density
σ_k	turbulence model constant for k equation, 1.0
σ_ε	k-ε turbulence model constant, 1.3
τ	shear stress
Ω	whirl speed
ω	shaft spinning speed

Subscripts and Superscripts

a	axial direction
r	radial direction
s	shaft synchronous surface
t	tangential direction or tangential to wall
w	wall surface value
+	sublayer-scaled value
ncr	natural frequency

1 Introduction

1.1 Background and Motivation

1.1.1 Introduction to the Labyrinth Seal

The labyrinth seal is a type of non-contacting annular seal serving to reduce leakage flow. It has been widely used in various kinds of turbo machines due to its benefits of no contact, no wear, small frictional power loss and long life [1]. In labyrinth seals, the pressure head of the working fluid is converted into kinetic energy when passing through the specially designed flow path. Figure 1-1 shows that the labyrinth seals are installed as eye seals on every stage and balance drum next to the last stage in a typical centrifugal compressor.

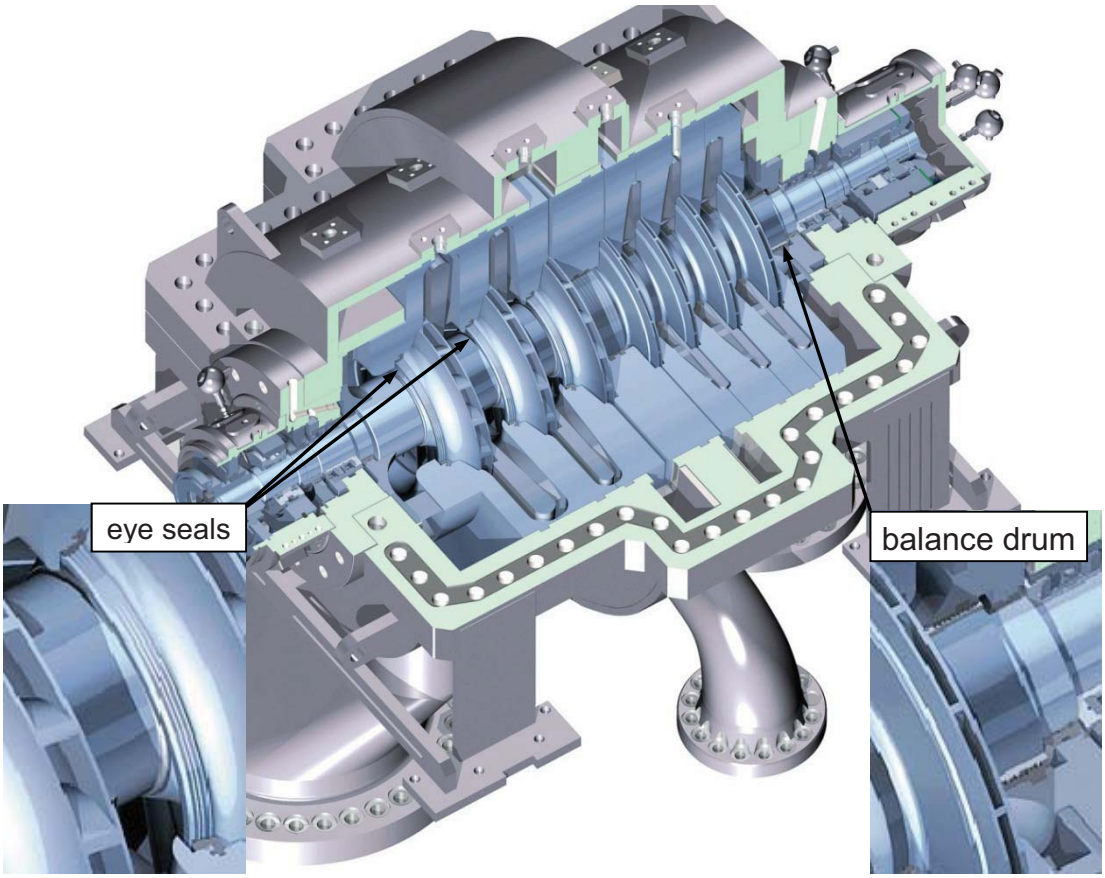

Figure 1-1 Cross section view of a centrifugal compressor (http://www.stoomturbine.nl/foto_siemens.html)

The labyrinth seal can be divided into several types based on their different shapes. Figure 1-2 shows three very common types: straight, stepped, and full labyrinth. The straight and stepped labyrinth seals can be further divided into tooth-on-stator and tooth-on-rotor, except for the full labyrinth seal with teeth on both rotor and stator.

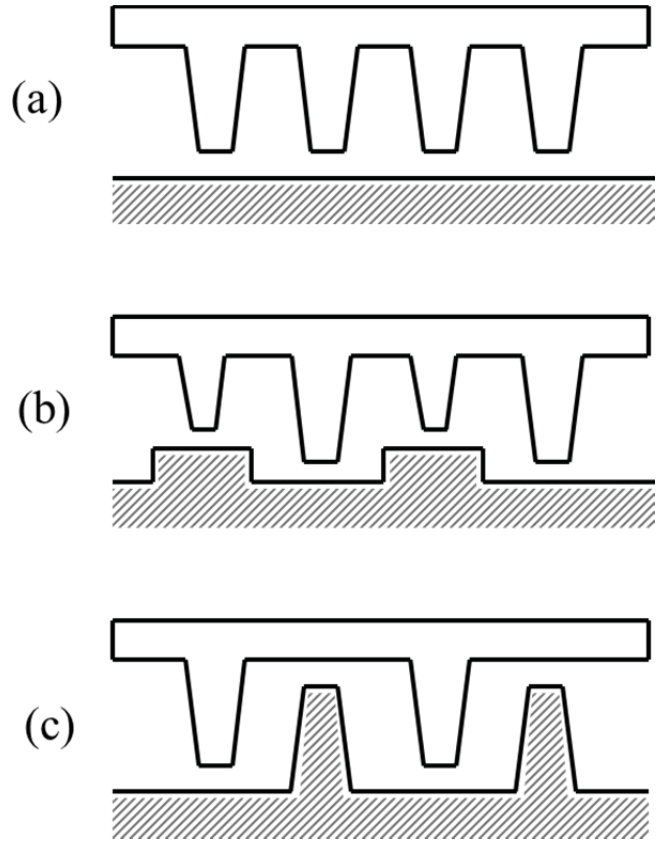

Figure 1-2 Labyrinth Types
(a) Straight Labyrinth; (b) Stepped Labyrinth; (c) Full Labyrinth

1.1.2 Motivation of the Research

When the leakage flow is blocked by the labyrinth seal, the flow generates forces on the rotor at the same time. Thus the labyrinth seal also influences rotordynamic properties of the rotor-bearing-seal system. The forces from labyrinth seal have to be included for a precise rotordynamic analysis so it is of interest to study the rotordynamic characteristics of the labyrinth seal. The study on labyrinth seals has been divided into two aspects: (1) focusing on the flow efficiency, leakage, and thermal effects; (2) evaluating the forces generated by the flow in the

seal and then analyze the rotordynamic properties of the seal. This research mostly belongs to the second category.

A linearized model [2-5] has been widely used to describe the rotordynamic properties of the labyrinth seal:

$$-\begin{Bmatrix} F_x \\ F_y \end{Bmatrix} = \begin{bmatrix} K & k \\ -k & K \end{bmatrix} \begin{Bmatrix} x \\ y \end{Bmatrix} + \begin{bmatrix} C & c \\ -c & C \end{bmatrix} \begin{Bmatrix} \dot{x} \\ \dot{y} \end{Bmatrix} \tag{1.1}$$

where (F_x, F_y) are reaction forces working on the rotor; diagonal terms (K, C) are direct stiffness and damping of the seal; off-diagonal terms (k, c) are cross-coupled stiffness and damping of the seal; and the inertia terms are neglected. The influence of labyrinth seal on the rotor can be predicted via the four rotordynamic coefficients of the seal. For example, the increase of cross-coupled stiffness, k, decreases the stability of the rotor while larger direct damping, C, helps to keep the rotor stable; the other two coefficients, K and c, have much smaller influence on stability[6].

Factors such as pre-swirl, eccentricity and clearance all have significant influences on the four rotordynamic coefficients thus can change the rotordynamic properties of the seal. Of those factors, the pre-swirl has a dominant influence on the rotordynamic coefficients of a given labyrinth seal. The pre-swirl can usually be generated by two ways: the friction from rotating rotor and shunt injection in a turbo machine. Since the pre-swirl rate is so important in this research, a clear definition will be given in the next section.

1.1.3 Definition of Pre-swirl Rate

Generally the pre-swirl rate is the ratio of fluid circumferential velocity and the shaft synchronous surface velocity. However, the circumferential velocity of working fluid is subjected to change with the axial location, so a datum plane is required to define pre-swirl rate. In this research, the plane which is 2.64 mm prior to the first tooth was selected as datum plane and the ratio of average circumferential velocity in that plane and shaft synchronous surface velocity is defined as pre-swirl rate, as shown in Figure 1-3. The data plane was placed in a region close to the leading edge of the first tooth and the pre-swirl rate in that region is almost constant in the numerical results. As discussed above, the pre-swirl rate influences rotordynamic

properties of the labyrinth seal, so it is of significance to generate a desired pre-swirl rate in calculated models. So far three ways has been applied, which will be discussed in sections from 2.3.1 to 2.3.3.

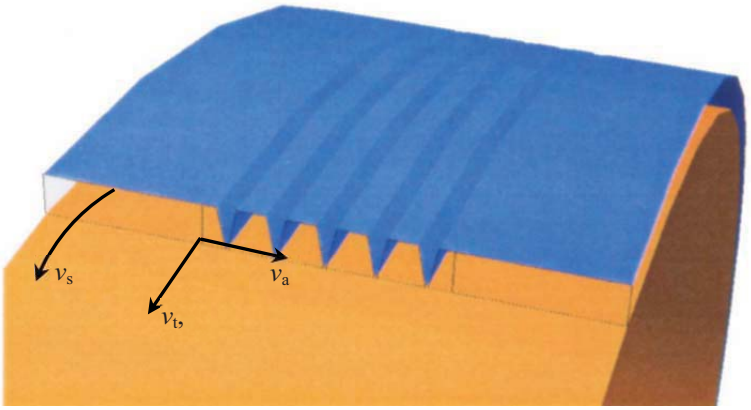

Figure 1-3 Illustration of pre-swirl rate

where v_a is the axial velocity of the flow, v_t is the circumferential velocity of the fluid, v_s is the shaft synchronous surface velocity.

1.1.4 Labyrinth Seals to Study

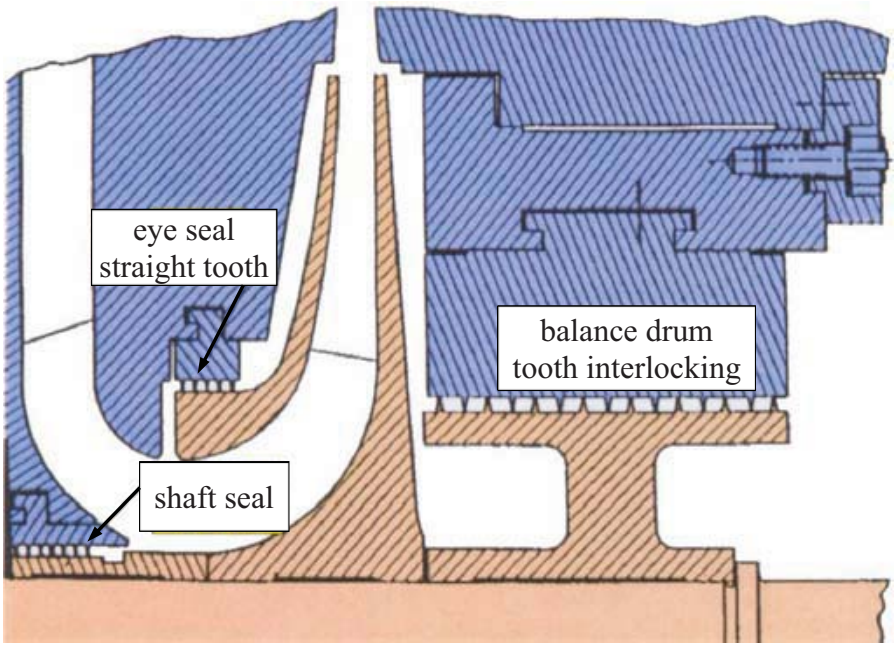

Figure 1-4 Typical compressor eye seal and balance drum seal

In this paper, three type of labyrinth seals will be modeled and studied: the straight eye seal with 5 teeth on stator as shown in Figure 1-4; the 5-tooth stepped eye seal which was employed

as the experimental seal in [17]; and the balance drum seal with 15 interlocking teeth (7 on stator) as shown in Figure 1-4. There are several reasons to study these three seals:

The straight eye seal is very typically used in compressors and it usually has a high pre-swirl rate around 70%. Moreover the simple geometry of the straight seal is beneficial for investigation on the effects of eccentricity, clearance, and tooth location. The eye seal shown in Figure 1-4 was actually used as a prototype and a series of models with varying eccentricities, clearances, and tooth locations were built.

As for the stepped eye seal, Kwanka [17] studied that seal in experiments so that it can be used to verify and validate the numerical models and methods applied in this research. It is noticeable that the pre-swirl rate is as high as 20 in his experiment due to the low rotating speed. Moreover, modern eye seals are more often designed as stepped seal to provide higher pressure drop so it is necessary to reconfirm the influence of high pre-swirl on this type of seal.

The balance drum seal usually has the longest geometry and highest pressure drop in a compressor and thus it has the most significant influence on the dynamic behavior of the rotor. Furthermore, it is usually installed close to the bearing and may have a coupled effect on the rotor stability. Due to that reason, the balance drum seal was studied and a rotor stability analysis was conducted afterwards.

The three seals will be modeled and further discussed in section 2.4.

1.2 Literature Review

The study on labyrinth seal has been processed on two different directions: to focus on the fluid field such as flow efficiency, leakage, thermal effects, and etc.[7-10]; to obtain forces generated by the flow in seal and then to analyze the rotordynamic properties of the seal. This section will mainly introduce previous works belonging to the second category. There were mainly three methods developed to study the forces and rotordynamic characteristics of the labyrinth seal: experiment, bulk flow, and calculation fluid dynamics (CFD).

The experiment has been an important approach to study labyrinth since ever. Alford [11] studied the influences of inlet and outlet areas on a labyrinth seal. He concluded that an excitation force is generated causing whirl in the direction of the rotation when the inlet area is bigger than the outlet area; conversely, there is no excitation force when the outlet is bigger than the inlet area.

Benchert and Wachter [12] conducted more experiments to test rotordynamic coefficients for the labyrinth seal. Their results showed that the tangential forces in eccentric labyrinth seals are caused by the uneven circumferential pressure distribution in the seal, which was induced by the circumferential flow in the seal. The circumferential flow comes from two sources: shaft rotation and swirling flows at the entrance to the seal. The results also show that with a variety of labyrinth seals the tangential forces are linear to the eccentricity ratio of the seal.

Experiments were carried out by Rajakumar and Sisto [13] more recently to determine the circumferential pressure distributions and forces generated by the flow in the labyrinth seal. In their experiments, they studied the variations of the radial and tangential forces with respect to eccentricity and rotor velocity. Both cases with and without pre-swirl were conducted. The results showed that the pre-swirl has a significant influence on the forward whirling rotor for a short labyrinth; moreover the radial force increases with respect to the pre-swirl rate in an eccentric labyrinth seal.

Childs and Scharrer [14] tested rotordynamic coefficients for both teeth-on-rotor and teeth-on-stator labyrinth seals in experiments and the results showed that the stiffness and damping coefficients are insensitive to rotor speed for both seal configurations but they are very sensitive to inlet tangential velocity, i.e. pre-swirl. They also concluded that the teeth-on-stator seal is more stable than the teeth-on-rotor seal for inlet tangential velocity in the direction of rotation. Childs and Scharrer [15] conducted more experiments to further study the influences of clearance and rotor rotating speed. They found that for teeth-on-rotor seals the direct damping increases with clearance while for teeth-on-stator seals the direct damping decreases with clearance. Direct stiffness is negative and increases as clearance increases for both seal configurations. Additionally, direct stiffness and direct damping are not sensitive to rotating speed while cross-coupled stiffness shows a sharp upswing at high rotating speed.

Soto and Childs [16] further studied the rotordynamic characteristics of the labyrinth seal with shunt injection via experimental approach. The results showed that seals configured with injections in both radial and against rotation directions have bigger cross-coupled stiffness and direct damping than traditional labyrinth seals. Additionally they concluded that labyrinth seals with injection against rotation are better able to control rotordynamic instabilities than ones with radial injection.

Kwanka [17] conducted experiments and evaluated the leakage and rotordynamic coefficients of a stepped labyrinth seal at different pre-swirl rates. The author also compared the rotordynamic properties of the stepped labyrinth seal to a straight labyrinth one with the same tooth number. The author concluded that the stepped labyrinth seal leaks less than a straight eye seal but the dynamic properties of the stepped seal may lead to system unstable. The stepped eye seal in this reference was employed for the numerical study in the dissertation.

Wagner et al. [18, 19] built a full-scale high-pressure test rig and tested the rotordynamic coefficients of impeller eye seals, which is designed as stepped labyrinth seal. It is noticeable that inertia coefficients of the eye seal were also tested in their study. Test results proved the existence of fluid inertia forces in the labyrinth seal, which indicates that the second order rotordynamic model for the labyrinth seal is required for high rep-swirl cases. Test results were also compared with numerical simulation.

Most recently, Zhang et al. [20] performed experiments on the influences of inlet pressure, rotating speed, eccentricity ratio, rotor vibration, and clearance. The results showed that seal forces increase almost linearly with the increasing inlet pressure, eccentricity ratio and vibration amplitude. Furthermore, the seal force is strongly sensitive to the change of clearance. It was also concluded that the phase difference between the seal force and the vibration influences the work done by the rotor.

The bulk-flow method is actually a simplified finite volume approach. It was applied to solve the flow in the labyrinth seal by Iwatsubo [21] in 1980 for the first time. The first bulk-flow model was a one-control-volume model. Forces induced by the labyrinth seal and the factors of the seal which affect the stability were investigated. Iwatsubo concluded that the forces

are proportional to the velocity and displacement of the rotor and always make the rotor system unstable.

Wyssmann et al. [22] developed the two-control-volume bulk-flow model to predict the flow and rotordynamic coefficients in a labyrinth seal. The model has been confirmed by comparing the numerical results with measured data taken from laboratory investigations and from measurements carried out on a high pressure centrifugal compressor. It was concluded that if a swirl brake is installed to reduce the pre-swirl of the leakage flow, then the labyrinth cross-coupling stiffness is eliminated as predicted by his theory and confirmed by measurements; while the damping action of the labyrinth is retained. Hence the author suggested that for a rotor stability analysis this should be taken into account if rotor design should not be overly conservative.

Scharrer [23] further developed the bulk-flow method with two control volume to predict rotordynamic coefficients and compared to the experimental result presented in [15]. The recirculation velocity in the cavity was incorporated into the model for the first time by using the jet flow theory. By comparison with experiment measurements, the result showed that this improved two-control-volume bulk-flow model is more accurate in predicting cross-coupled stiffness and direct damping than does the one-control-volume model [21, 24].

Kirk [2] developed a special design computer program using bulk-flow method to predict the forces and the rotordynamic characteristics of a labyrinth seal including the inlet and discharge leakage path. Some derivations of the perturbation equations were modified in his model. And the model was validated by comparing with test data. Kirk [25] further applied this model to evaluate rotordynamic coefficients of the labyrinth seal with high pre-swirl rate. The pre-swirl at the entrance of the seal was calculated by employing a radial chamber. The results showed that non-uniform leak path geometry can be used to increase or decrease the swirl in the gas leak path. Additionally, increased stator surface roughness will suppress the swirl due to the increased shear drag on the swirling flow.

Yücel [26] established a specific bulk-flow model for the stepped labyrinth seal focusing on the influence of pre-swirl. The author also compared his results with Kwanka's test data [17] and showed good agreement. Ha [27] and Eser [28] also developed a bulk-flow method for the

stepped labyrinth seal using different friction-factor models and compared their results with previous experimental or calculational results

Picardo and Childs [29] compared the predictions of one-control-volume model and two-control-volume with experimental data. Different clearances and pressure ratios were taken into account. Even though the test results poorly agreed with theoretical prediction based on bulk-flow model, the author concluded that the one-control-volume model provides a conservative prediction for effective damping and both models under predict leakage rates.

Rhode and Sobolik [30] applied a finite element approximation to predict the leakage flow in the labyrinth seal. They iteratively made use of one cavity to model the flow through labyrinth seals with five, ten, and fifteen cavities. The computer code was developed and was validated with other types of flows, including subsonic flow through a pipe expansion and incompressible flow though a large scale model of a generic labyrinth seal. The results showed that relatively close agreement with experimental labyrinth seal data was achieved with the fifteen cavity seal. Flow characteristics in a single labyrinth cavity were also shown.

With the development of computer technology, computational fluid dynamics (CFD) has become an important method to predict the flow and forces in seals since 1990s. Rhode et al. [31, 32] developed a three-dimensional finite difference approach and studied the influence of inlet swirl on the flow though a labyrinth seal. It was shown that the inlet swirl has a significant influence on the forces produced by the flow in seal. Furthermore, larger inlet swirls increases the forces and led to more unstable operating conditions.

Ishii et al. [33] developed a numerical method based on the finite volume approach to predict the flow and rotordynamic forces in an eccentric labyrinth seal. The results showed that the circumferential pressure distribution in the seal agrees with experimental data well. Moreover, the authors also concluded that the inlet swirl causes less desirable radial and tangential forces in the labyrinth seal. It was determined that forces obtained by the finite-volume code had good agreement with experimental data for the interior labyrinth seal cavities, but did not agree well with the experimental results for the cavities towards the inlet and outlet of the labyrinth seal.

Moore [34] developed a CFD code to analyze the flow and forces in a labyrinth seal. The CFD results were compared to those from bulk-flow approach and it was shown that the bulk-flow approach under-predicted direct stiffness values and reasonably predicted damping values. It was shown that the CFD results well agree with experimental results for forces and leakage. Moreover, they author also concluded that compared to the bulk-flow codes, a drawback to the CFD software is the computational time involved in obtaining CFD solutions.

Kirk and Guo [35] used a commercial CFD program, TASCflow, to predict the flow and forces in a normal speed labyrinth seal and a high speed compressor eye seal. For each seal, a three-dimensional model with eccentric rotor was built and solved and the result was compared with the result from bulk-flow approach. It was shown that the bulk-flow prediction could match the CFD prediction better by adjusting the friction factors.

Hirano et al. [36] used both TASCflow and bulk-flow codes to calculate forces and rotordynamic coefficients of a typical compressor eye seal and a steam turbine labyrinth seal. A systematically mesh independent study was conducted in this paper. The results were compared to previous bulk-flow results. It was shown that the two methods give relatively close results for leakage flow; however bulk-flow method overestimates the rotordynamic forces in the labyrinth seal compared to the TASCflow results. In another word, the bulk-flow method gives a pessimistic prediction of the destabilizing forces. Some numerical methods introduced in this reference were inherited such as the frame transfer and the grid independent study; furthermore, some numerical methods were developed and improved, such as the improvement on generating a high pre-swirl rate (>70%).

Recently the influence of leak path geometry and friction on inlet swirl in a labyrinth seal was investigated by Kirk and Guo [37] with both CFD and bulk-flow approaches. The results showed that the geometry and the resultant reverse pumping flow in the entry channel have a significant influence on the pre-swirl rate: a diverging leak path will generate larger pre-swirl values than a uniform leak path; a converging leak path will generate smaller pre-swirl values than a uniform leak path. Moreover the authors concluded that there were significant differences between the TASCflow and bulk-flow analysis for pre-swirl: the bulk-flow inlet swirl results were shown to vary from 92% to 149% with the TASCflow results; and the bulk-flow method provides a pessimistic prediction of the inlet swirl velocities when compared to TASCflow.

The nonlinear approach has also been applied to study the flow and rotordynamic properties of seals. Huang and Li [38-40] developed a nonlinear method to investigate the influence of pre-swirl on the stability of the rotor. The results again proved that high pre-swirl rate leads to instability of the rotor. The authors also concluded that the force excited by the flow is not linearly related to the displacement and velocity of the rotor. The direct stiffness increases rapidly with the increase of amplitude and the cross-coupled stiffness increases with the increase of amplitude at a very small rate; the direct damping decreases rapidly with the increase of velocity and the cross-coupled damping decreases gradually with the increase of velocity.

1.3 Aims and Objects

As shown by the literature review, previous researchers did not systematically study the exact relationships between rotordynamic coefficients and factors such as pre-swirl, eccentricity, clearance, and location of tooth. Moreover, high pre-swirl has never been fully studied even though pre-swirl was considered in some previous work. So the main aims of this research are:

1) To predict rotordynamic coefficients of the three labyrinth seals based on the fluid field results given by the numerical simulation;

2) To systematically evaluate the influences of pre-swirl, eccentricity, clearance, and location of tooth on rotordynamic characteristics of the labyrinth seal;

3) To establish a second-order rotordynamic model for the labyrinth seal in high pre-swirl conditions.

4) To conduct a rotor stability analysis to study how high pre-swirled labyrinth seal affects the stability of a practical compressor rotor system.

1.4 Dissertation Outline

1) Three types of labyrinth seal have been studied in this research: the straight eye seal, the stepped eye seal, and the balance drum seal. In the study of the straight eye seal, sets of three-

dimensional models with different eccentricities, clearances, and tooth locations were built based on the prototype eye seal as shown in Figure 1-4. The highest pre-swirl rate for the straight eye seal was 75.6%, eccentricity ranged from 0.1 to 0.7 and the clearance ranged from 146μm to 438μm. For the stepped eye seal, the seal from [17] was modeled and calculated with the eccentricity of 0.1 and compared with experimental data. Due to the low rotating speed of the rotor, the pre-swirl rate is as high as 20 for the stepped seal. The balance drum seal in Figure 1-4 was also modeled and studied, with eccentricity of 0.1 and the highest pre-swirl rate of 75%. All models were built in Solid Works and meshed in ANSYS-ICEM. Then they were numerically solved in ANSYS-CFX to simulate the fluid field.

2) A system numerical method was developed to simulate the flow in labyrinth seals. The rotating reference frame was applied to simplify the complicated transient rotor motion to a stationary problem. The k-ε turbulence model with curvature correction and the scalable wall function were employed. A systematical grid study including grid independence study and estimation on discretization error was conducted to minimize the error generated by meshing. To verify the numerical model and method used in this research, part of the results have been compared to previous bulk-flow and experimental results [17, 36].

3) Since the pre-swirl has a significant influence on rotordynamic properties of labyrinth seals, it is of interest to generate a high enough pre-swirl rate, which had actually been difficult to obtain in the CFD process. This dissertation will discuss three ways to generate pre-swirl: (1) to add inlet path with special shapes or extra teeth, (2) to apply a rough inlet, and (3) to specify the velocity ratio at the inlet. The three ways were studied and compared and the approach by specifying velocity ratio was finally employed for all the calculation in this research.

4) The fluid field has to be analyzed to guarantee the precision of the rotordynamic analysis afterwards. The pressure distributions and leakages for the three seals were compared with bulk-flow results. An extra small vortex at the downstream edge of each tooth was found. This has never been reported before and the discovery of this small vortex will help to improve seal design in future. The flow details at the discharge region and chambers were also discussed.

5) Then forces on the rotor were extracted from the fluid field and applied for rotordynamic analysis. The second-order rotordynamic model including inertia terms was built and applied to the rotordynamic analysis in this research.

6) Rotordynamic coefficients of the three labyrinth seals were solved based on the second-order model. Different pre-swirl rates, clearances, eccentricities and configurations on tooth location were considered. Some relationships between those influencing factors and the four coefficients were concluded.

7) Rotordynamic stability analysis was conducted on a typical radial compressor shaft considering fluid forces from bearings, aerodynamic effects, and balance drum. The analysis showed that the high pre-swirl could lead to rotor instability and thus de-swirling equipment should be employed in turbo machines.

2 Numerical Method and Model

2.1 Frame Transfer

Observing the motion of rotor-seal system from a stationary frame, the rotor is spinning at the speed ω while also whirling at the speed Ω at the same time, which means that the location of rotor and thus the shape of mesh are changing all the time. So it is actually a transient problem involved with mesh moving.

To avoid a transient analysis and moving mesh, a rotating frame with the speed Ω was applied as shown in Figure 2-1. In the rotating frame, the rotor itself spins at the speed ω, while the stator spins at the speed Ω in the opposite direction to the frame. Thus it becomes a steady state problem and there is no mesh moving. Viewing the same motions from the stationary frame, the rotor is actually spinning at the speed ω and whirling at the speed Ω, while the stator is at rest.

All variables were calculated in the rotating frame and then transferred to the stationary frame for further rotordynamic analysis.

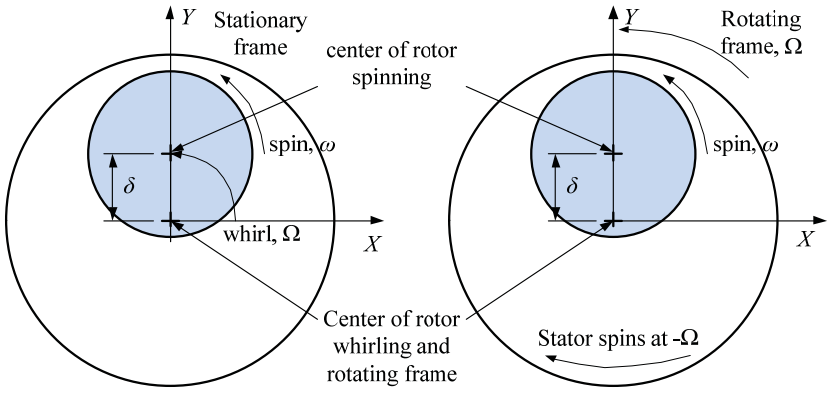

Figure 2-1 Frame transfer from stationary to rotating

2.2 Numerical Methods

2.2.1 The *k*-ε Turbulence Model

Even though the problem became steady state in the rotating frame, the flow is still very complicated considering the high axial and circumferential velocities and pressure drop. The flow in labyrinth seal is typically three-dimensional turbulence. So 3D Reynolds-averaged Navier-Stokes (RANS) equations were numerically solved in CFX to analyze the flow patterns including velocities and pressure.

Two-equation turbulence models are very widely used, as they offer a good compromise between numerical effort and computational accuracy. Furthermore, two-equation models are more sophisticated than the zero equation models. Both the velocity and length scale are solved using separate transport equations. By far, the most popular two-equation turbulence models are the *k*-ε and the *k*-ω models [41].

Both the *k*-ε model and the *k*-ω model use the gradient diffusion hypothesis to relate the Reynolds stresses to the mean velocity gradients and the turbulent viscosity. The turbulent viscosity is modeled as the product of a turbulent velocity and turbulent length scale, in the two models. The turbulence velocity scale is computed from the turbulent kinetic energy, which is provided from the solution of its transport equation. The turbulent length scale is estimated from two properties of the turbulence field: usually the turbulent kinetic energy and its dissipation rate. The dissipation rate of the turbulent kinetic energy is provided from the solution of its transport equation [42].

In this research the standard *k*-ε model was selected to solve the turbulent flow and the scalable logarithmic wall function was used to describe the near wall velocity. The y^+ criterion meet over almost entire wall region. The theory about wall function will be further discussed in section 2.2.3.

The *k*-ε model introduces two new variables into the system of equations. *k* is the turbulence kinetic energy and is defined as the variance of the fluctuations in velocity. It has dimensions of (L^2 T^{-2}). ε is the turbulence eddy dissipation (the rate at which the velocity fluctuations dissipate), and has dimensions of *k* per unit time (L^2 T^{-3}).

The continuity equation is then:

$$\frac{\partial \rho}{\partial t} + \frac{\partial}{\partial x_j}\left(\rho U_j\right) = 0 \tag{2.1}$$

The momentum equation is given by

$$\frac{\partial \rho U_i}{\partial t} + \frac{\partial}{\partial x_j}\left(\rho U_i U_j\right) = -\frac{\partial p^{'}}{\partial x_i} + \frac{\partial}{\partial x_j}\left[\mu_{eff}\left(\frac{\partial U_i}{\partial x_j} + \frac{\partial U_j}{\partial x_i}\right)\right] + S_M \tag{2.2}$$

where S_M is the sum of body forces, μ_{eff} is the effective viscosity accounting for turbulence, and $p^{'}$ is the modified pressure defined as

$$p^{'} = p + \frac{2}{3}\rho k + \frac{2}{3}\mu_{eff}\frac{\partial U_k}{\partial x_k} \tag{2.3}$$

The k-ε model is based on the eddy viscosity concept, so that

$$\mu_{\text{eff}} = \mu + \mu_{\text{t}} \tag{2.4}$$

where μ_{t} is the turbulence viscosity. The k-ε model assumes that the turbulence viscosity is linked to the turbulence kinetic energy and dissipation via the relation:

$$\mu_{\text{t}} = C_\mu \rho \frac{k^2}{\varepsilon} \tag{2.5}$$

where C_μ is a constant. Values of all constants are given in the nomenclature.

The values of k and ε are obtained directly from the differential transport equations for the turbulence kinetic energy and turbulence dissipation rate:

$$\frac{\partial(\rho k)}{\partial t} + \frac{\partial}{\partial x_j}\left(\rho U_j k\right) = \frac{\partial}{\partial x_j}\left[\left(\mu + \frac{\mu_t}{\sigma_k}\right)\frac{\partial k}{\partial x_j}\right] + P_k - \rho\varepsilon + P_{kb} \tag{2.6}$$

$$\frac{\partial(\rho \varepsilon)}{\partial t} + \frac{\partial}{\partial x_j}\left(\rho U_j \varepsilon\right) = \frac{\partial}{\partial x_j}\left[\left(\mu + \frac{\mu_t}{\sigma_k}\right)\frac{\partial \varepsilon}{\partial x_j}\right] + \frac{\varepsilon}{k}\left(C_{\varepsilon 1} P_k - C_{\varepsilon 2}\rho\varepsilon + C_{\varepsilon 1} P_{\varepsilon b}\right) \tag{2.7}$$

where $C_{\varepsilon 1}$, $C_{\varepsilon 2}$, σ_k, and σ_ε are constants. P_{kb} and $P_{\varepsilon b}$ represent the influence of the buoyancy forces. P_k is the turbulence production due to viscous forces, which is modeled with:

$$P_k = \mu_t \left(\frac{\partial U_i}{\partial x_j} + \frac{\partial U_j}{\partial x_i} \right) \frac{\partial U_i}{\partial x_j} - \frac{2}{3} \frac{\partial U_k}{\partial x_k} \left(3\mu_t \frac{\partial U_k}{\partial x_k} + \rho k \right) \tag{2.8}$$

2.2.2 Curvature Correction

The k-ε model has a weakness of insensitivity to streamline curvature and system rotation. So the curvature correction was applied to sensitize the k-ε model to these effects. The empirical function suggested by Spalart and Shur [43] to compensate this defect is given as

$$f_{\text{rotation}} = (1 + c_{r1}) \frac{2r^*}{1 + r^*} \left[1 - c_{r3} \tan^{-1} \left(c_{r2} \tilde{r} \right) \right] - c_{r1} \tag{2.9}$$

where c_{r1}, c_{r2}, and c_{r3} are empirical constants.

It is used as a multiplier of the production term and has been limited in ANSYS-CFX in the following way:

$$P_k \rightarrow P_k f_r \tag{2.10}$$

where

$$f_r = \max \left[0, 1 + C_{\text{scale}} \left(\widetilde{f}_r - 1 \right) \right] \tag{2.11}$$

and

$$\widetilde{f}_r = \max \left\{ \min \left(f_{\text{rotation}}, 1.25 \right), 0 \right\} \tag{2.12}$$

The scaling coefficient C_{scale} has been introduced to allow the user to influence the effect of the curvature correction in ANSYS-CFX. In this research, the values of this scaling coefficient were set as 1.0 for all simulations.

Assuming that all the variables and their derivatives are defined in the rotating frame of the calculation, which is rotating with a speed of Ω^{rot}, the arguments r^* and $\tilde{r}$ of the function $f_{rotation}$ can be defined as.

$$r^* = \frac{S}{\Omega} \tag{2.13}$$

$$\tilde{r} = 2\Omega_{ik} S_{jk} \left[\frac{DS_{ij}}{Dt} \mid \left(c_{imn} S_{jn} \mid c_{jmn} S_{in} \right) \Omega_m^{Rot} \right]^1_{\Omega D^3} \tag{2.14}$$

where the first term in brackets is equivalent to the 2nd velocity gradient and the 2nd term in the brackets is a measure of the system rotation. The strain rate and vorticity tensor are defied, respectively, using Einstein summation convention as

$$S_{ij} = \frac{1}{2} \begin{pmatrix} \partial U_i & \partial U_j \\ \partial x_j & \partial x_i \end{pmatrix} \tag{2.15}$$

$$\Omega_{ij} = \frac{1}{2} \left(\frac{\partial U_i}{\partial x_j} - \frac{\partial U_j}{\partial x_i} \right) + 2\varepsilon_{mji} \Omega_m^{rot} \tag{2.16}$$

where

$$\begin{aligned} S^2 &= 2S_{ij} S_{ij} \\ \Omega^2 &= 2\Omega_{ij} \Omega_{ij} \\ D^2 &= \max\left(S^2, 0.09\omega^2 \right) \end{aligned} \tag{2.17}$$

and where DS_{ij}/D_t are the components of the Lagrangian derivative of the strain rate tensor.

2.2.3 Scalable Wall Function

The law of the wall describes the velocity profile for a turbulent boundary layer as shown in Figure 2-2. The boundary layer can be divided into three regions: viscous sublayer, log layer and defect layer. The streamwise velocity flow varies logarithmically with distance from the surface in the log layer.

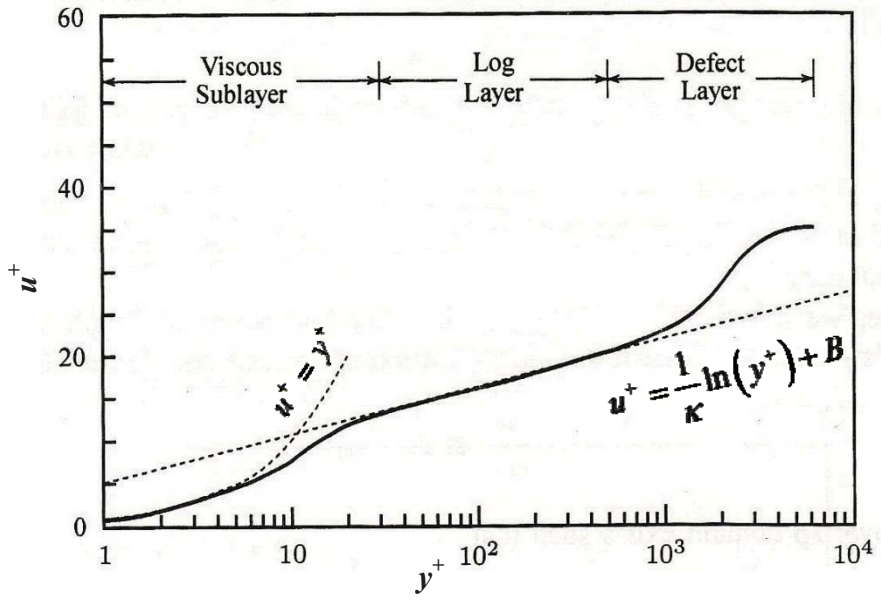

Figure 2-2 Law of the wall

The law of the wall defines some new variables: u_τ, the friction velocity; u^+, the dimensionless near wall velocity; y^+, the dimensionless distance from the wall. u_τ is given as.

$$u_\tau = \left(\frac{\tau_w}{\rho}\right)^{1/2} \tag{2.18}$$

where τ_w is the wall shear stress. y^+ is defined as

$$y^+ = \frac{\rho \Delta y u_\tau}{\mu} \tag{2.19}$$

where Δy is the distance from the wall and it has different numerical definitions in different wall functions. For the scalable wall function used in this research, $\Delta y = \Delta n/4$ and Δn is the near wall grid spacing.

In the viscous sublayer, the law of the wall gives:

$$u^+ = y^+ \tag{2.20}$$

In the log layer, the law of the wall gives

$$u^+ = \frac{U_t}{u_\tau} = \frac{1}{\kappa}\ln\left(y^+\right) + B \tag{2.21}$$

where B is a log-layer constant depending on wall roughness and $B \approx 5.10$ for smooth wall; U_t is the known velocity tangent to the wall at a distance of Δy from the wall; κ is the von Karman constant.

In wall function approaches in ANSYS-CFX, the velocity profile in the whole turbulent boundary layer is approximated by eq (2.21) to provide near-wall boundary conditions for the mean flow and turbulence transport equations. However, eq (2.21) has the problem that it becomes singular at separation points where the near wall velocity, U_t, approaches zero. An alternative velocity scale, u^* can be used instead of u_τ.

$$u^* = C_\mu^{1/4} k^{1/2} \tag{2.22}$$

And thus y^+ is replaced by y^* which is given as

$$y^* = \frac{\rho u^* \Delta y}{\mu} \tag{2.23}$$

This scale has the useful property because it does not go to zero if U_t goes to zero. Based on this definition, the following explicit equation for u_τ can be obtained:

$$u_\tau = \frac{U_t}{\frac{1}{2}\ln\left(y^*\right) + c} \tag{2.24}$$

The absolute value of the wall shear stress τ_w is then obtained from:

$$\tau_w = \rho u^* u_\tau \tag{2.25}$$

One of the major drawbacks of the wall function approach is that the predictions depend on the location of the point nearest to the wall and are sensitive to the near-wall meshing: refining the mesh does not necessarily give a unique solution of increasing accuracy. In the case of fine meshes, the problem of inconsistencies in the wall function can be overcome with the use of the Scalable Wall Function formulation developed by ANSYS-CFX, which can be applied on arbitrarily fine meshes and allows performing a consistent mesh refinement independent of the Reynolds number of the application.

The basic idea of the scalable wall function approach is to limit the y^* value used in eq (2.24) by a lower value of

$$\tilde{y}^* = \max(y^*, 11.06) \tag{2.26}$$

The value of 11.06 is the intersection between the logarithmic and the linear near wall profile as shown in Figure 2-2. The computed $\tilde{y}^*$ is therefore not allowed to be smaller than this limit. Therefore, all mesh points are outside the viscous sublayer and all fine mesh inconsistencies are avoided.

Thus the boundary condition for the dissipation rate, ε, is then given by the following relation which is valid in the logarithmic region:

$$\varepsilon = \frac{\rho u^*}{\tilde{y}^* \mu} \frac{C_\mu^{3/4}}{\kappa} k^{3/2} \tag{2.27}$$

If too many y^* values are smaller than 11.06 and replaced by eq (2.26), the accuracy of the calculation will be certainly decreased and the scalable wall function will be inappropriate. It means that to guarantee the accuracy by applying the scalable wall function in ANSYS-CFX, most values of y^* should be bigger than 11.06. The values of y^* are output as the variable of Yplus in ANSYS-CFX.

The minimum Yplus value is 18.4 on the wall of the rotor and 74.2 on the stator, so this criterion was satisfied over almost entire wall region in this research.

2.2.4 Assumptions

To simplify the problem, the working fluid is always assumed to be ideal gas for all the models of the three seals even though the working air may vary for each seal. The walls of both stator and rotor are assumed to be adiabatic, smooth and non-slip. The roughness of wall actually helps fluid to pick up more circumferential velocity before entering the seal, which will be further discussed in next section. However this makes the problem more complex so the rough wall was not used in the research. The desired convergent target of each simulation is that the root mean square (rms) residuals of the momentum and mass equations, energy equation, and

turbulence equations reach 10^{-5}. Turbulence models and assumptions applied in the research are summarized in Table 2-1.

Table 2-1 Assumptions and models in the simulation

Fluid	Air (ideal gas)
Wall properties	Adiabatic, smooth, non-slip
Turbulent model	*k*-*ε* with curvature correction Scalable log law wall function
Discretization scheme	Second-order high resolution
Convergence criterion	10^{-5} (rms)

2.3 Generation of Pre-swirl

2.3.1 Inlet Path with Special Shapes or Extra Teeth

It has been proven by Kirk and Guo [37, 44] that the converging inlet path helps the fluid to obtain bigger circumferential velocity. The pre-swirl rate of 46.69% was obtained by applying the converging inlet path in their research. Thompson [45] made some improvement based on that by building a model with reducing diameter radius inlet path and extra teeth as shown in Figure 2-3 and a pre-swirl rate as high as 62.2% was obtained.

However, the highest pre-swirl rate obtained by this method was 62.2% which is still lower than the usual pre-swirl rate of 70% for a typical compressor eye seal. Moreover, there is an obvious drawback of this method that it evolves extra modeling load, extra mesh and thus extra calculation time. It is also difficult to predict the required number of extra teeth and the shape of converging inlet so a set of models has to be built and calculated to find out the proper one, which make this method more time consuming.

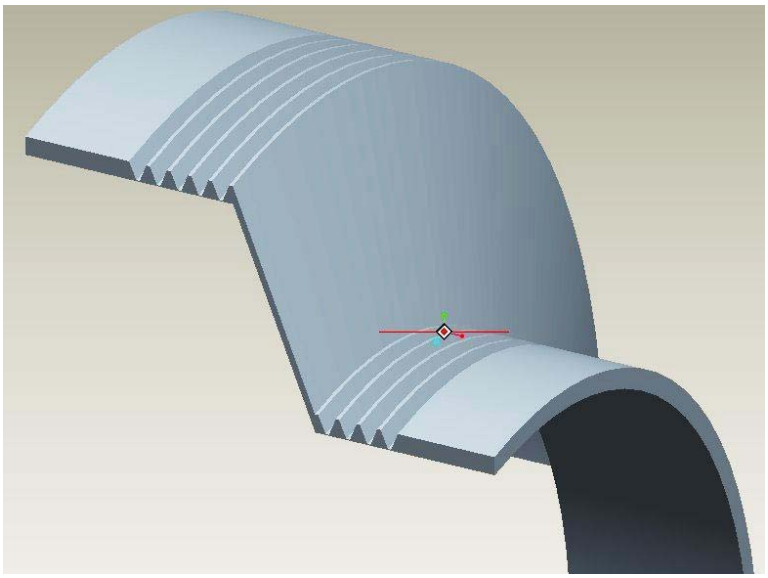

Figure 2-3 A combined application of reducing diameter inlet and extra teeth

2.3.2 Rough and Long Inlet Path

The rough wall increases turbulence of the flow and helps the flow to pick up more circumferential velocity; however there may be a limit for this function. To test that, a simplified O-shaped pipe with a specific pressure drop was calculated for different roughness and length of inlet path and the result in Figure 2-4 shows that there is a limit for the increase of pre-swirl rate.

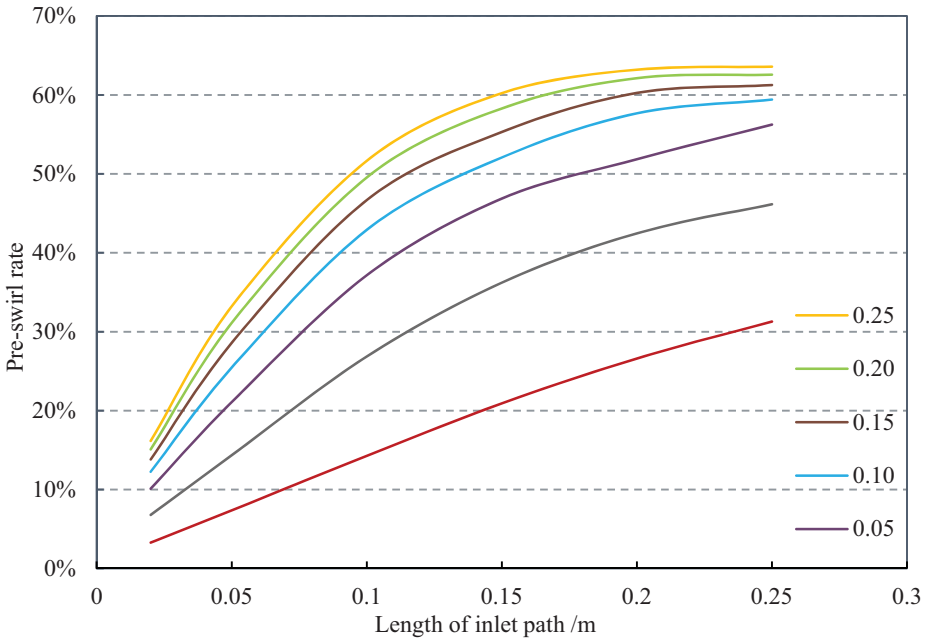

Figure 2-4 Pre-swirl rate *vs*. length of inlet path at different roughness

In this simulation, when the roughness was set to be bigger than 0.25, the case failed to converge. This is because that the scalable wall function employed in the simulation is not suitable for large roughness surface. To solve higher roughness, the automatic scalable wall function is required. However this breaks the consistency of method in the research even though a higher pre-swirl may be obtained with higher roughness.

2.3.3 Ratio of Inlet Velocities

The velocity profile at the inlet is unknown so that in the simulation the inlet boundary condition has to be set with pressure. However the ANSYS-CFX allows specifying the ratio of the three velocity components. As shown in Figure 2-5, the ratio of circumferential and axial velocities at inlet is subjected to change until the desired pre-swirl rate at section B (before entering the seal) is obtained. The radial velocity at inlet is zero.

Usually a proper velocity ratio at inlet can be found after several trial calculations. This approach avoids building and meshing many extra models and actually can obtain a very high pre-swirl rate, even more than 100%.

Practical labyrinth seals usually start from section B and the region between A and B only serves to make the problem converge better, so in the rotordynamic analysis forces from that region were excluded.

This method has been proven to be an efficient way and has been employed in this research.

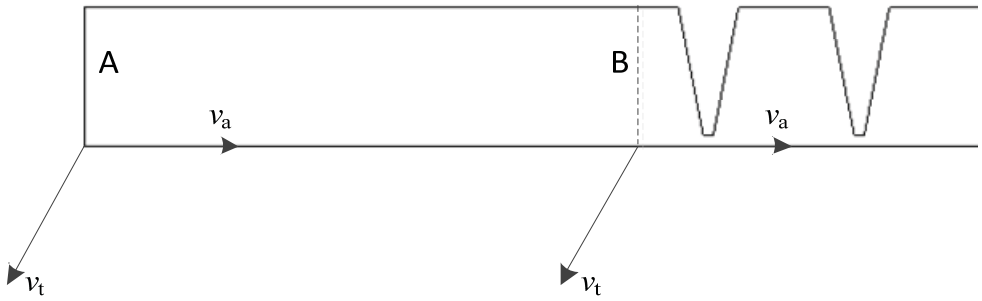

Figure 2-5 Illustration of specifying inlet velocities

2.4 Computational Models

2.4.1 Straight Labyrinth Eye Seal

A set of the 5-tooth straight labyrinth eye seal models was modeled according to the dimensions shown in Figure 2-6. The three-dimensional models have to be built because of the eccentricity. In those models, the eccentricities ranged from 0.1 to 0.7 to study the influence of eccentricity on labyrinth seals. Higher eccentricity would lead to converging problem. For the purpose of studying how clearance affect rotordynamic characteristics of labyrinth seals, a series of three-dimensional models with the clearance varying from 146μm to 438μm were built based on the dimensions of the prototype shown in Figure 2-6. One of the three-dimensional models is shown in Figure 2-7.

To investigate the influence of tooth location, a model with teeth on rotor was also built based on dimensions of the prototype straight seal shown in Figure 2-6. There is no change to dimensions except for the change of tooth location.

The pre-swirl rates for typical seals in a compressor are usually around 70% and the highest pre-swirl rate of 75.6% was obtained in the simulation. Boundary conditions in both stationary and rotating fames for the straight labyrinth eye seal are summarized in Table 2-2.

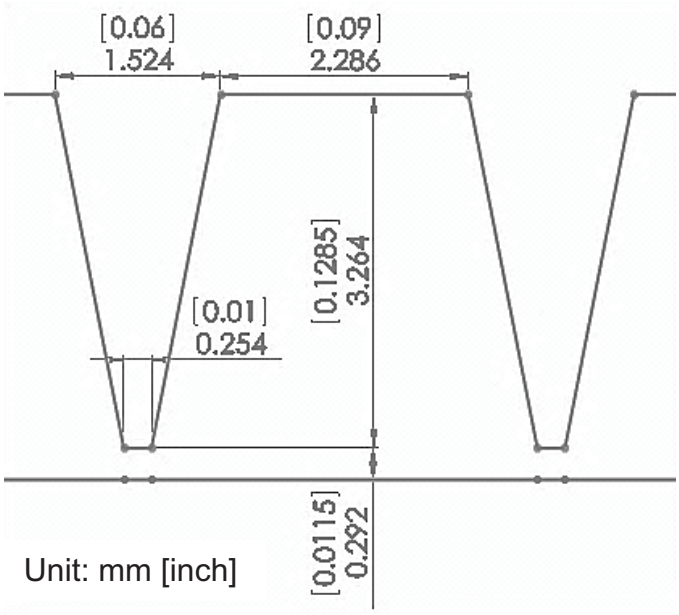

Figure 2-6 Dimensions of the straight labyrinth seal (tooth on stator)

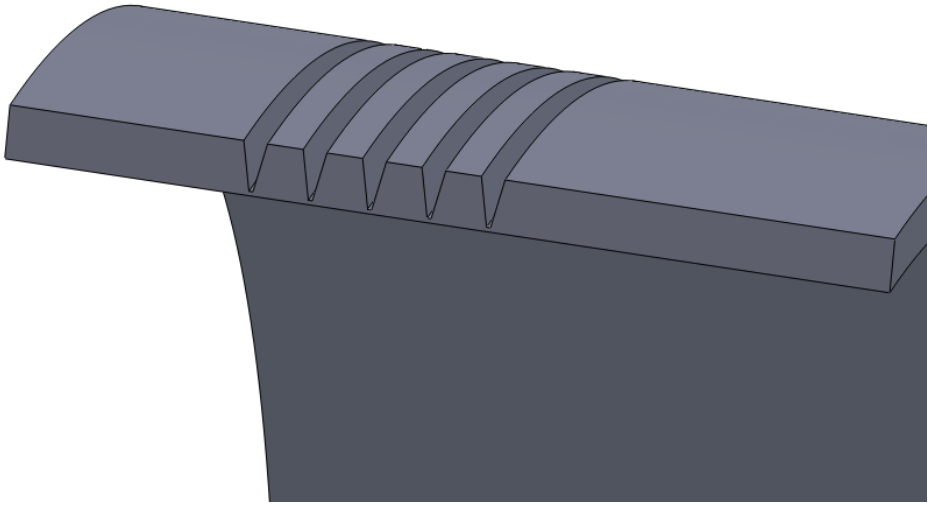

Figure 2-7 3-D model of the straight eye seal
(tooth-on-stator, 10% eccentricity, 292 μm clearance)

Table 2-2 Boundary conditions for the straight eye seal

B.C's	In Stationary Frame	In Rotating Frame
Inlet pressure	3.447 MPa (500 psi)	3.447 MPa (500 psi)
Inlet temperature	366.7 K (660 R)	366.7 K (660 R)
Inlet velocity ratio	Subjected to change	Subjected to change
Desired pre-swirl rates	70%	70%
Outlet pressure	1.724 MPa (250 psi)	1.724 MPa (250 psi)
Frame rotating speed	0	Ω
Stator rotating speed	0	- Ω
Rotor whirl speed	Ω	0
Rotor spinning speed	1162 rad/s (11,097 rpm)	1162 rad/s (11,097 rpm)

Note: Ω = 0, 290.5, 581, 871.5, and 1162 rad/s

2.4.2 Stepped Labyrinth Eye Seal

Modern eye seals are more usually designed as stepped labyrinth seal so an experimental stepped seal used in [17] was modeled and calculated. The three-dimensional model was built based on the dimensions shown in Figure 2-8. The three-dimensional model is shown in Figure 2-9.

Boundary conditions in both stationary and rotating fames for the stepped labyrinth eye seal are summarized in Table 2-3. It is noticeable that rotating speed for this experimental seal is much lower than practical rotors for industrial use, which leads to an extraordinarily high pre-swirl rate of 2000%. The highest pre-swirl obtained in the simulation was 2030%.

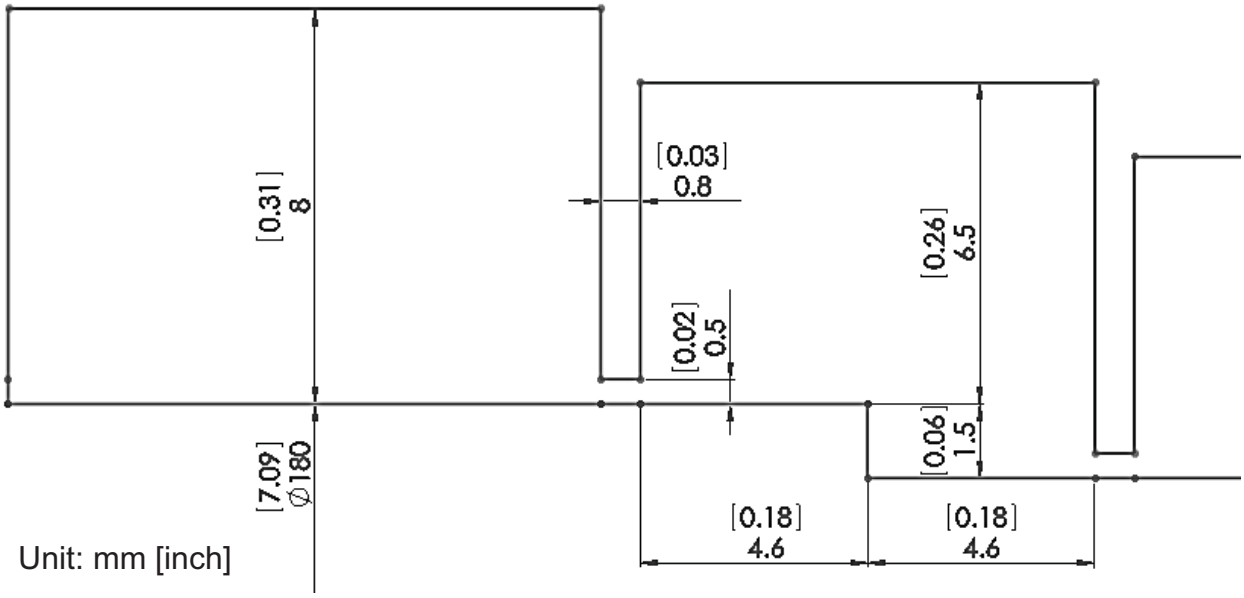

Figure 2-8 Dimension of the stepped labyrinth seal

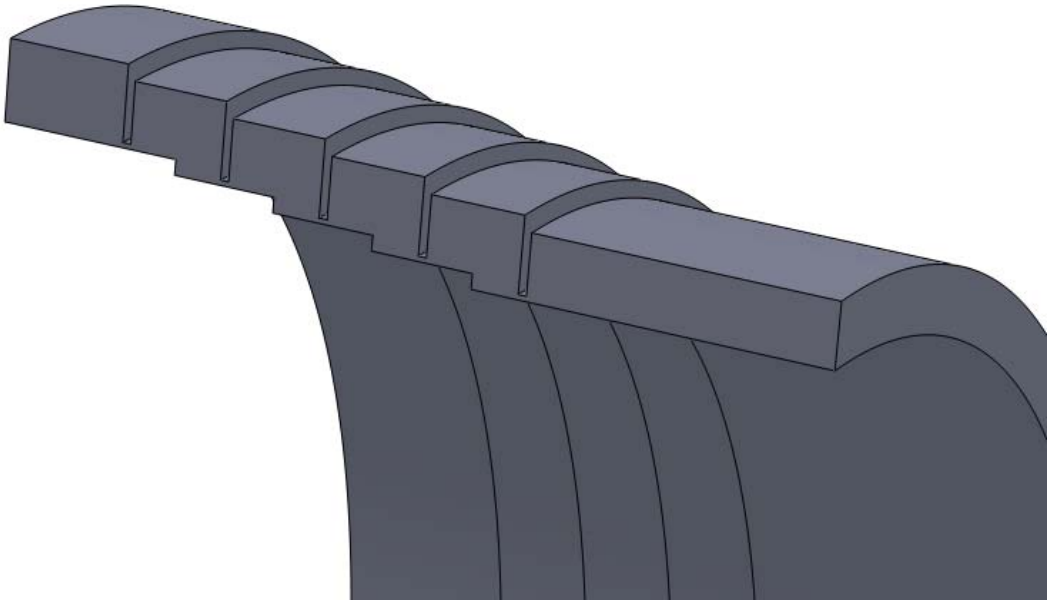

Figure 2-9 3-D model of the stepped eye seal

Table 2-3 Boundary conditions for the stepped eye seal

B.C's	In Stationary Frame	In Rotating Frame
Inlet pressure	201 kPa (29.2 psi)	201 kPa (29.2 psi)
Inlet temperature	300 K (540 R)	300 K (540 R)
Inlet velocity ratio	Subjected to change	Subjected to change
Desired pre-swirl rate	2000%	2000%
Outlet pressure	101 kPa (14.6 psi)	101 kPa (14.6 psi)
Frame rotating speed	0	Ω
Stator rotating speed	0	$-\Omega$
Rotor whirl speed	Ω	0
Rotor spinning speed	78.5 rad/s (750 rpm)	78.5 rad/s (750 rpm)

Note: Ω = 0, 19.6, 39.3, 58.9, and 78.5 rad/s

2.4.3 Balance Drum Labyrinth Seal

To generate higher pressure drop, balance drum seals usually have more teeth and longer geometries. The labyrinth balance drum studied in this dissertation has 15 interlocking teeth with 7 on the stator and 8 on the rotor. The dimensions of the balance drum are shown in Figure 2-10 and the built three-dimensional model is shown in Figure 2-11.

Boundary conditions in both stationary and rotating fames for the stepped labyrinth eye seal are summarized in Table 2-4. It is shown that the pressure drop for the balance drum seal is twice of that for the straight eye seal equipped in the same compressor.

Comparing Figure 1-4 to Figure 2-7, Figure 2-9, and Figure 2-11, it is noticeable that both an extended inlet and discharge path were employed for each seal. This revision on seal shape helps to reduce the effects of discharge flow in the simulation and thus improve the convergence.

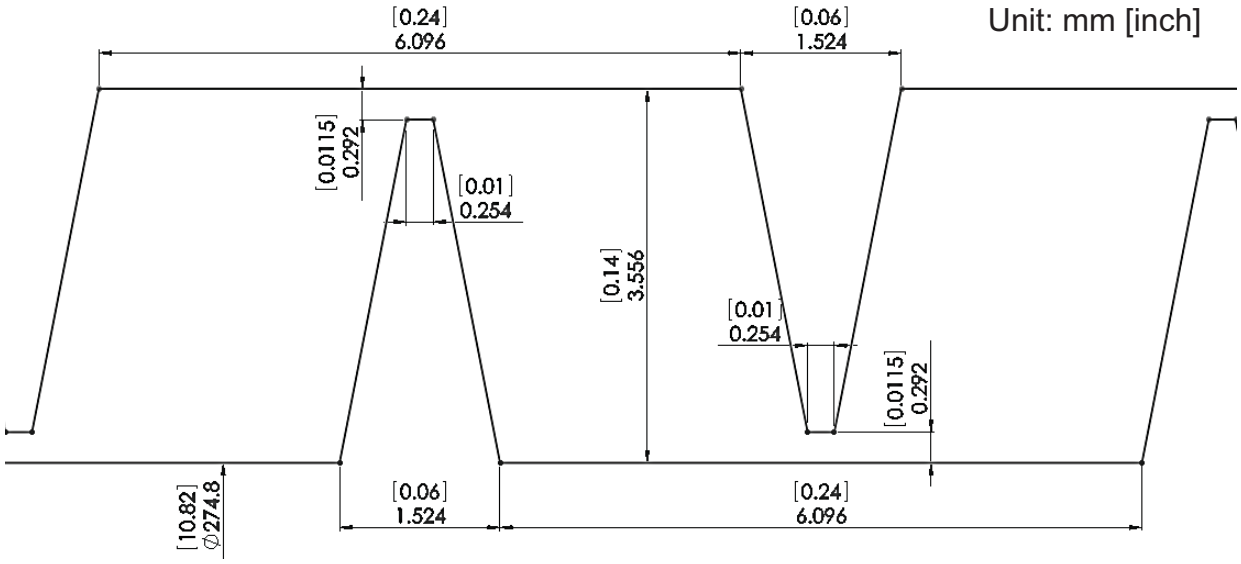

Figure 2-10 Dimension of the balance drum seal

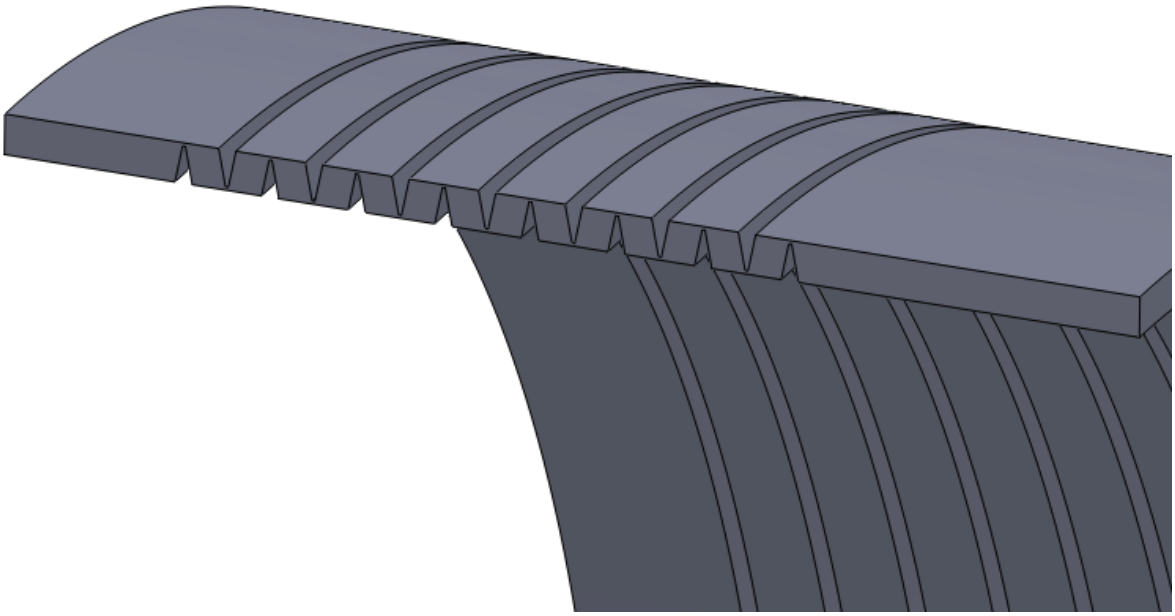

Figure 2-11 3-D model of the balance drum seal

Table 2-4 Boundary conditions for the balance drum seal

B.C's	In Stationary Frame	In Rotating Frame
Inlet pressure	7.584 MPa (1100 psi)	7.584 MPa (1100 psi)
Inlet temperature	366.7 K (660 R)	366.7 K (660 R)
Inlet velocity ratio	Subjected to change	Subjected to change
Desired pre-swirl rate	70%	70%
Outlet pressure	4.137 MPa (600 psi)	4.137 MPa (600 psi)
Frame rotating speed	0	Ω
Stator rotating speed	0	- Ω
Rotor whirl speed	Ω	0
Rotor spinning speed	1162 rad/s (11,097 rpm)	1162 rad/s (11,097 rpm)

Note: Ω = 0, 290.5, 581, 871.5, and 1162 rad/s

2.5 Meshing Scheme

It is very necessary to conduct a systematical grid study to obtain the optimal balance between calculation time and precision in CFD simulations. In this investigation, two grid study methods were applied: the grid independence study and the discretization error estimation. The straight eye seal will be employed as an example to explain the grid study process in section 2.5.1 and 2.5.2 while the grid study results of the stepped eye seal and balance drum seal will be presented in Appendix 1.

2.5.1 Grid Independence Study

Since high swirl rates and high eccentricities are involved in this research, the number of nodes in the circumferential direction was firstly studied. Table 2-5 shows that the required number of nodes in the circumferential direction is 144 to converge the residue to 10^{-5}. It may actually be not good enough for a high precision but it is the maximum number to use due to the restriction of computer memories.

Table 2-5 Nodes in circumferential direction required to converge

Pre-swirl rate	Number of nodes required in circumferential direction
0%	36
17.2%	72
62.6%	144

Since the node number in circumferential direction has been fixed as 144, only grids in radial and axial directions need to be studied. So it is not necessary to consider the eccentricity again and the model could be simplified to a quasi-three-dimensional model. Thus all the elements discussed below are two-dimensional elements but the nodes have circumferential velocities.

As shown in Figure 2-12, the desired number of nodes in radial and axial direction at chamber and tips were studied respectively. The method of best practice guidelines was applied and the results are shown in Figure 2-13 and Figure 2-14. Based on the result, the radial and axial node numbers at tips are set to be 16 and 11 respectively and the radial and axial node numbers at chambers are set to be 26 and 51 respectively. Figure 2-15 shows the mesh used for simulation in this research.

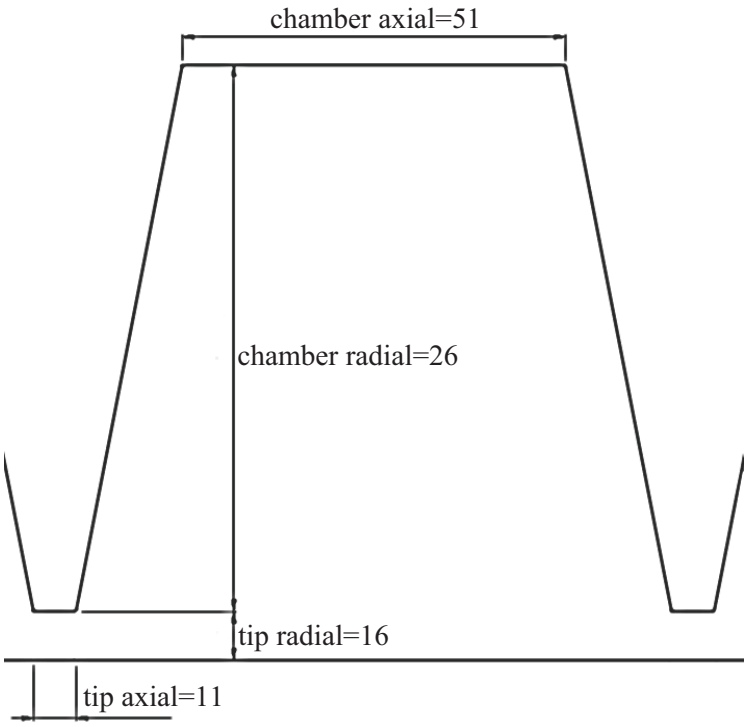

Figure 2-12 Node numbers in radial and axial direction

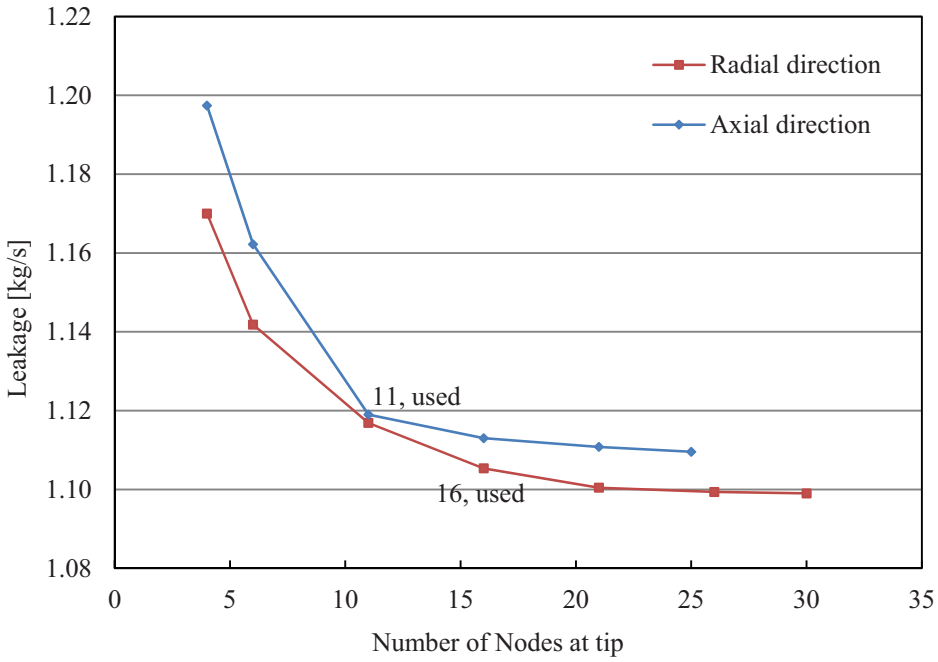

Figure 2-13 Grid independence study of nodes at tooth tip for the stepped eye seal

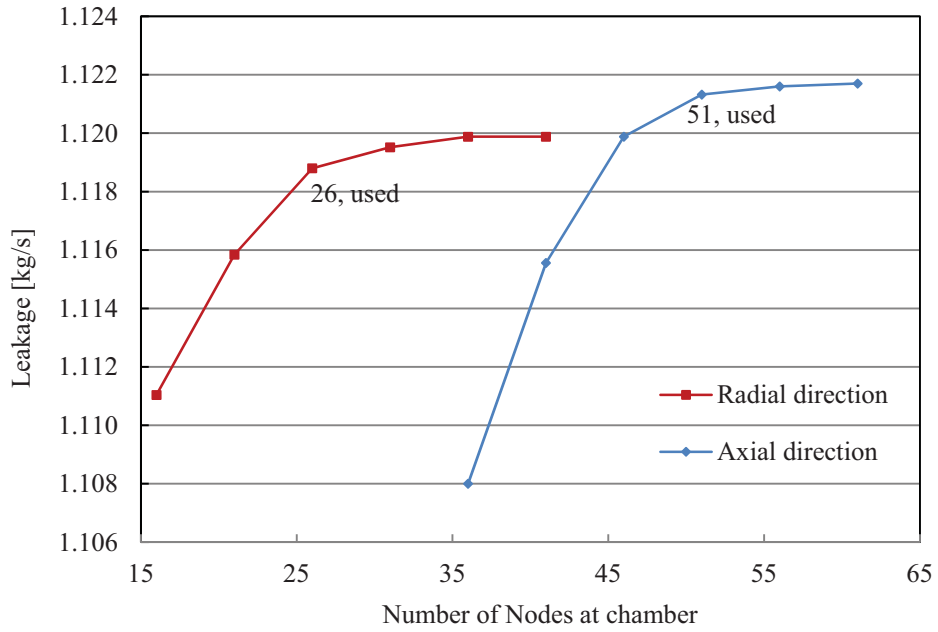

Figure 2-14 Grid independence study of nodes at chamber for the stepped eye seal

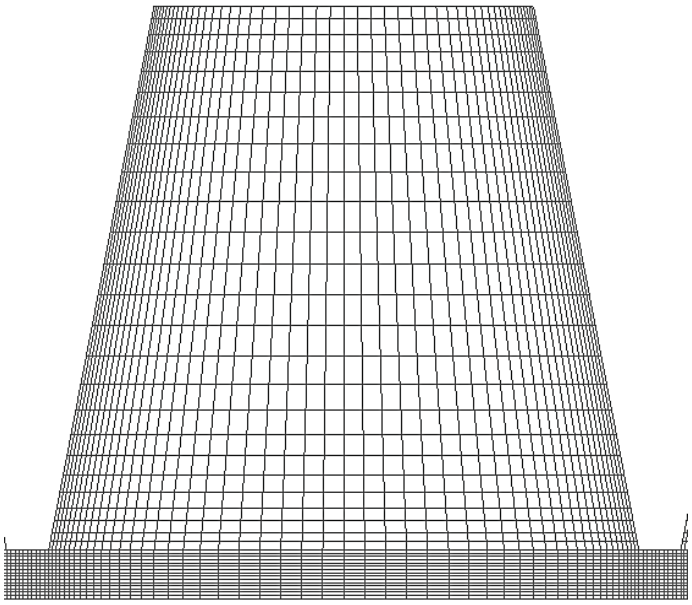

Figure 2-15 Mesh used for straight labyrinth eye seal

2.5.2 Discretization Error Estimation

In order to guarantee that discretization errors are small enough, the error estimation was also conducted with the systematical approach introduced by Roache [46, 47]. A courser and finer mesh were generated to compare with the mesh which was finally used in this research. The three mesh schemes are compared in Table 2-6.

Table 2-6 Comparison of the three meshes in each chamber for the straight eye seal

	Number of elements, *N*	**Average grid size, *h* (mm)**	**Refinement factor, *r***
Course	1217	0.093	1.33
Medium (used)	2150	0.070	1.30
Fine	3639	0.054	

In the table, the average grid size and refinement factor are defined as

$$h = \left[\frac{1}{N} \sum_{i=1}^{N} \Delta A_i \right]^{1/2} \tag{2.28}$$

$$r = \frac{h_1}{h_2} \tag{2.29}$$

where, A_i is the area of each element, the subscription 1 represents a courser mesh and the subscription 2 represents a finer mesh.

In this approach, the variable of apparent order, p is defined as

$$p = \frac{1}{\ln(r_{21})} \left| \ln \left| \varepsilon_{32} / \varepsilon_{32} \right| + q(p) \right| \tag{2.30}$$

$$q(p) = \ln \left(\frac{r_{21}^{p} - s}{r_{32}^{p} - s} \right) \tag{2.31}$$

$$s = 1 \cdot \mathrm{sgn}(\varepsilon_{32} / \varepsilon_{21}) \tag{2.32}$$

where $\varepsilon_{32} = \phi_3 - \phi_2$, $\varepsilon_{21} = \phi_2 - \phi_1$ and ϕ_k denotes the solution on the k^{th} grid. Note that $q(p) = 0$ for r = const. eq (2.30) and (2.31) can be solved using fixed-point iteration, with initial guess equal to the first term. Negative values of $\varepsilon_{32}/\varepsilon_{21}$ indicate oscillatory convergence, which was not detected in the discretization evaluation procedure in this research.

Then the approximate relative error is given by

$$e_a^{21} = \left| \frac{\phi_1 - \phi_2}{\phi_1} \right| \tag{2.33}$$

The grid convergence index (GCI) is defined as

$$\mathrm{GCI}_{\text{fine}}^{21} = \frac{1.25 e_a^{21}}{r_{21}^{p} - 1} \tag{2.34}$$

The profiles of velocities and estimated errors at the first teeth are compared from Figure 2-16 to Figure 2-19. Velocity results from the three meh schemes agree with each other very well.

The maximum GCI are 3.54%, 6.10%, 0.98%, and 1.36% respectively for axial, radial, tangential velocities, and pressure. Those GCI values are acceptable. The errors in Figure 2-16 to Figure 2-19 are computed by multiplying the GCI and velocity values from the medium mesh. Table 2-7 summarizes the discretization errors for the three models.

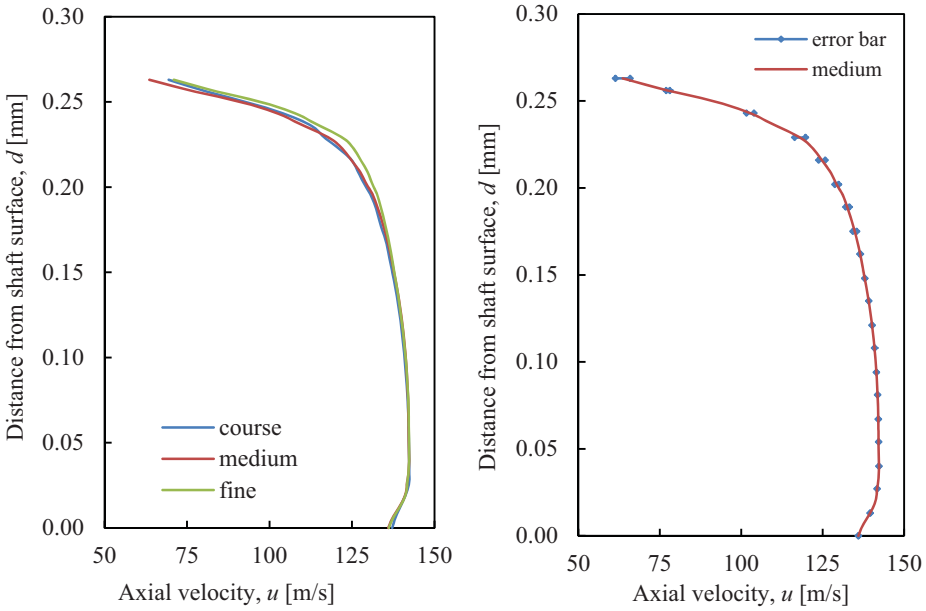

Figure 2-16 Axial velocity profile at the 1st tooth and errors

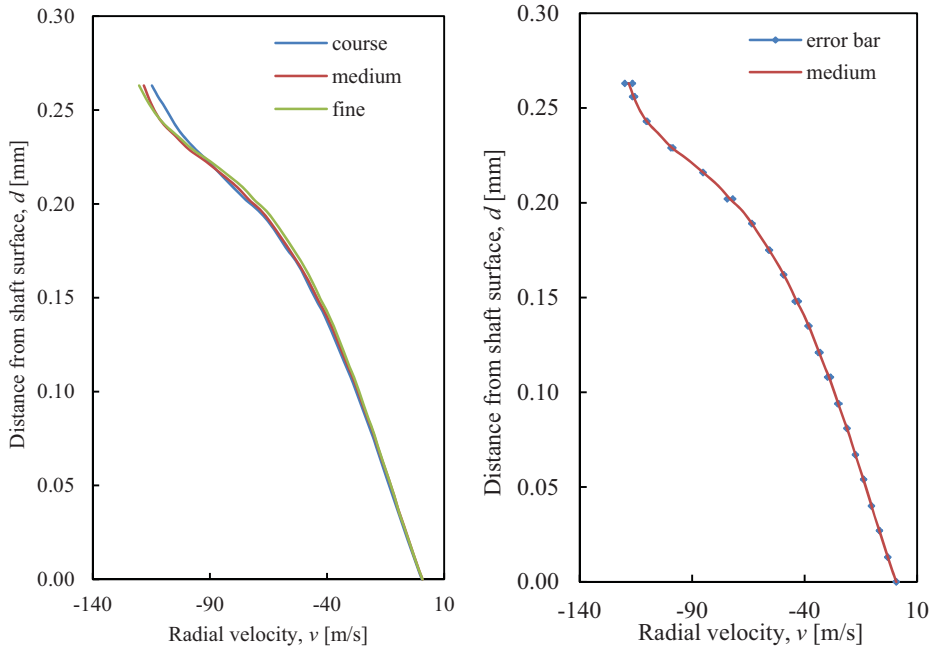

Figure 2-17 Radial velocity profile at the 1st tooth and errors

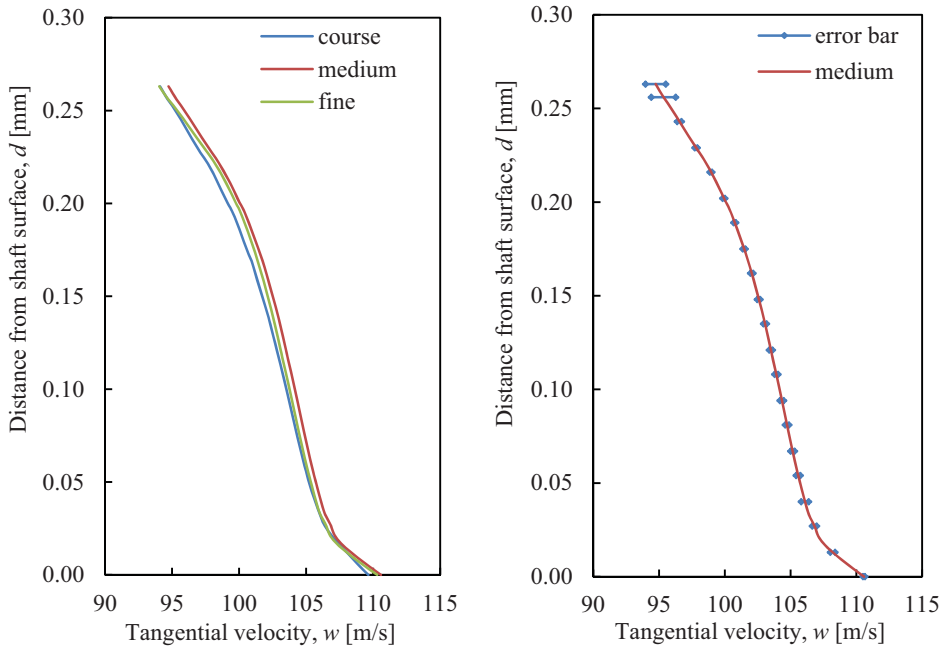

Figure 2-18 Tangential velocity profile at the 1st tooth and errors

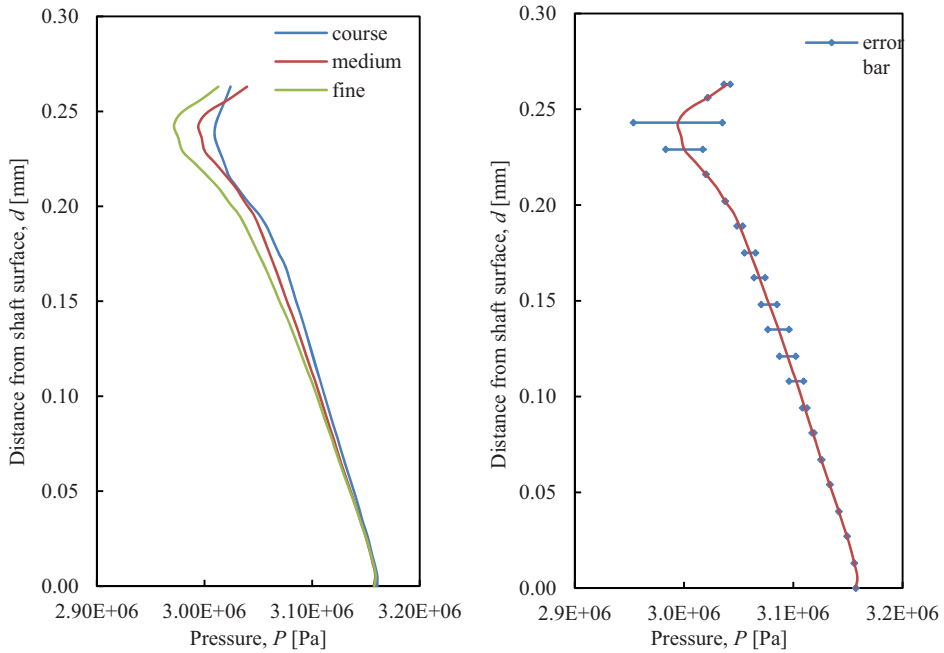

Figure 2-19 Pressure profile at the 1st tooth and errors

Table 2-7 Summary on the error estimation results

Models	Axial Velocity		Radial Velocity		Tangential Velocity		Pressure	
	GCI (%)	Error (m/s)	GCI (%)	Error (m/s)	GCI (%)	Error (m/s)	GCI (%)	Error (kPa)
Straight Eye Seal	3.54	2.26	6.10	4.78	0.98	0.93	1.36	41
Stepped Eye Seal	4.58	0.35	7.33	0.21	8.74	0.0007	0.0085	0.016
Balance Drum Seal	3.47	2.57	6.42	1.03	1.48	0.45	0.05	35

2.6 Verification of Model and Method

2.6.1 Comparison for the Straight Eye Seal

To verify the accuracy and reliability of the numerical model and method, the case with no pre-swirl and eccentricity of 0.1 was compared to bulk-flow and TASC flow results in [11] as shown in Figure 2-20 - Figure 2-22.

Figure 2-20 compares the numerically predicted pressure distribution with bulk-flow method and shows good agreement.

According to the linearized model given by eq. (4.2), data points in Figure 2-21 and Figure 2-22 can be approximated with linear lines. In Figure 2-21 intercepts are direct stiffness and slopes are cross-coupled damping, while in Figure 2-22 intercepts represent cross-coupled stiffness and slopes represent direct damping. Figure 2-21 shows that the three methods lead to the same cross-coupled damping but different direct stiffness; while Figure 2-22 shows good agreement on cross-coupled stiffness and direct damping among the three methods. The difference in Figure 2-21 can be neglected because direct stiffness and cross-coupled damping have very small influence on rotor stability and moreover it has been observed that the bulk-flow method usually gives a pessimistic prediction [36, 37, 44].

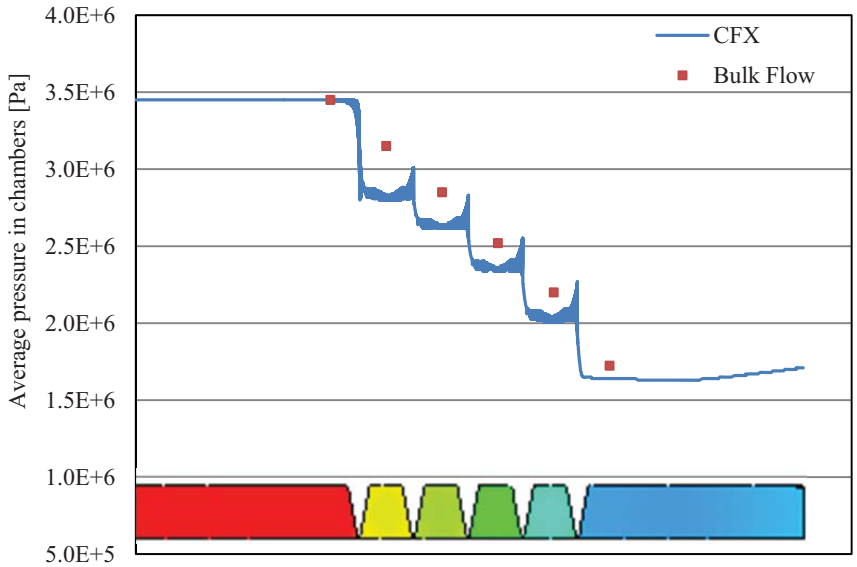

Figure 2-20 Comparison of predicted pressure distribution

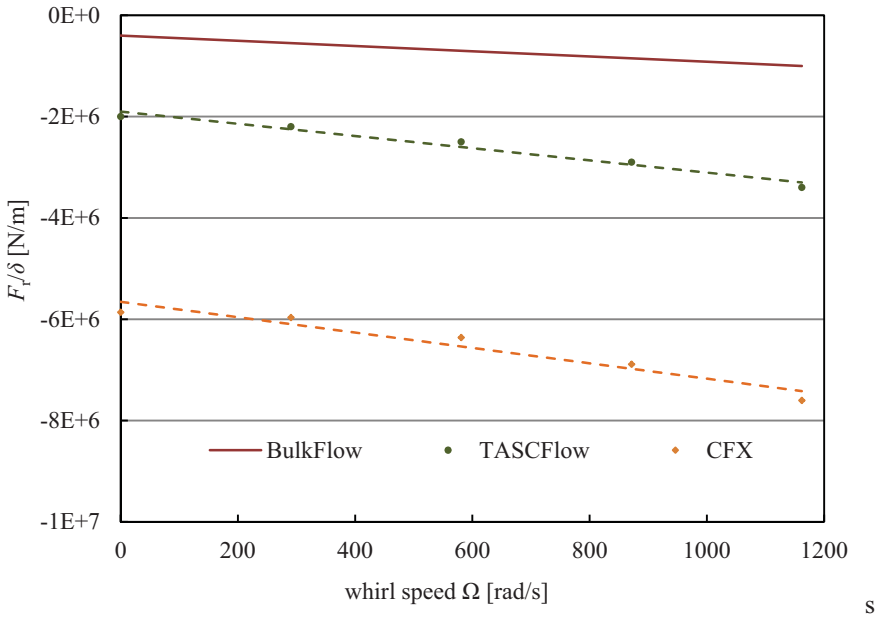

Figure 2-21 Comparison of predicted radial force with previous work (tooth-on-stator, 10% eccentricity, 3% pre-swirl)

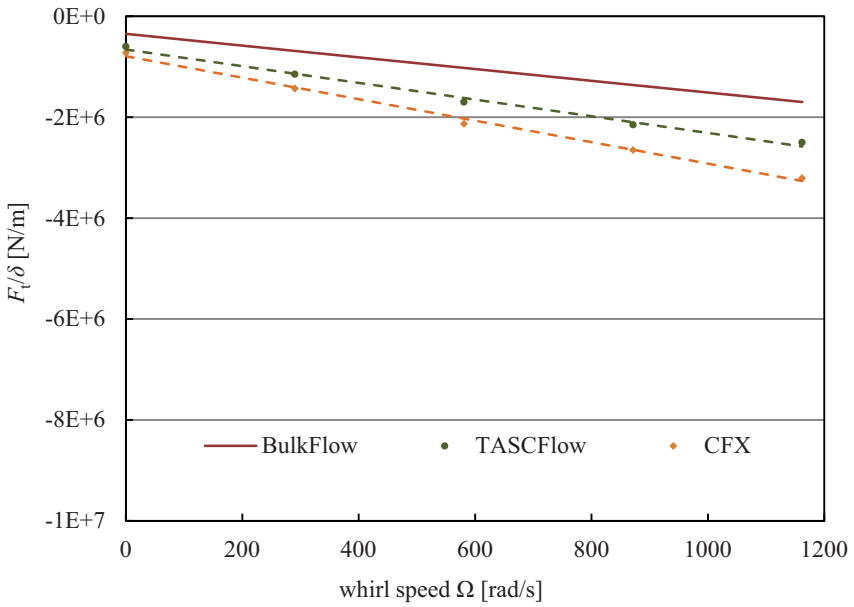

Figure 2-22 Comparison of predicted tangential force with previous work (tooth-on-stator, 10% eccentricity, 3% pre-swirl)

2.6.2 Comparison for the Stepped Eye Seal

One of the main reasons to calculate the stepped eye seal is that there are test data for comparison with the numerical results. To further verify the accuracy and reliability of the numerical approach, the leakages *vs*. pre-swirl rates were compared with test data in [17] and bulk-flow results. Then the direct and cross-coupled stiffness coefficients at different pre-swirls were also compared.

Figure 2-23 compares the leakage among the numerical, bulk-flow, and experimental results. The three ways show good agreement. It is noticeable that both CFX simulation result and test data show that the leakage decreases slightly with the increase of pre-swirl rate, while leakage given by the bulk-flow method is not sensitive to pre-swirl. The whirl speed of the rotor also has influence on the leakage. For a synchronously whirling rotor, the leakage may increase with the pre-swirl slightly, which will be further discussed in section 3.2.

The comparison of direct and cross-coupled stiffness among the three methods are shown in Figure 2-24 and Figure 2-25, in which the CFD stiffness coefficients are calculated with the linearized model given by eq. (4.2). In Figure 2-24, the three methods give close prediction on direct stiffness amplitudes and the same trend of increasing with pre-swirl. But the direct

stiffness tested by the experiment was positive while the other two methods give negative predictions. This may be because that the direction of radial force in the experiment has a different definition. Figure 2-25 shows the same trend for the cross-coupled stiffness. It's also shown that the cross-coupled stiffness given by CFX simulation is more sensitive to the pre-swirl. It indicates that the conclusion given by [36, 37, 44] that the bulk-flow method usually over predict the stiffness only works for low pre-swirl case. The CFD prediction may give bigger prediction when the pre-swirl rate is high.

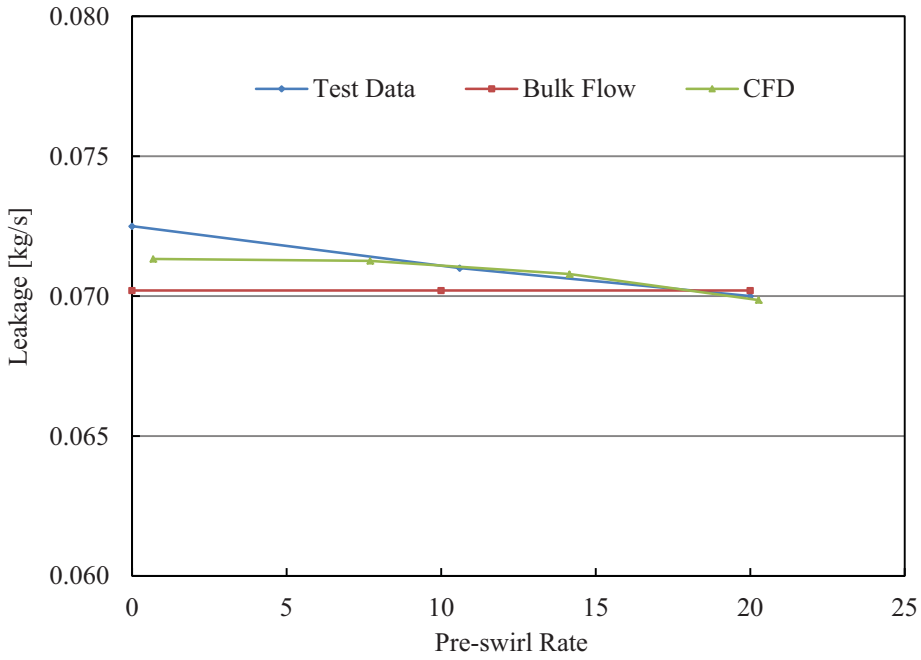

Figure 2-23 Comparison of leakage for the stepped eye seal

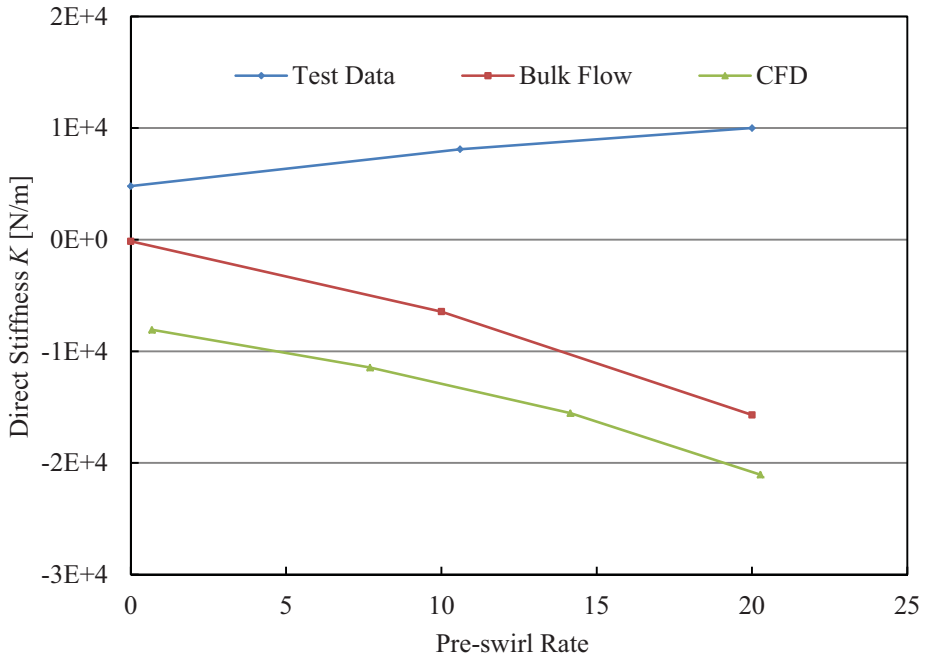

Figure 2-24 Comparison direct stiffness for the stepped eye seal

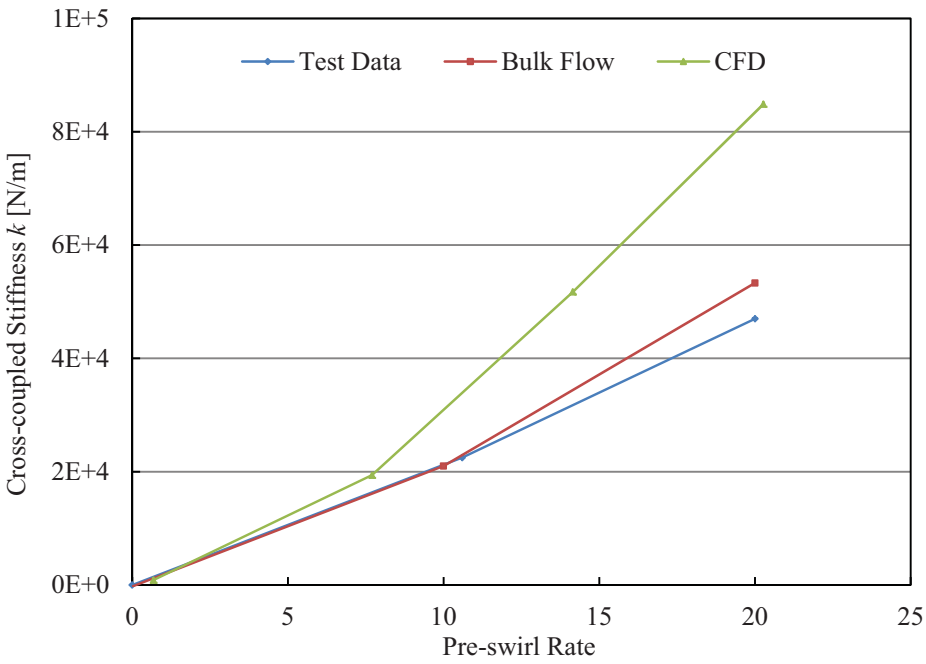

Figure 2-25 Comparison of cross-coupled stiffness for the stepped eye seal

2.7 Summary

In this chapter some numerical methods and models were firstly introduced including the rotating frame transfer, the k-ε turbulence model with curvature correction, the scalable wall function, and some assumptions on wall and working fluid.

Then three ways to generate pre-swirl were discussed. The ways by creating inlet path with special shapes turned out to be too complicated and time consuming. The method of using rough long inlet path has been proven to be not sufficient enough for a pre-swirl as high as 70%. The way by specifying the inlet velocity ratio turned out to be the best way and was finally used for the calculation on all models in this dissertation.

The three types of seals calculated in this dissertation including the straight eye seal, the stepped eye seal, and the balance drum seal were modeled in Solid Works and meshed in ICEM. The specialties and boundary conditions for each seal were discussed.

To obtain the optimal mesh, a systematical grid study was employed including two parts: the grid independence study and the discretization error estimation. The three seal models were finally solved in ANSYS-CFX. The numerical methods and models were verified and validated by comparing results with previous bulk-flow and test data.

3 Fluid Field Result Analysis

Even though the main objective of this research is to study rotordynamic characteristics of labyrinth seals, it is still necessary to analyze and discuss results of the fluid fields in seals. The accuracy of forces in the labyrinth seal will be guaranteed based on the reasonable fluid field obtained from the numerical simulation.

3.1 Pressure Distribution

The pressure distribution is a crucial overall property to determine the fluid field in the labyrinth seal and thus the pressure distribution will be firstly studied. Comparison of pressure between the CFX and the bulk-flow predictions for the straight eye seal has been shown in Figure 2-20 in last chapter for the purpose of model verification.

The pressure distributions for the stepped seal and the balance drum seal are separately shown in Figure 3-1 and Figure 3-2 and compared with bulk-flow result. The predictions given by CFX simulation agree with bulk-flow results very well; moreover the CFX results give more details on the pressure distribution. It is shown that the pressure mainly drops at tooth tips while remains stable in chambers. Figure 3-1 also shows that there is a small jump of the pressure at the leading edge of each tooth, which should be because that the flow is partially blocked at the tooth and then reverses back to the chamber. Figure 3-2 shows the similar results for the balance drum seal.

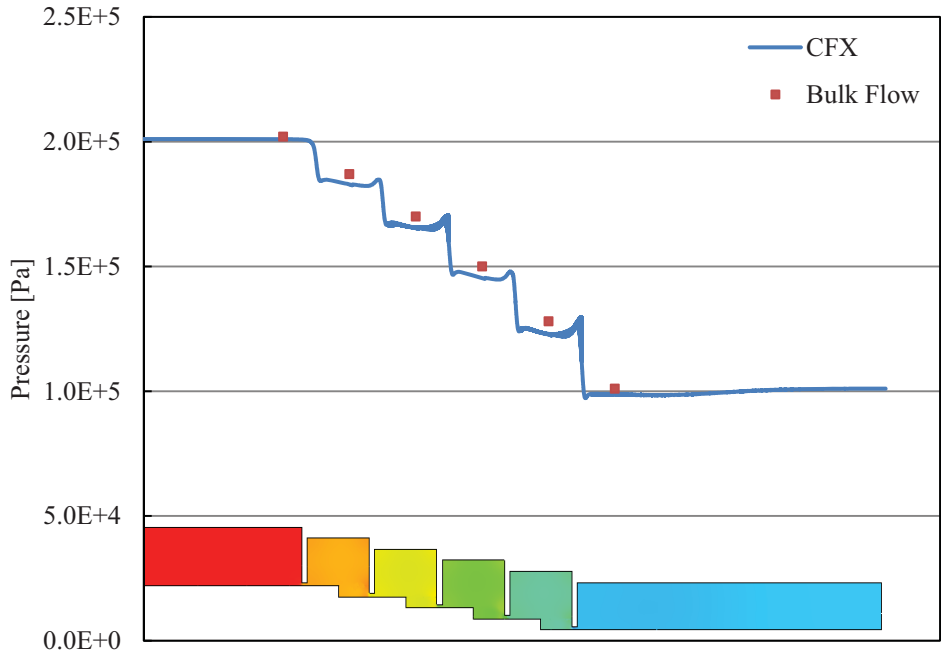

Figure 3-1 Comparison of predicted pressure distribution for the stepped seal

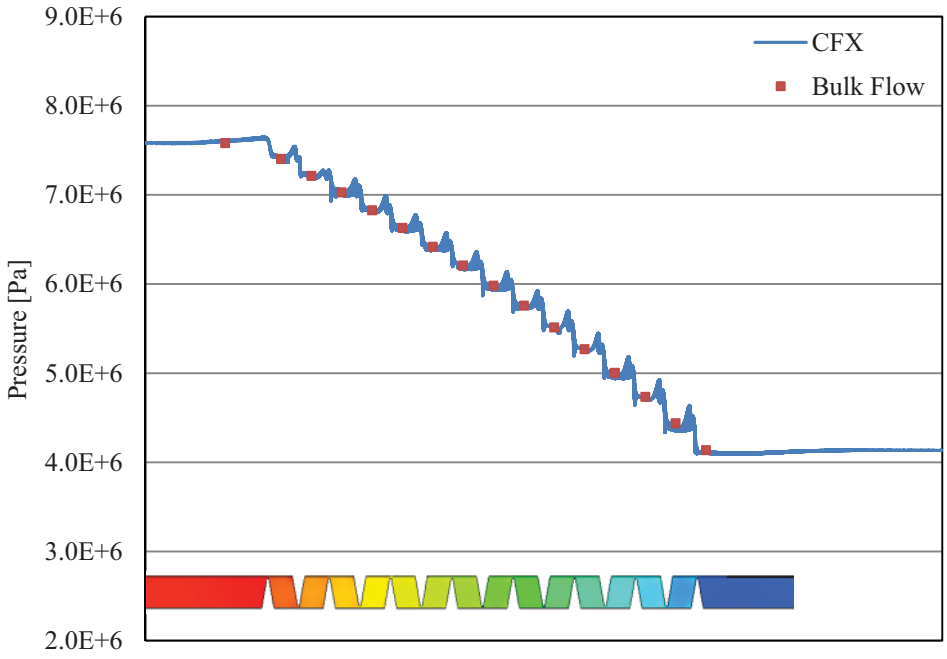

Figure 3-2 Comparison of predicted pressure distribution for the balance drum seal

3.2 Leakage

The leakage is another important overall property for the flow in the labyrinth seal. Furthermore the leakage is also a significant criterion to judge the quality of the seal. So it is of interest to study the influence of pre-swirl on the leakage. The leakage *vs.* pre-swirl for the stepped eye seal has been compared with the test data as shown in

Figure 3-3 and Figure 3-4 show that for both tooth-on-rotor and tooth-on-stator cases the pre-swirl basically has a very small influence on the leakage. The change rate caused by pre-swirl is only about 1% for all whirl speeds. However it is still noticeable that the leakage slightly increases with the pre-swirl except for the case of zero whirl speed. It is also shown that the whirl speed of the rotor also has slight influence on the leakage.

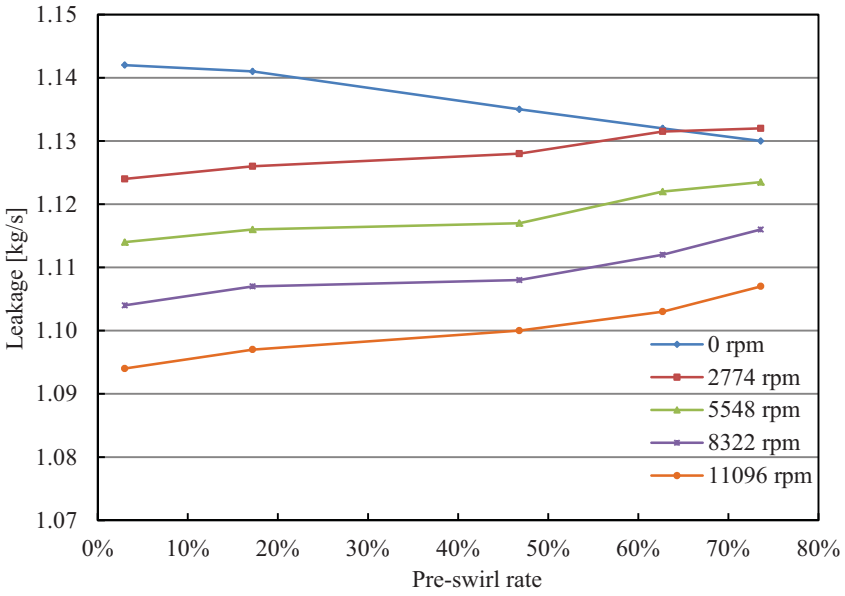

Figure 3-3 Predicted leakage *vs*. pre-swirl at different whirl speeds for the straight eye seal (tooth-on-stator, 0.1 eccentricity, 292 μm clearance)

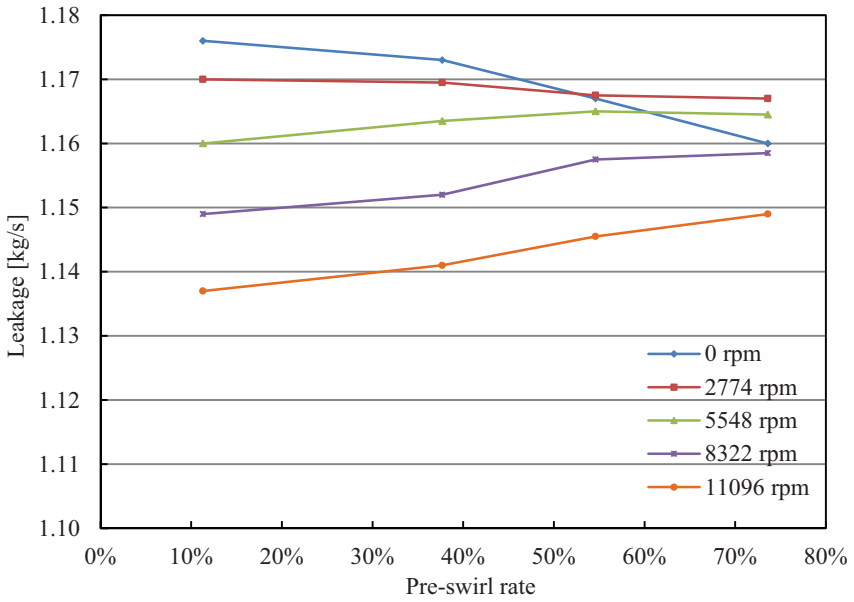

Figure 3-4 Predicted leakage *vs*. pre-swirl at different whirl speed for the straight eye seal (tooth-on-rotor, 0.1 eccentricity, 292 μm clearance)

Table 3-1 summarizes the comparison of predicted leakages for the three seals given by CAD and bulk-flow methods. The bulk-flow prediction is independent on the pre-swirl and the whirl speed. The CFX predicted leakage changes with pre-swirl and whirl speed very slightly thus the leakage with no pre-swirl or whirl speed were used for the comparison. It is shown that the predictions given by the two methods generally agree.

Table 3-1 Comparison of predicted leakage with bulk-flow result

Seal Models	Bulk Flow (kg/s)	CFX (kg/s)	Difference (%)
Tooth-on-stator straight eye seal	1.28	1.14	10.78
Stepped eye seal	0.0702	0.0713	1.57
Balance Drum	0.95	1.03	8.42

3.3 Flow Details

3.3.1 The Small Vortex

There are two vortices detected in each chamber for the straight eye seal with both tooth-on-stator and tooth-on-rotor configurations, as shown in Figure 3-5 and Figure 3-6. The big vortex in the center of each chamber is the usual one and the existence has been proven by previous researchers. However the small vortex downstream the each tooth has never been reported before and can be observed in all cases for the straight eye seal. The small vortex grows slightly when pre-swirl rate and eccentricity increase.

However the second small vortex has not been detected in the stepped eye seal and the balance drum seal as shown in Figure 3-7. It indicates that the small vortex may be related to the tooth profile and if so the discovery of this small vortex may be helpful for improving seal design in the future.

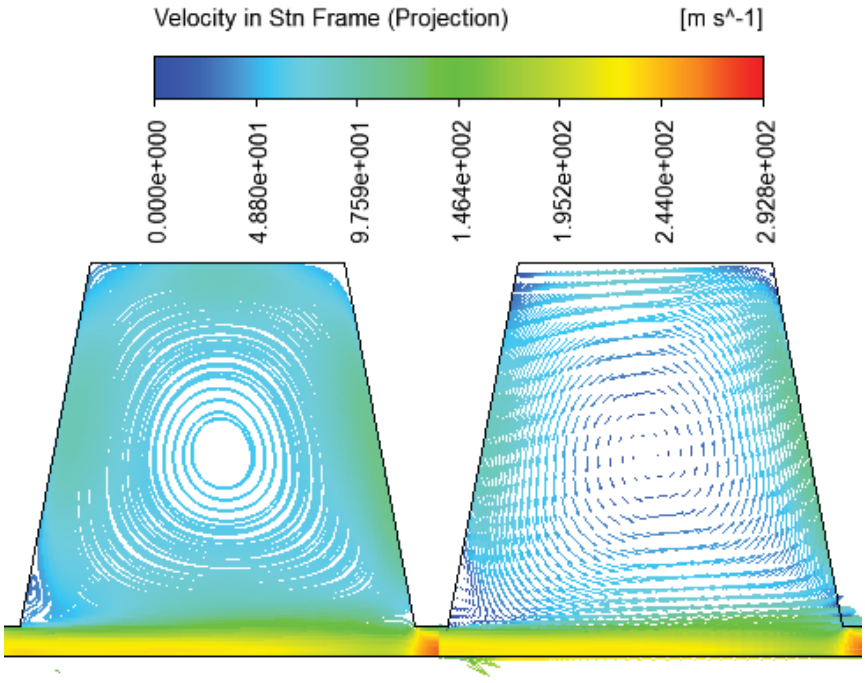

Figure 3-5 Predicted stream lines and vectors in the last chamber (tooth-on-stator, 73.6% pre-swirl rate)

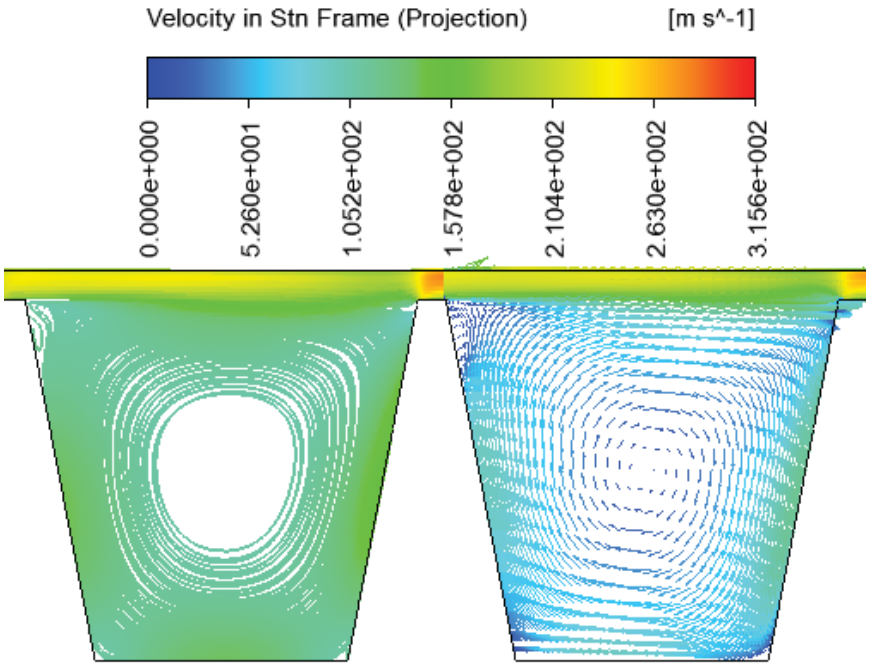

Figure 3-6 Predicted stream lines and vectors in the last chamber (tooth-on-rotor, 75.3% pre-swirl rate)

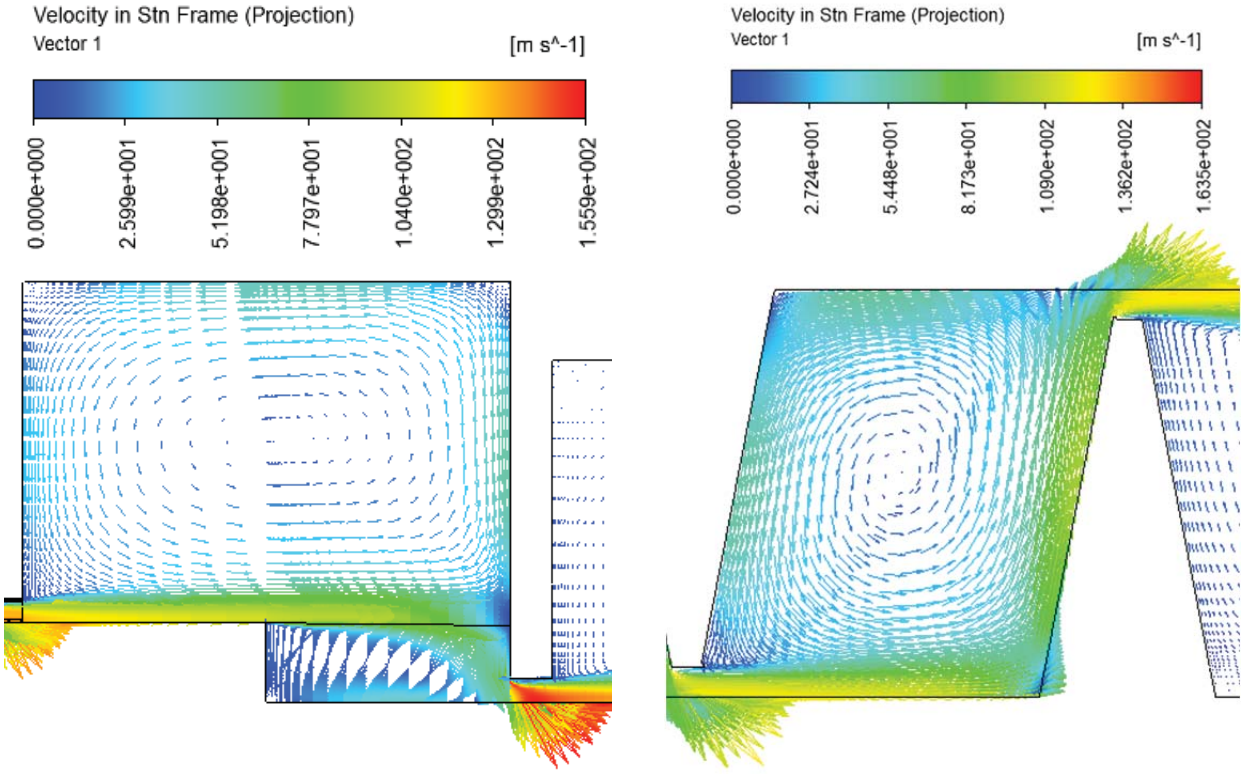

(a) the stepped eye seal (b) the balance drum seal

Figure 3-7 Predicted vectors in the last chamber for the stepped and balance drum seals

3.3.2 The Discharge Region

Velocity vectors leaving the last tip of the eye seal for the eccentricity of 0.7 are shown in Figure 3-8. The part (a) is the side with minimum clearance caused by eccentricity while the part (b) is the side with maximum clearance. The fluid at the side with minimum clearance is blocked by higher pressure generated by the smaller clearance and thus more fluid leaves the seal at the side with maximum clearance at higher velocity.

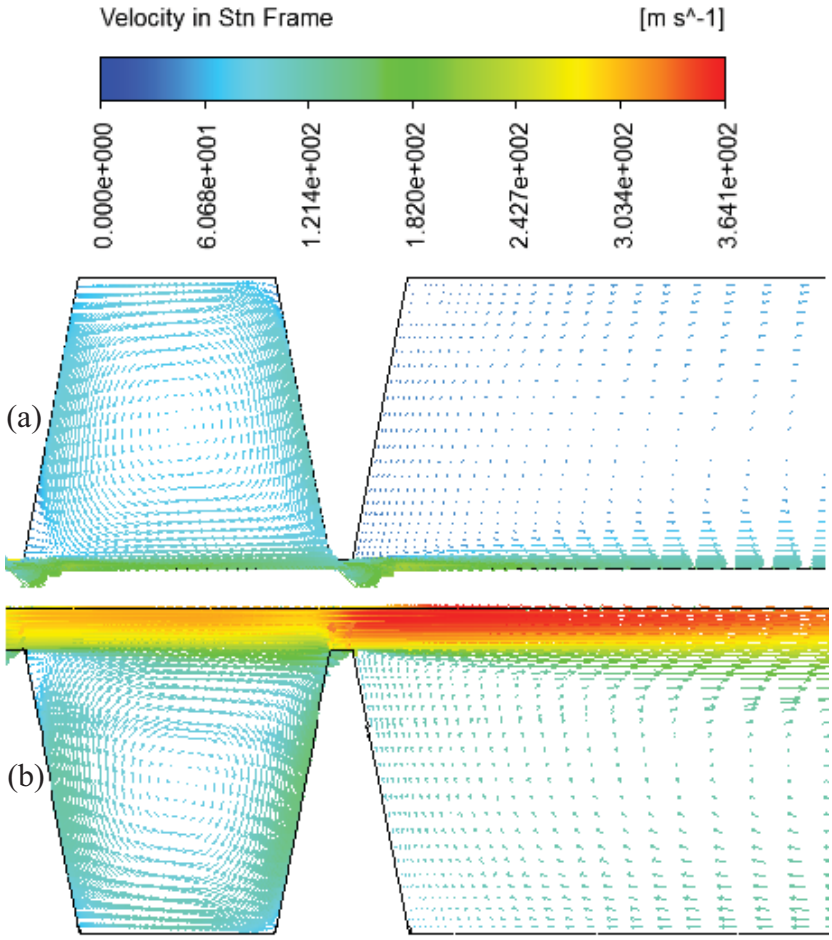

Figure 3-8 The difference of velocities leaving the seal at high eccentricity

(a) shows the plane of minimum clearance and (b) shows the plane of maximum clearance (tooth-on-stator, 0.7 eccentricity, 73.6% pre-swirl rate, 0 whirl speed)

3.3.3 The Spiral Flow in Chambers

Figure 3-9 shows that the gas flows into the chamber in a spiral pattern with very large circumferential velocity components. For a real seal, the pre-swirl is caused by the rotating rotor or shunt injection; while in this simulation it was generated by specifying the velocity ratio at inlet. The pre-swirl rate reached 73.6% for tooth-on-stator and 75.3% for tooth-on-rotor cases in this study.

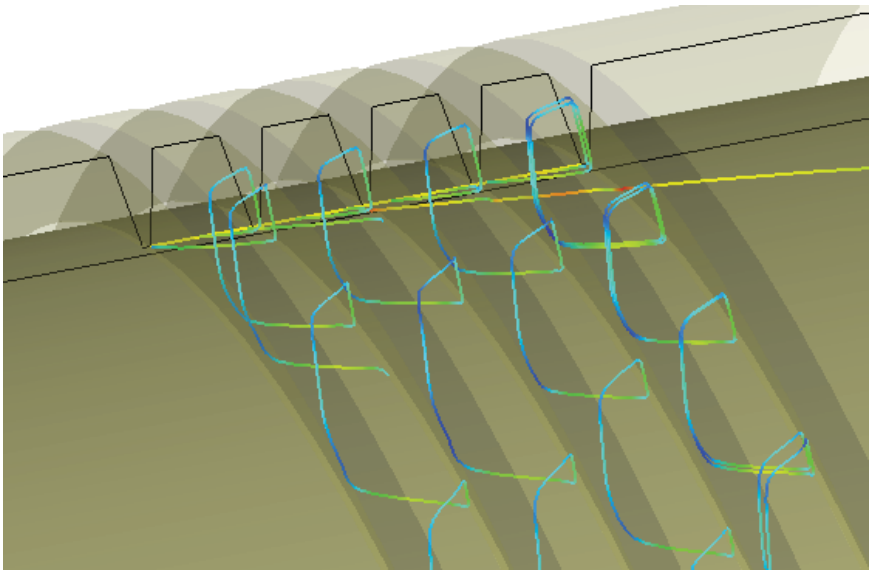

Figure 3-9 3-D Stream lines in chambers (tooth-on-stator, 73.6% pre-swirl rate)

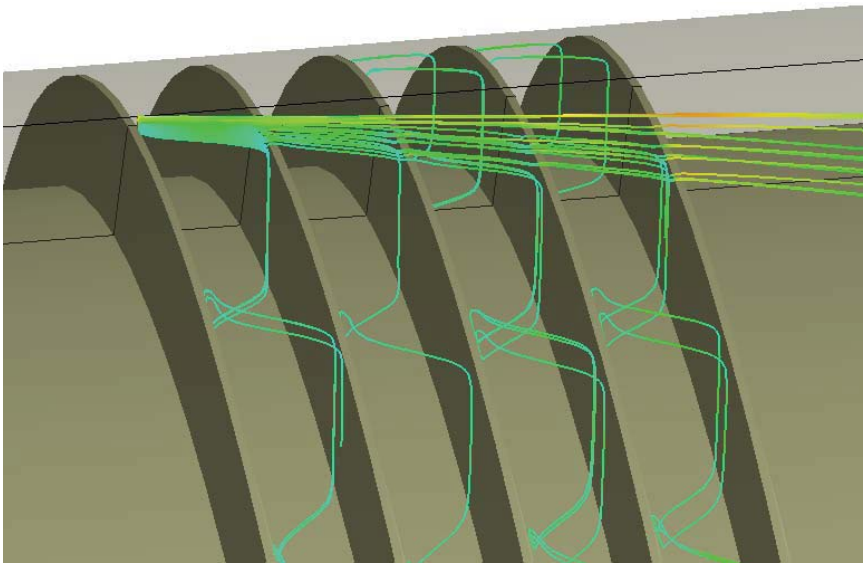

Figure 3-10 3-D Stream lines in chambers (tooth-on-rotor, 75.3% pre-swirl rate)

3.4 Summary

To guarantee the afterward rotordynamic analysis, the fluid field results from the numerical simulation in ANSYS-CFX were presented and discussed in this chapter. Some conclusions can be obtained below:

1) The pressure distributions predicted by the CFD and bulk-flow methods agree very well. It is noticeable that the pressure drops are mainly at tooth tips and there is a small increase for the pressure upstream each tooth.

2) The leakage given by CFD agrees with bulk-flow results for each model. Moreover, it is also shown that the leakage is slightly affected by the whirl speed and pre-swirl.

3) A second small vortex was detected downstream the tooth in each chamber in both the tooth-on-stator and tooth-on-rotor straight eye seal models. However it is not found in the other two models, which may indicate that the small vortex is tooth profile dependent. If so the discovery of this small vortex may be helpful for improving seal design in the future.

4) For the large eccentricity of 0.7 which is the maximum eccentricity involved in this research, the leakage flow at the side with minimum clearance is blocked by higher pressure generated by the smaller clearance and thus more fluid leaves the seal at the side with maximum clearance at higher velocity.

5) The gas flows into the chamber in a spiral pattern with very large circumferential velocity components.

4 Rotordynamic Coefficients Prediction

4.1 The First-Order Rotordynamic Model

The first-order model given by eq (4.1) has been widely used till now. It can be further simplified. Assuming that the rotor is whirling at the speed Ω with an offset of δ as shown in Figure 4-1, the location of the rotor can be given as

$$\begin{aligned} x &= \delta\cos(\Omega t) \\ y &= \delta\sin(\Omega t) \end{aligned} \tag{4.1}$$

For simplification, the frame can be defined in the way that the center of the rotor always locates on the x axis as shown in Figure 4-1. Then by substituting eq (4.1) into eq (1.1), it can be simplified as

$$\begin{aligned} F_r/\delta &= -K - c\Omega \\ F_t/\delta &= k - C\Omega \end{aligned} \tag{4.2}$$

where F_r is the seal force in the radial direction (F_x actually) and F_t is the seal force in the tangential direction (F_y actually).

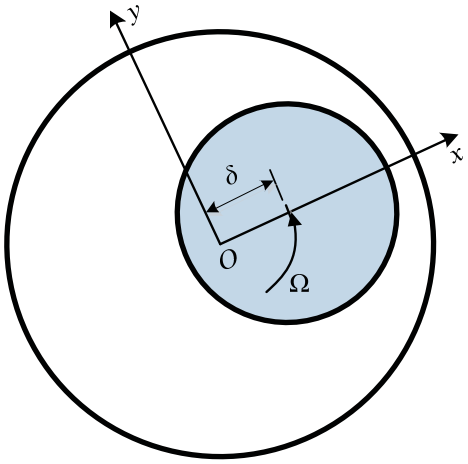

Figure 4-1 Whirl of the rotor

Eq (4.2) is more commonly used in rotordynamic analysis. The four rotordynamic coefficients in it have significant influences on the stability of the seal rotor system. Usually the bigger the cross-coupled stiffness k is, the more unstable the rotor is; while larger direct damping C helps to keep the rotor stable. So it is required to predict the four coefficients for a precise rotordynamic analysis on the rotor-bearing-seal system.

Obviously, to predict the four coefficients, radial and tangential forces on the rotor must be solved accurately. Integrated forces in specific directions on the rotor can be obtained in the post-processor of ANSYS-CFX. Since the numerical method of simulating the flow in labyrinth seals has been verified and the results of fluid field have been analyzed, forces extracted from the simulation should be exact enough and valid for further rotordynamic analysis.

Data points plotted in Figure 2-21 and Figure 2-22 are approximated by the first-order model, eq (4.2). It's shown that the first-order model is valid for cases with low pre-swirl.

4.2 The Second-Order Rotordynamic Model

Figure 4-4 and Figure 4-5 show the radial and tangential forces *vs.* whirl speed. Data points from numerical simulation are approximated with solid straight lines based on the first-order model. It's shown that the first-order model fits data points more and more poorly with the increase of pre-swirl rate. However, data points are much better approximated by dashed lines based on a quadratic equation.

It indicates that linearized model, eq (4.2), works well for low pre-swirl cases but does not accurately reflect the characteristics of high pre-swirl cases. Thus a second-order model including inertia terms is required to describe the dynamic behaviors of labyrinth seal at high pre-swirl rates:

$$-\begin{Bmatrix} F_x \\ F_y \end{Bmatrix} = \begin{bmatrix} K & k \\ -k & K \end{bmatrix} \begin{Bmatrix} x \\ y \end{Bmatrix} + \begin{bmatrix} C & c \\ -c & C \end{bmatrix} \begin{Bmatrix} \dot{x} \\ \dot{y} \end{Bmatrix} + \begin{bmatrix} M & m \\ -m & M \end{bmatrix} \begin{Bmatrix} \ddot{x} \\ \ddot{y} \end{Bmatrix} \tag{4.3}$$

where M and m are inertia coefficients coming from the flow and should be related to whiling speed, pre-swirl rate, and etc. Applying the same approach used for simplifying eq (1.1), eq (4.3) becomes

$$F_r/\delta = -K - c\Omega + M\Omega^2$$
$$F_t/\delta = k - C\Omega - m\Omega^2 \tag{4.4}$$

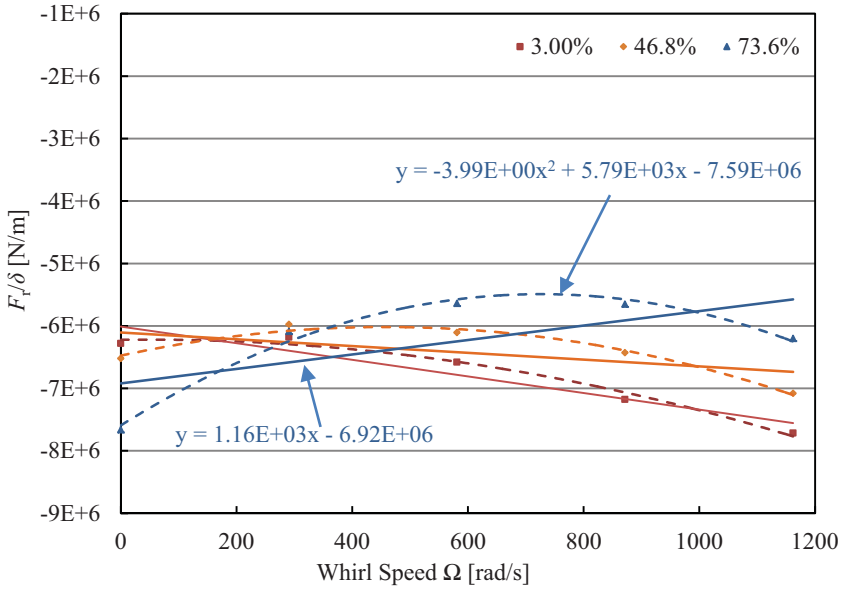

Figure 4-2 Predicted radial seal force *vs*. whirl speed at different pre-swirl rates (tooth-on-stator, 0.1 eccentricity)

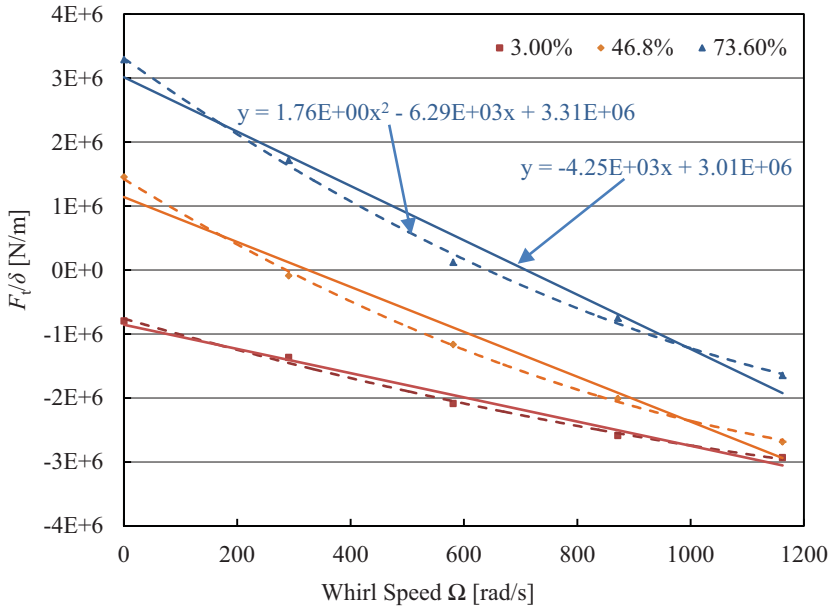

Figure 4-3 Predicted tangential seal force *vs*. whirl speed at different pre-swirl rates (tooth-on-stator, 0.1 eccentricity)

Table 4-1 further compared the rotordynamic coefficients solved based on the first-order and the second-order models. In this research, all results will be analyzed using the second-order model. However rotordynamic coefficients solved with the first-order model for all cases involved in this research will be listed in the Appendix 2 for comparison.

Table 4-1 Rotordynamic coefficients for the straight eye seal (0.1 eccentricity and 292μm clearance)

Pre-swirl Rate	Direct Stiffness K (N/m)		Cross-coupled Damping c (N·s/m)		Cross-coupled Stiffness k (N/m)		Direct Damping C (N·s/m)	
	1st order model	2st order model	1st order model	2st order model	1st order model	2st order model	1st order model	2st order model
3.00%	6.01×10^{6}	6.22×10^{6}	1.33×10^{3}	-1.21×10^{2}	-8.56×10^{5}	-7.6×10^{5}	1.89×10^{3}	2.55×10^{3}
46.8%	6.11×10^{6}	6.48×10^{6}	5.41×10^{2}	-2.00×10^{3}	1.14×10^{6}	1.42×10^{6}	3.51×10^{3}	5.44×10^{3}
73.6%	6.92×10^{6}	7.59×10^{6}	-1.16×10^{3}	-5.79×10^{3}	3.01×10^{6}	3.31×10^{6}	4.25×10^{3}	6.29×10^{3}

4.3 Q-Factor

The Q-Factor is an important criterion to determine the rotordynamic stable properties of labyrinth seals. It is defined as

$$Q = k - C\omega_{\text{ncr}} \tag{4.5}$$

where ω_{ncr} is the first-order critical speed of the rotor.

Usually the smaller the Q-Factor is the better dynamic property the seal has. If Q-Factor is negative, it means that the labyrinth seal helps to keep the rotor system stable; oppositely the labyrinth seal drives the rotor to move if the Q-Factor is positive.

The Q-Factor will be calculated for the straight eye seal and the balance drum seal. The first-order critical speed of the rotor as shown in Figure 1-4 usually lands between 3000 rpm to 4000 rpm. For all the calculation in this dissertation, ω_{ncr} = 419 rad/s (4000 rpm).

4.4 Tooth-on-Stator Straight Eye Seal

The straight eye seal were firstly calculated to study some basic properties of the labyrinth seal due to the simplicity of its geometry. The influencing factors such as pre-swirl, eccentricity, clearance, and tooth location were studied using a series of models built based on the prototype shown in Figure 2-6.

4.4.1 Pre-Swirl

Forces *vs*. whirl speeds for different pre-swirl rates are shown in Figure 4-4 and Figure 4-5. Dashed curves are approximation for data points based on the second-order model, eq (4.4). Rotordynamic coefficients can be read from the equation of the curves and they are shown in Figure 4-6 and Figure 4-7.

Figure 4-6 shows that both direct and cross-coupled stiffness are increased with the increasing pre-swirl rate. Note that the direct stiffness seems to be decreased in Figure 4-4, but the amplitudes are actually increased. Figure 4-7 shows that the direct damping is increased but the cross-coupled damping is decreased with the increasing pre-swirl rate.

It is noticeable in Figure 4-7 that the cross-coupled stiffness even increases from negative to positive, which adds an unstable factor to the rotor but the increase of direct damping serves to make the rotor more stable. In this case, the Q-Factor could give an overall prediction on the stability property of the seal. Figure 4-8 shows that the Q-Factor increased from negative to positive with the pre-swirl which means that the rotor stability is decreased by the seal because of the pre-swirl. So we can conclude that the labyrinth seal could drive the rotor unstable at high pre-swirl.

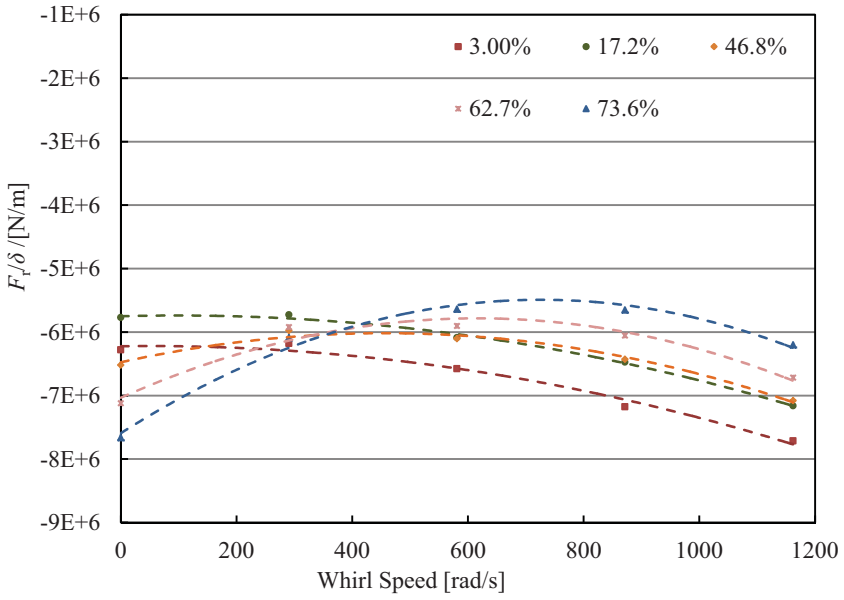

Figure 4-4 Predicted radial seal force *vs*. whirl speed at different pre-swirl rates (tooth-on-stator, 0.1 eccentricity)

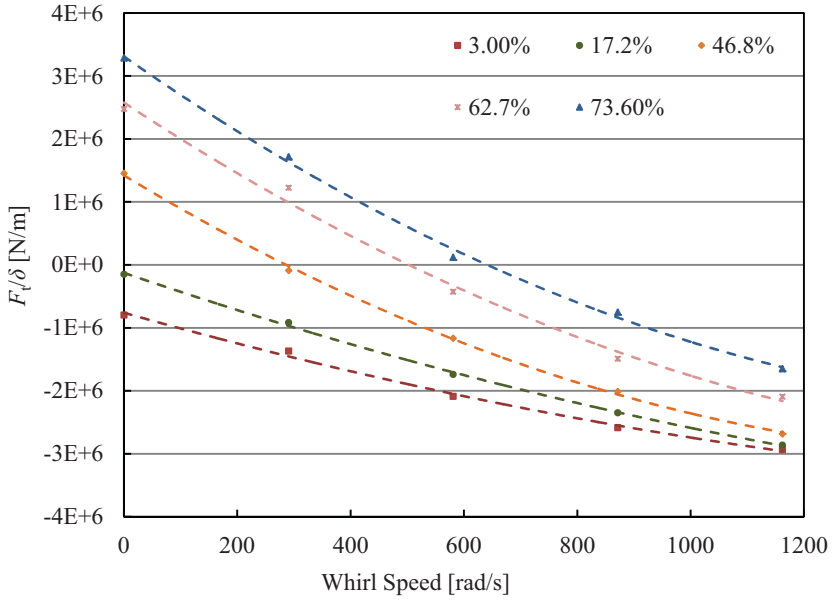

Figure 4-5 Predicted tangential seal force *vs*. whirl speed at different pre-swirl rates (tooth-on-stator, 0.1 eccentricity)

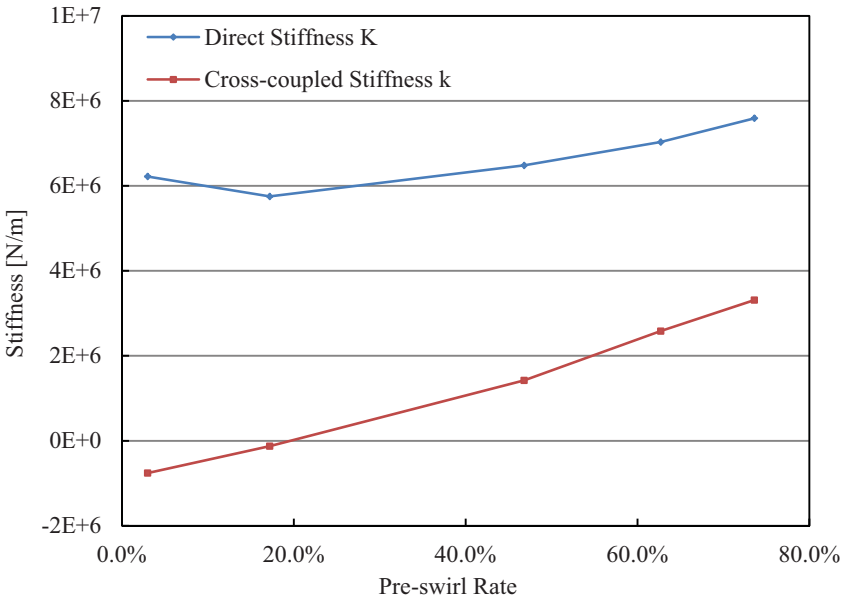

Figure 4-6 Predicted stiffness *vs*. pre-swirl rate (tooth-on-stator, 0.1 eccentricity)

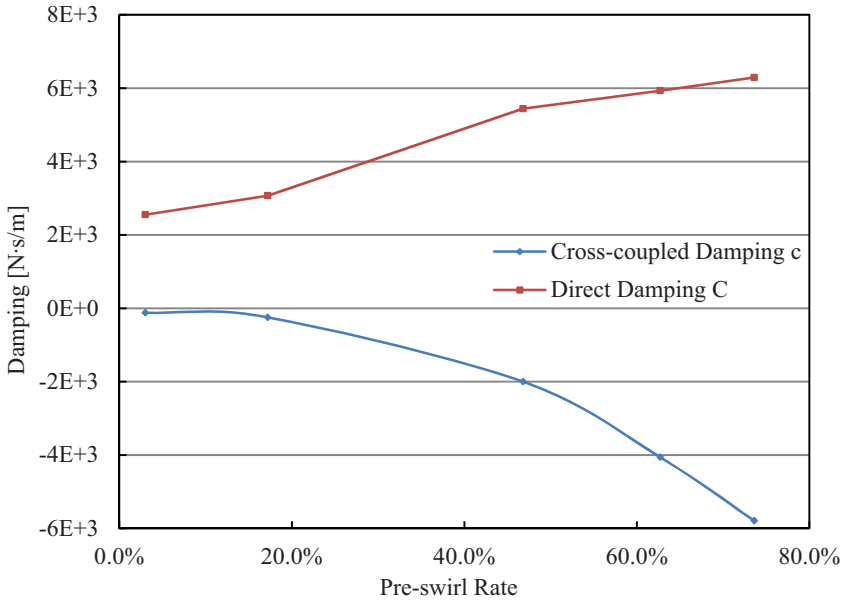

Figure 4-7 Predicted damping *vs*. pre-swirl rate (tooth-on-stator, 0.1 eccentricity)

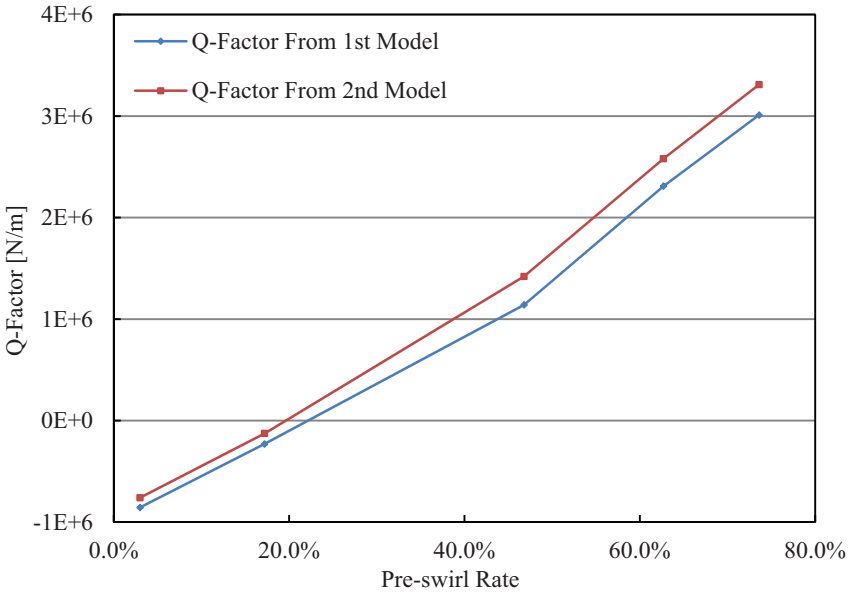

Figure 4-8 Q-Factor *vs*. pre-swirl rate (tooth-on-stator, 0.1 eccentricity)

4.4.2 Eccentricity

To study the influence of eccentricity on rotordynamic properties of the labyrinth seal, a set of models based on the dimensions shown in Figure 2-6 with eccentricities ranging from 10% to 70% were modeled and solved.

Figure 4-9 and Figure 4-10 show the radial and tangential forces on rotor *vs*. whirl speed for different eccentricities in the low pre-swirl condition. It's noticeable that eccentricity has very small influence on the behavior of tangential forces. While Figure 4-11 and Figure 4-12 show the forces on rotor *vs*. whirl speed for different eccentricities in the high pre-swirl condition. In this case, both radial and tangential forces on the rotor are affected by eccentricity.

Data points in Figure 4-9 to Figure 4-12 were approximated with the second-order model and the results are compared in Figure 4-13 to Figure 4-16. Figure 4-13 and Figure 4-14 show that the increase of eccentricity leads to a drop of direct stiffness and cross-coupled stiffness at 74% pre-swirl rate while changes are much smaller at the 3% pre-swirl rate. This also indicates that the pre-swirl could enhance the influence of eccentricity on both direct and cross-coupled stiffness. Actually the forces on the rotor are bigger to drag the rotor back when the rotor is farther away from the center, but the stiffness decrease slightly considering the stiffness is force divided by eccentricity.

Figure 4-15 shows that the cross-coupled damping decreases with eccentricity when the pre-swirl rate is low however it increases significantly with eccentricity in a high pre-swirl condition. In Figure 4-16, the direct damping doesn't show too much change with the increase of eccentricity in low pre-swirl condition however it drops significantly in high pre-swirl condition, which decreases the stability of the rotor.

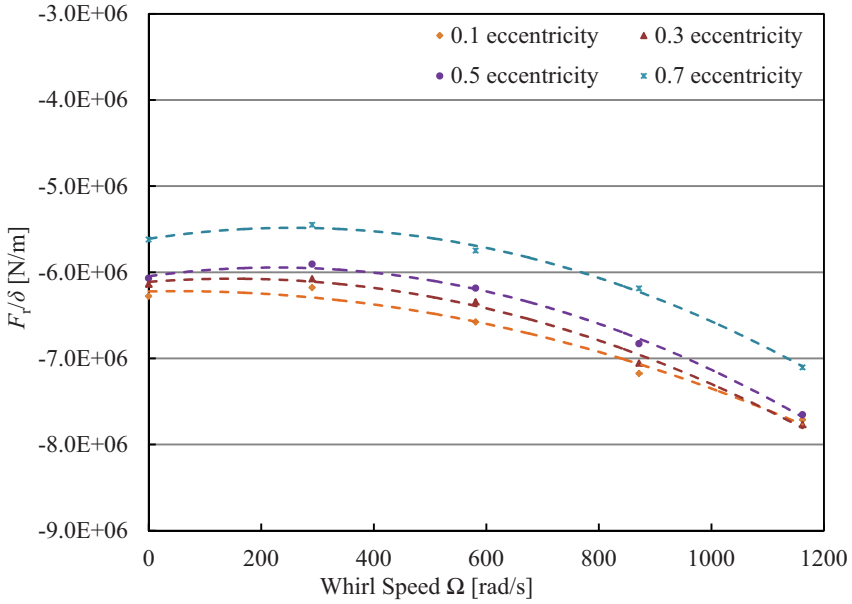

Figure 4-9 Predicted radial seal force *vs*. whirl speed at different eccentricities (tooth-on-stator, 3.0% pre-swirl rate)

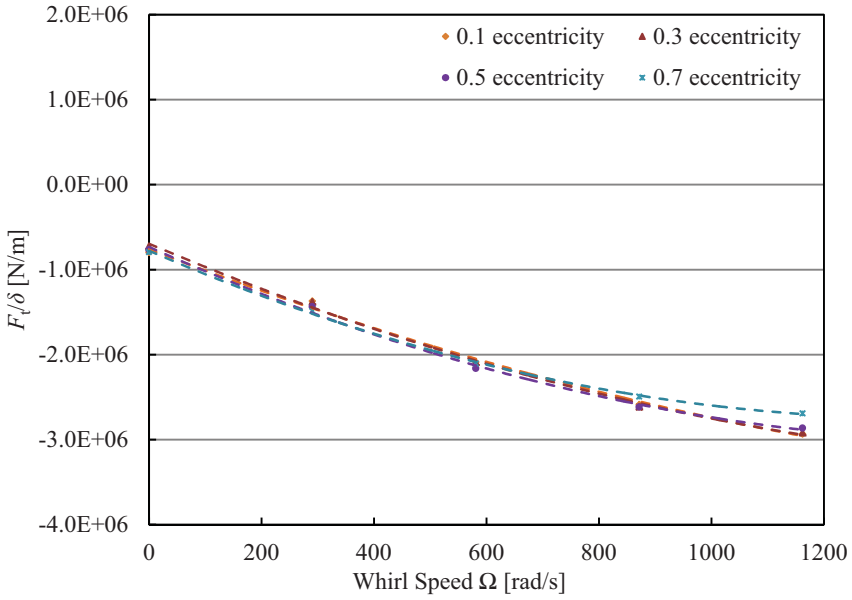

Figure 4-10 Predicted tangential seal force *vs*. whirl speed at different eccentricities (tooth-on-stator, 3.0% pre-swirl rate)

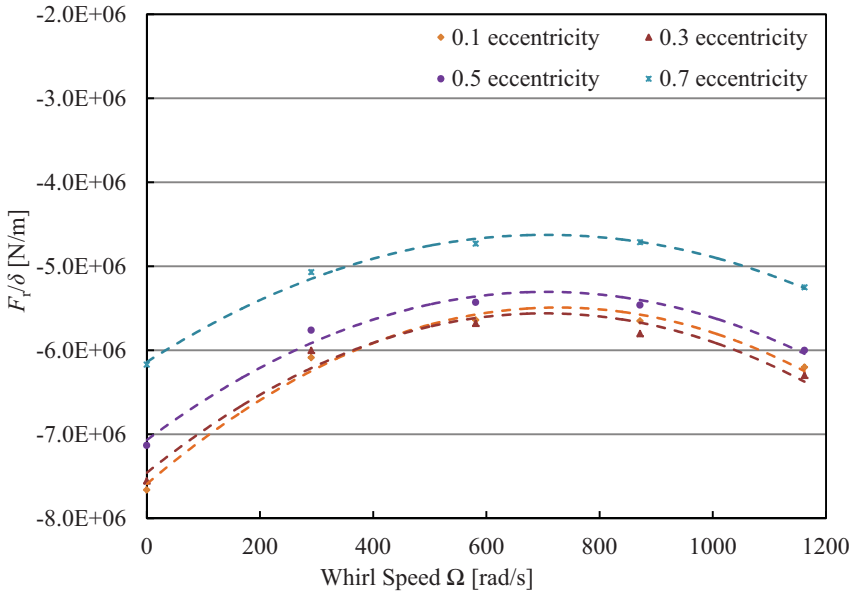

Figure 4-11 Predicted radial seal force *vs*. whirl speed at different eccentricities (tooth-on-stator, 73.6% pre-swirl rate)

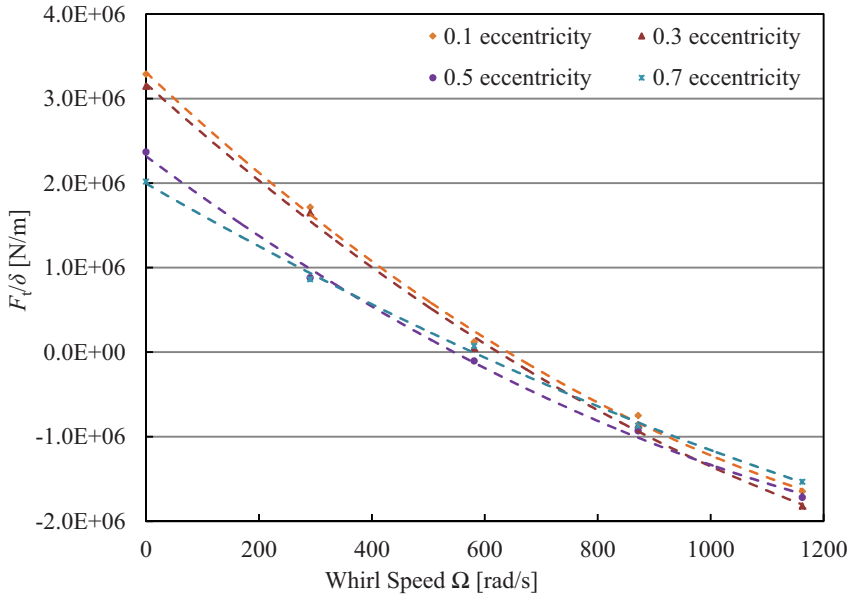

Figure 4-12 Predicted tangential seal force *vs*. whirl speed at different eccentricities (tooth-on-stator, 73.6% pre-swirl rate)

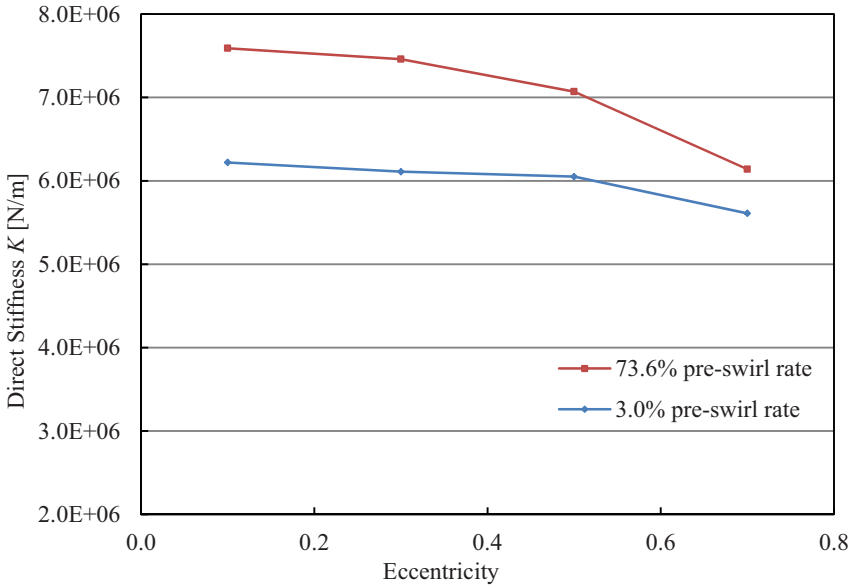

Figure 4-13 Predicted direct stiffness vs. eccentricity (tooth-on-stator)

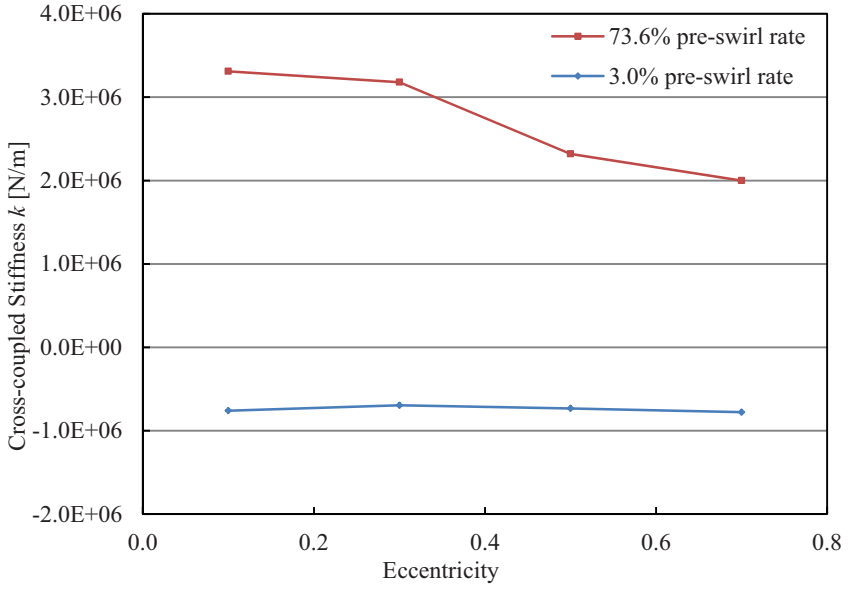

Figure 4-14 Predicted cross-coupled stiffness *vs*. eccentricity (tooth-on-stator)

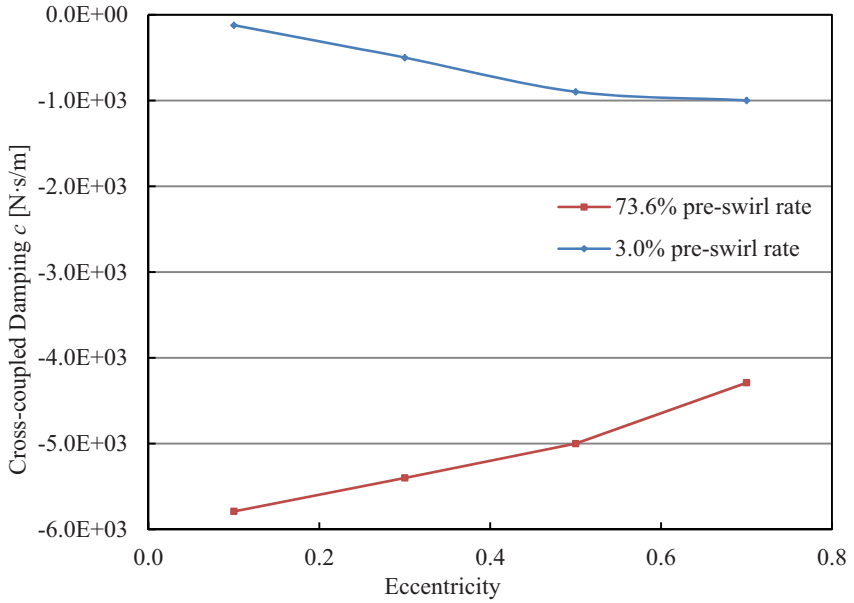

Figure 4-15 Predicted cross-coupled damping *vs*. eccentricity (tooth-on-stator)

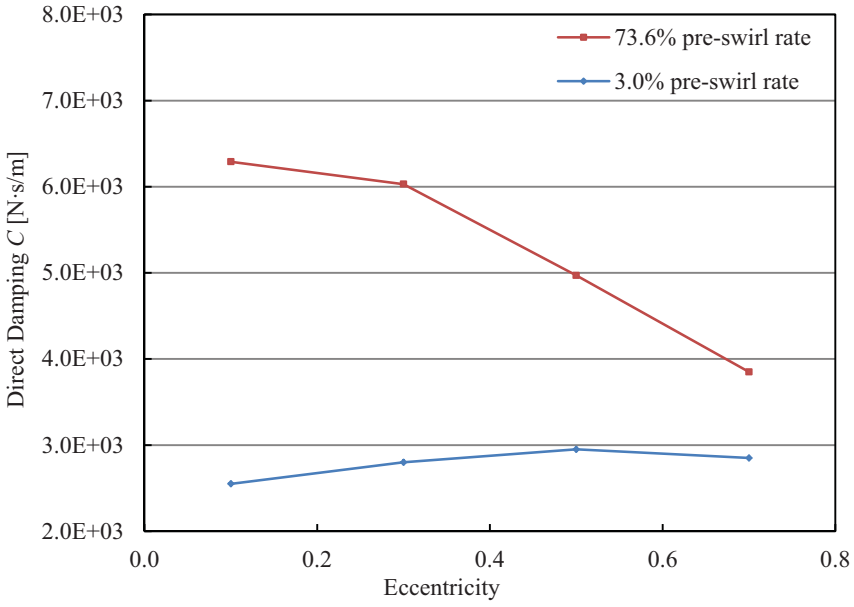

Figure 4-16 Predicted direct damping *vs*. eccentricity (tooth-on-stator)

4.4.3 Clearance

To study the influence of clearance on rotordynamic properties of the labyrinth seal, a set of models based on the dimensions shown in Figure 1-4 with different clearances were modeled and solved. The diameter of rotor was adjusted to generate clearances ranging from 146μm to 438μm. Results of forces at different whirl speed were analyzed with the second-order model.

Figure 4-17 and Figure 4-18 show the radial and tangential forces on rotor *vs*. whirl speed for different clearances in the low pre-swirl condition. Figure 4-19 and Figure 4-20 show the forces on rotor *vs*. whirl speeds for different clearances in a high pre-swirl condition. In this case, both the tangential forces on the rotor are affected by eccentricity.

Data points in Figure 4-17 to Figure 4-20 were approximated with the second-order model and the results are compared in Figure 4-21 to Figure 4-24. Figure 4-21 shows that the increase of clearance leads to increase of direct stiffness for both low and high pre-swirl cases. It is shown in Figure 4-22 that the cross-coupled stiffness increases with clearance in low pre-swirl condition but decrease in high pre-swirl condition. It indicates that bigger clearance help to make the rotor more stable when the pre-swirl is high.

Figure 4-23 and Figure 4-24show that in the low pre-swirl condition the cross-coupled damping increases with clearance; while the direct damping decreases with clearance, which indicates bigger clearance make the rotor more unstable. Unfortunately, no clear relationship between damping and clearance were shown in the high pre-swirl condition.

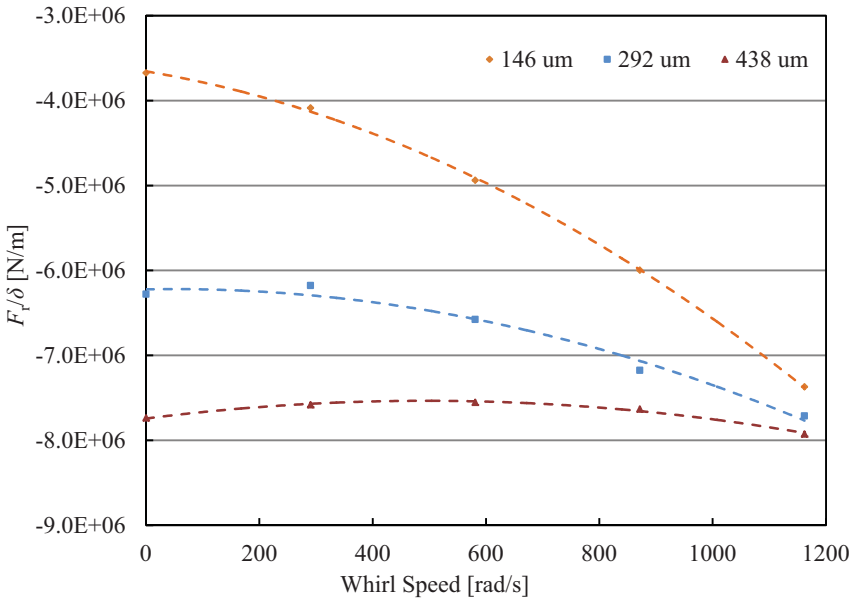

Figure 4-17 Predicted radial seal force *vs*. whirl speed at different clearance (tooth-on-stator, 0.1 eccentricity, 9.7% pre-swirl rate)

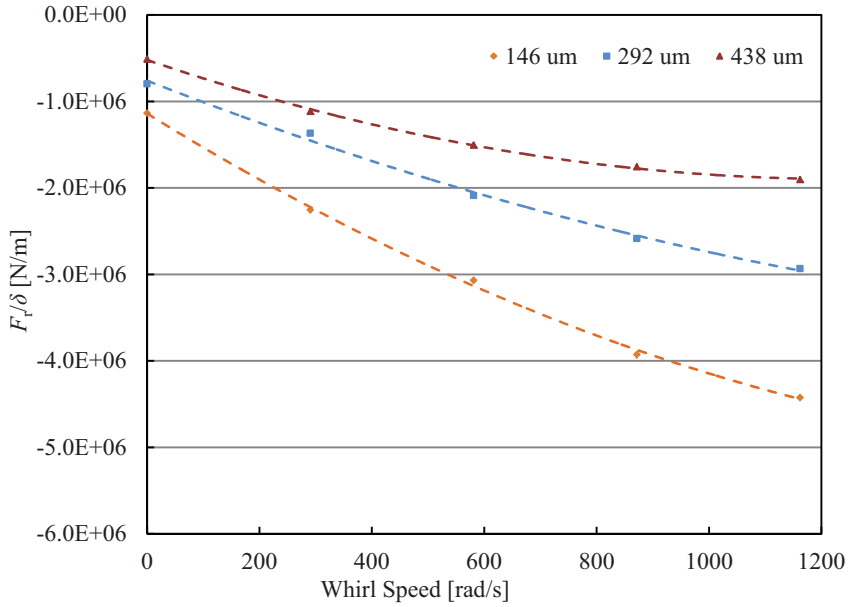

Figure 4-18 Predicted tangential seal force *vs*. whirl speed at different clearance (tooth-on-stator, 0.1 eccentricity, 9.7% pre-swirl rate)

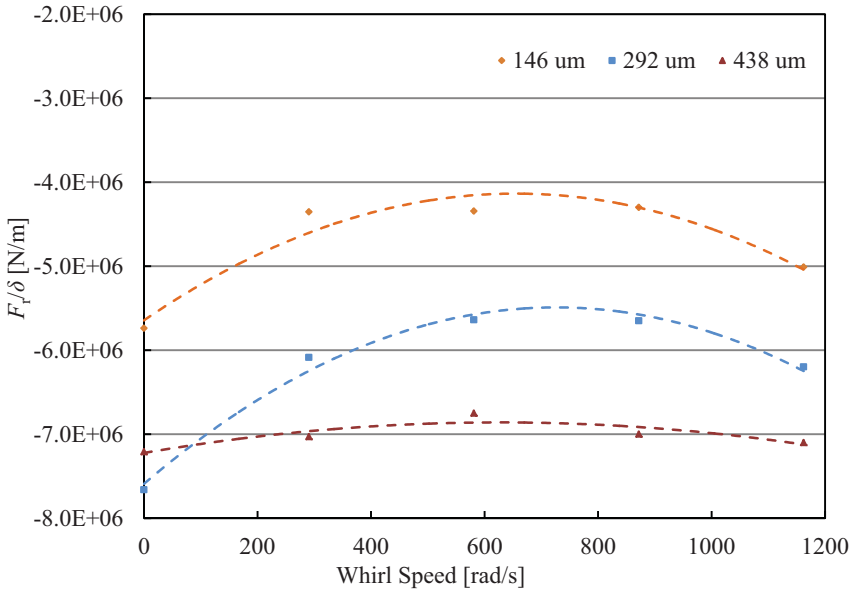

Figure 4-19 Predicted radial seal force *vs*. whirl speed at different clearance (tooth-on-stator, 0.1 eccentricity, 73.6% pre-swirl rate)

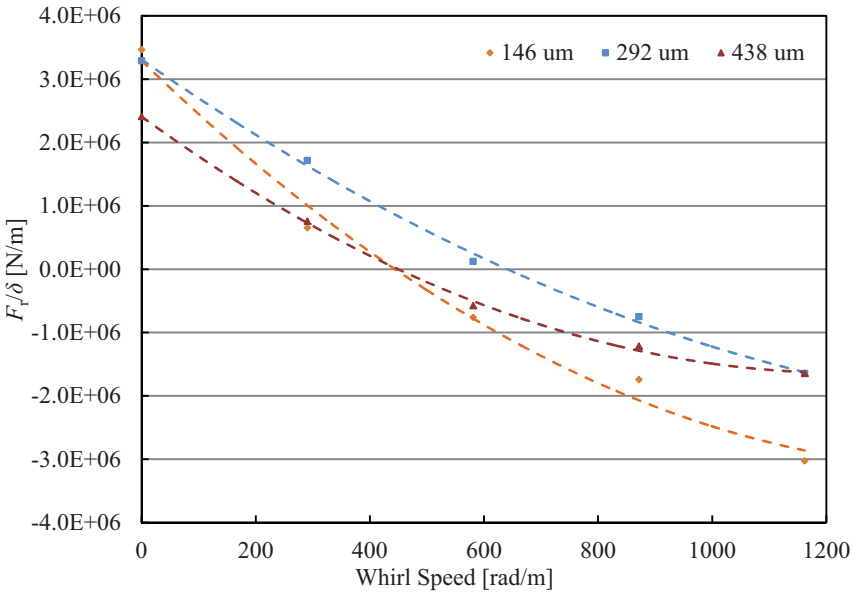

Figure 4-20 Predicted tangential seal force *vs*. whirl speed at different clearance (tooth-on-stator, 0.1 eccentricity, 73.6% pre-swirl rate)

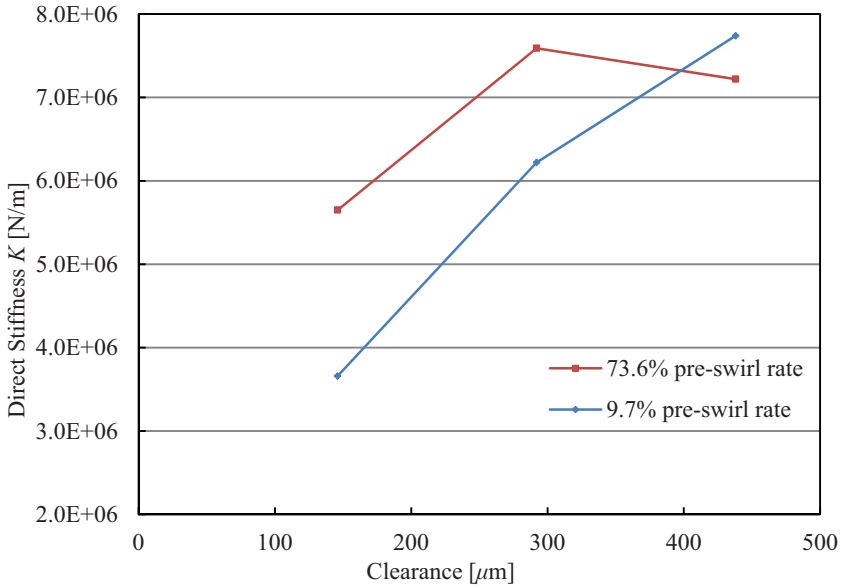

Figure 4-21 Predicted direct stiffness *vs*. clearance (tooth-on-stator, 0.1 eccentricity)

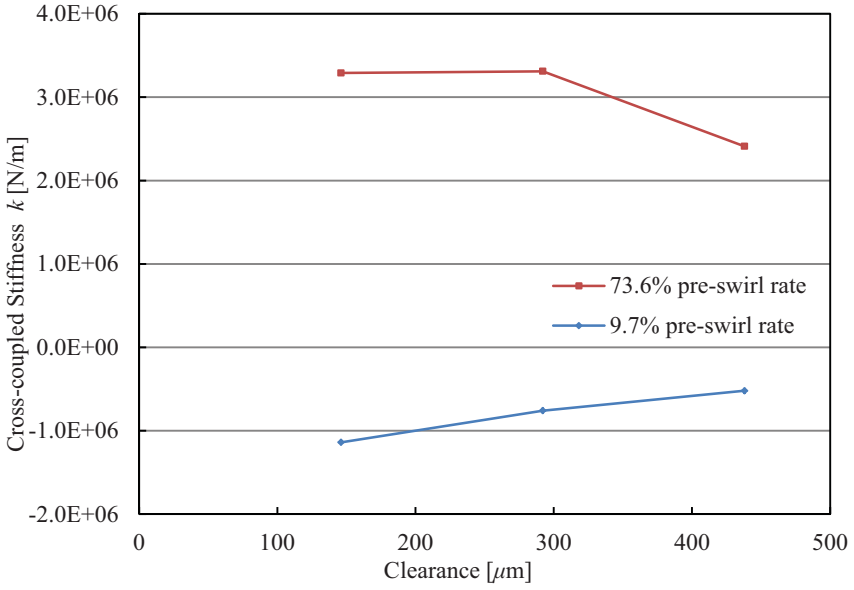

Figure 4-22 Predicted cross-coupled stiffness *vs*. clearance (tooth-on-stator, 0.1 eccentricity)

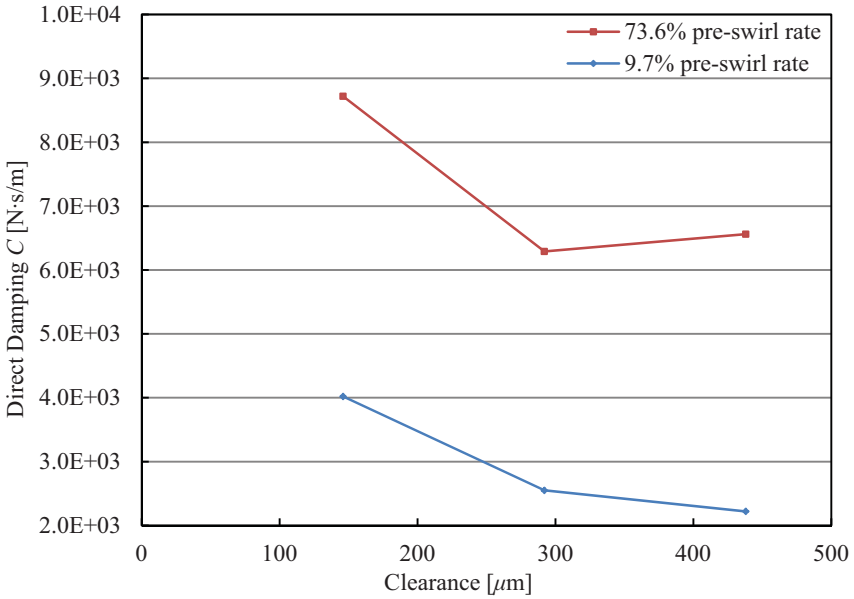

Figure 4-23 Predicted direct damping *vs*. clearance (tooth-on-stator, 0.1 eccentricity)

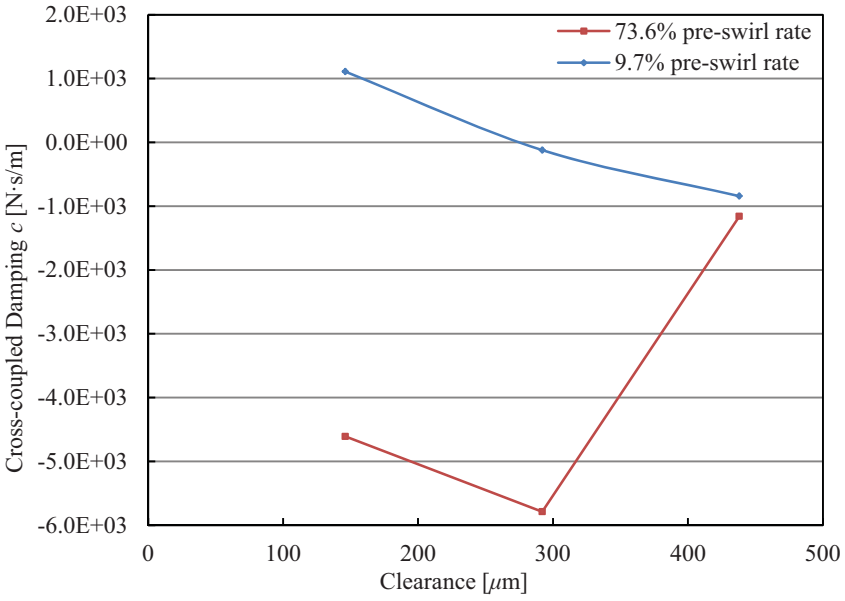

Figure 4-24 Predicted cross-coupled damping *vs*. clearance (tooth-on-stator, 0.1 eccentricity)

4.5 Tooth-on-Rotor Straight Eye Seal

In order to compare rotordynamic characteristics of the tooth-on-stator and tooth-on-rotor labyrinth seal, a model with teeth on rotor was built based on the dimensions shown in Figure 1 2 with eccentricity of 0.1. Results of forces at different whirl speed were analyzed with the second-order model and compared with the tooth-on-stator cases.

Radial and tangential forces on rotor *vs*. whirl speed for different pre-swirl rates were plotted in Figure 4-25 and Figure 4-26 and approximated with the second-order model. Rotordynamic coefficients for the tooth-on-rotor and tooth-on-stator are compared in Figure 4-27 to Figure 4-28.

Figure 4-27 compares the direct and cross-coupled stiffness of tooth-on-stator and tooth-on-rotor models. It is shown that the tooth-on-rotor labyrinth seal has bigger direct and cross-coupled stiffness than the tooth-on-stator seal. Moreover, the direct and cross-coupled stiffness are proportional to the pre-swirl rate for both tooth-on-rotor and tooth-on-stator configurations.

Figure 4-28 shows that the direct damping increases with pre-swirl for both tooth-on-rotor and tooth-on-stator configurations. Furthermore the tooth-on-rotor seals increases faster, which indicates that the tooth-on-rotor labyrinth seal may have a better stability when there is a high pre-swirl. In Figure 4-28, it is also shown that cross-coupled damping decrease with pre-swirl for both configurations.

It is of interest that the tooth-on-rotor configuration leads to bigger cross-coupled stiffness and direct damping. They work on the stability of the rotor in opposite ways: bigger cross-coupled stiffness is an unstable factor for the rotor while the bigger direct damping is the stable the rotor is. In this case, the Q-Factor is required to calculate. As shown in Figure 4-29, the Q-Factor for the tooth-on-rotor model increased from negative to positive with the pre-swirl in a similar pattern as that of the tooth-on-stator model, which proves that the rotor stability is decreased by the pre-swirl in the seal. Moreover the Q-Factor of the tooth-on-rotor model is slightly smaller than that of the tooth-on-stator model, which means that the tooth-on-rotor configuration could be more stable.

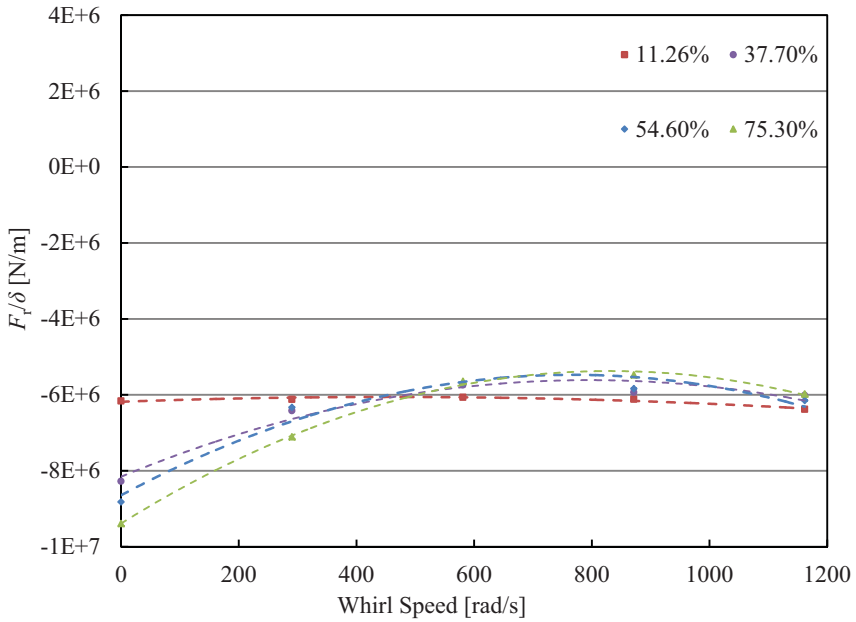

Figure 4-25 Predicted radial seal force *vs*. whirl speed at different pre-swirl rates (tooth-on-rotor, 0.1 eccentricity)

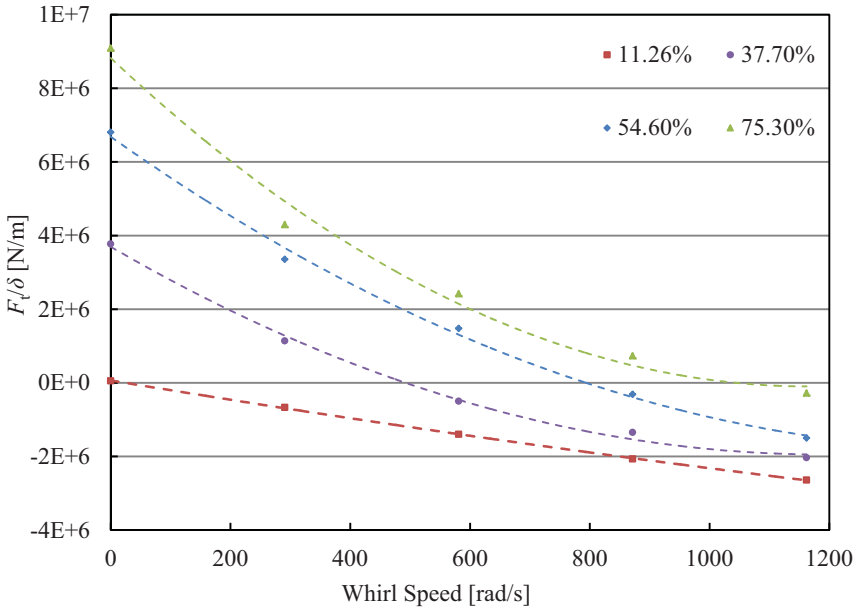

Figure 4-26 Predicted tangential seal force *vs*. whirl speed at different pre-swirl rates (tooth-on-rotor, 0.1 eccentricity)

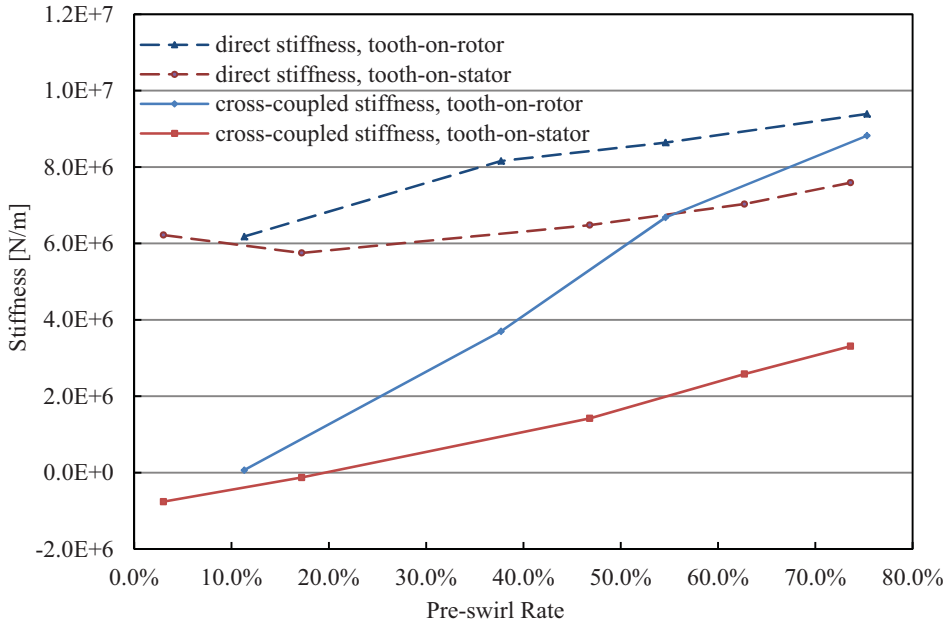

Figure 4-27 Predicted stiffness *vs*. pre-swirl rate (0.1 eccentricity)

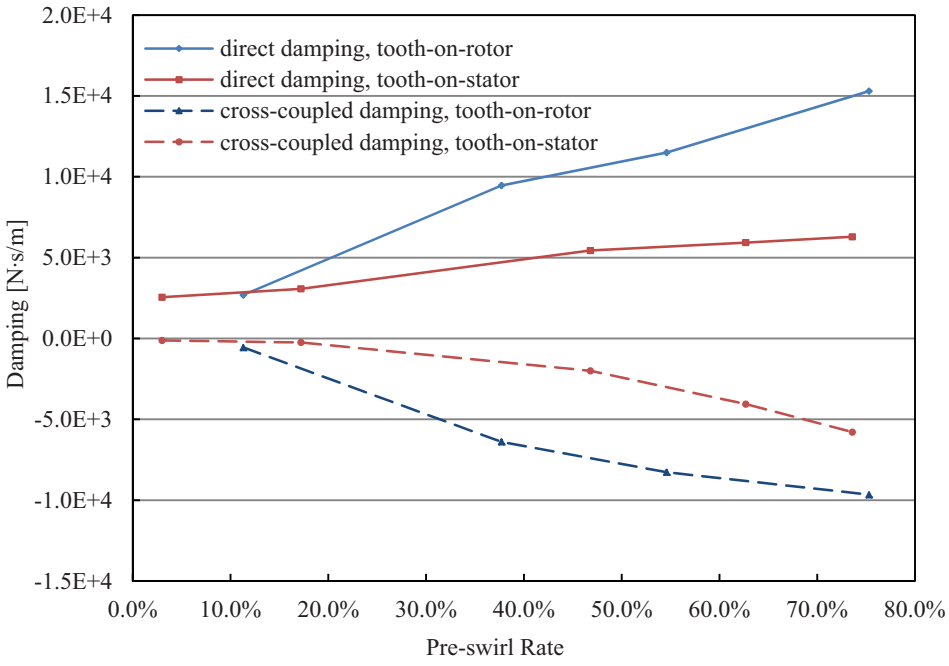

Figure 4-28 Predicted damping *vs*. pre-swirl rate (0.1 eccentricity)

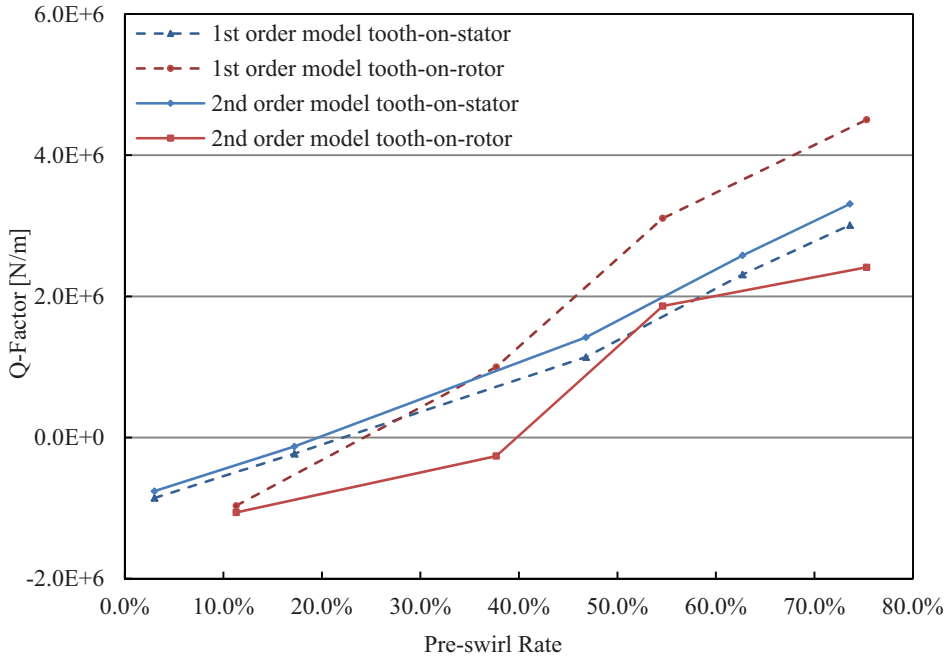

Figure 4-29 Q-Factor *vs*. pre-swirl rate (0.1 eccentricity)

4.6 Stepped Eye Seal

The stepped eye seal experimentally studied by Kwanka [17] was modeled for the calculation. It is noticeable that the pre-swirl rate is as high as 2000% in the experiment due to the low rotating speed. The predictions on direct and cross-coupled stiffness have been compared with the test data in 2.6.2 and thus some more details given by the CFX simulation will be shown and discussed in this section.

Radial and tangential forces on rotor vs. whirl speed for different pre-swirl rates were plotted in Figure 4-30 and Figure 4-31. Rotordynamic coefficients calculated with the second-order model for varying pre-swirl rates are shown in Figure 4-32 and Figure 4-33.

Figure 4-32 shows that both direct and cross-coupled stiffness are increased with the increasing pre-swirl rate. Note that the direct stiffness seems to be decreased in Figure 4-32, but the value is actually increased. Figure 4-33 shows that both the direct and cross-coupled damping is increased with the increasing pre-swirl rate. The increase of cross-coupled stiffness is an unstable factor for the rotor while the increase of direct damping helps to keep the rotor stable.

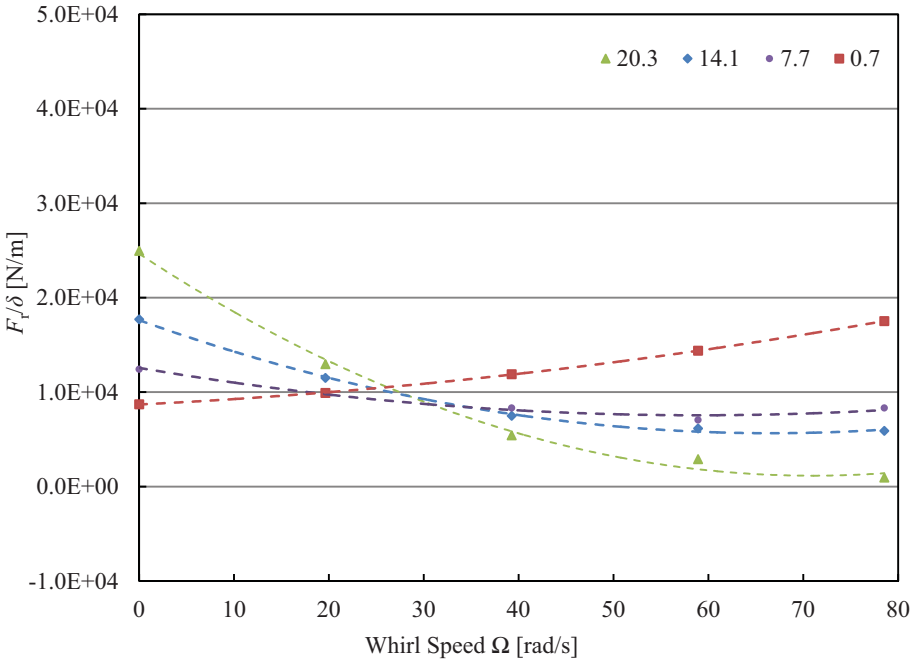

Figure 4-30 Predicted direct stiffness *vs*. pre-swirl rate (stepped eye seal, 0.1 eccentricity)

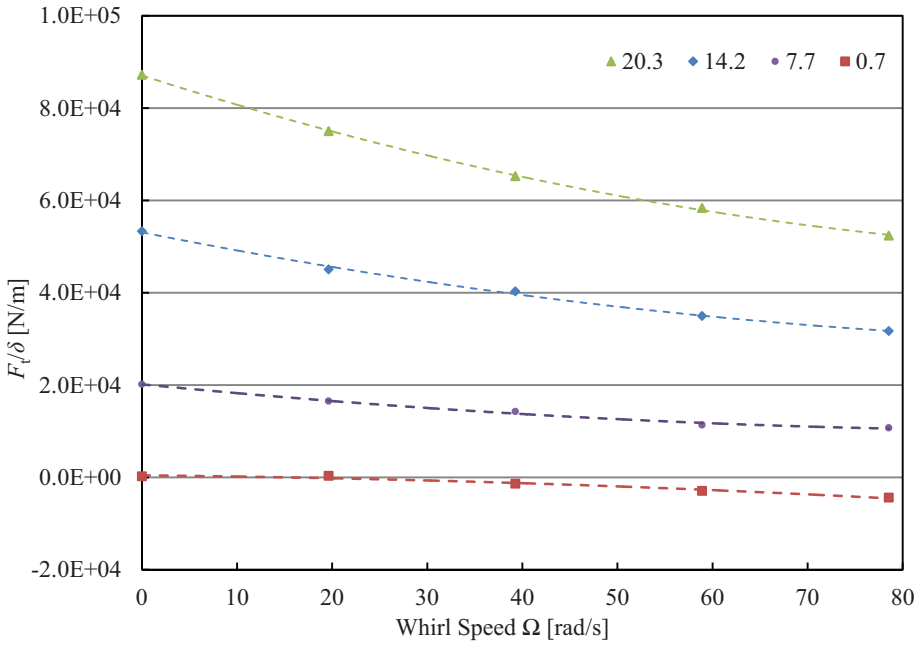

Figure 4-31 Predicted cross-coupled stiffness *vs*. pre-swirl rate (stepped eye seal, 0.1 eccentricity)

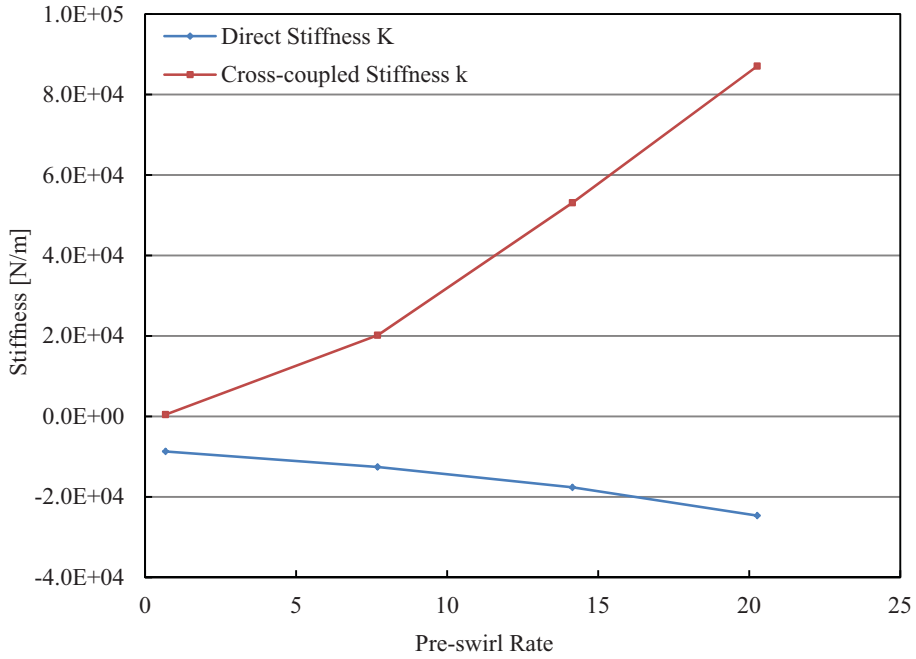

Figure 4-32 Predicted stiffness *vs*. pre-swirl rate (stepped eye seal, 0.1 eccentricity)

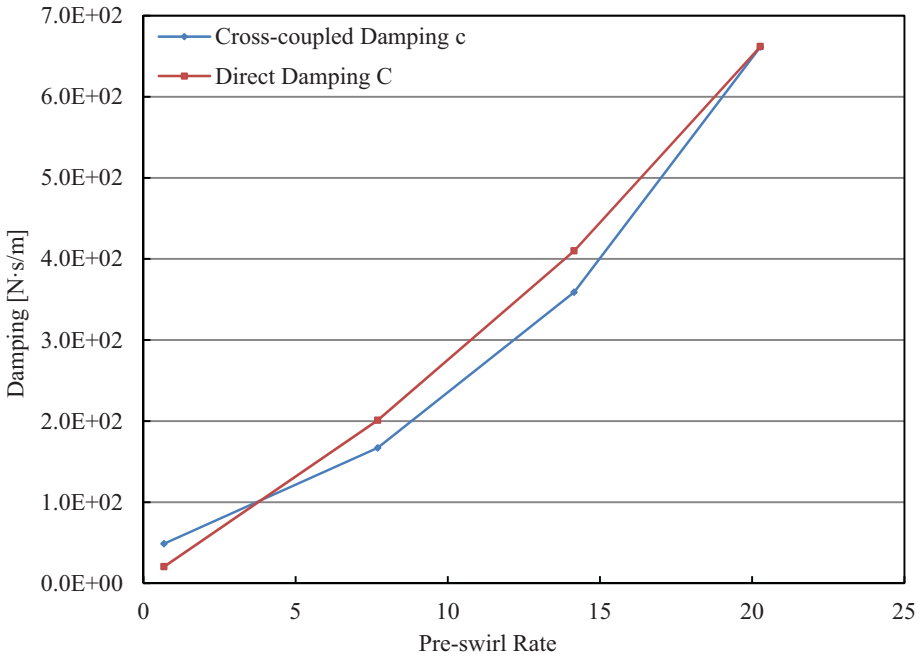

Figure 4-33 Predicted damping *vs*. pre-swirl rate (stepped eye seal, 0.1 eccentricity)

4.7 Balance Drum Seal

Of all the seals used in a turbo machine, the balance drum seal usually has the most significant influence on the dynamic behavior of the rotor because it could usually generate the biggest force on the rotor due to its longest geometry and highest pressure drop. Furthermore, it is usually installed closed to the bearing, which is another destabilizing factor for the rotor. So it is of interest to study the rotordynamic properties of the balance drum seal considering high pre-swirl rates.

Figure 4-34 and Figure 4-35 plot the radial and tangential forces on the rotor vs. whirl speeds for different pre-swirl rates. Rotordynamic coefficients *vs.* pre-swirl rates are shown in Figure 4-36 and Figure 4-37.

It is shown in Figure 4-36 and Figure 4-37 that both direct and cross-coupled stiffness are increased with the increasing pre-swirl rate. Again the direct stiffness seems to be decreased in Figure 4-36 but the amplitude is actually increased. Figure 4-37 shows that both the direct and cross-coupled damping is increased with the increasing pre-swirl rate.

As discussed above, the increase of cross-coupled stiffness and direct damping works oppositely on the stability of the rotor. So it is necessary to calculate the Q-Factor to predict the stability property of the seal. Figure 4-38 shows that the Q-Factor is increased from negative to positive with the pre-swirl, which indicates that the rotor stability is decreased by the high pre-swirl in the balance drum seal. So we can predict that the balance drum seal would drive the rotor unstable at high pre-swirl. To prove that prediction, a rotor stability analysis will be conducted in the next chapter with rotordynamic coefficient calculated here.

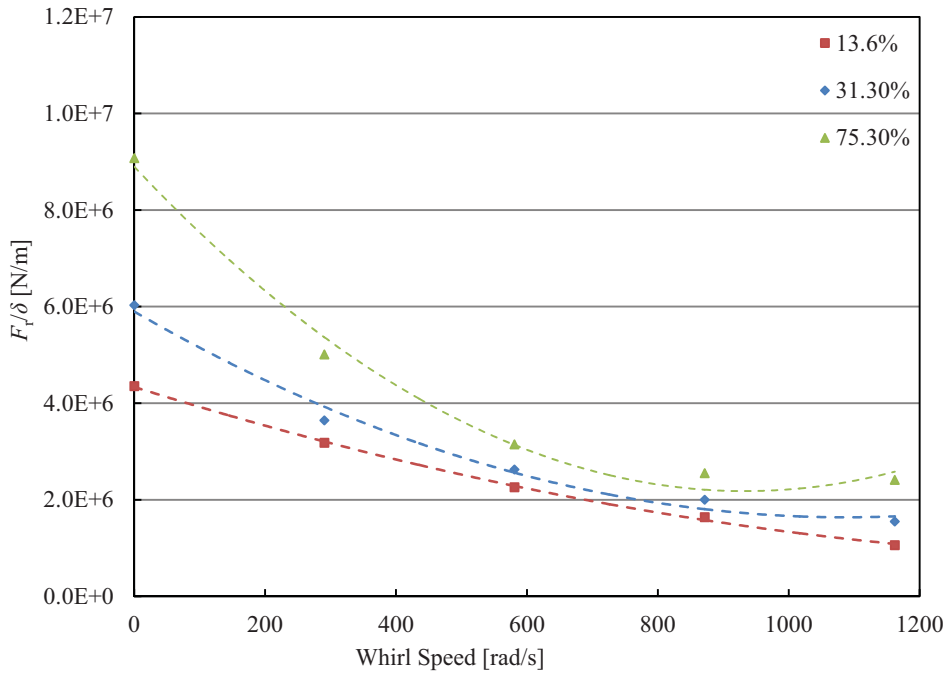

Figure 4-34 Predicted direct stiffness *vs*. pre-swirl rate (balance drum seal 0.1 eccentricity)

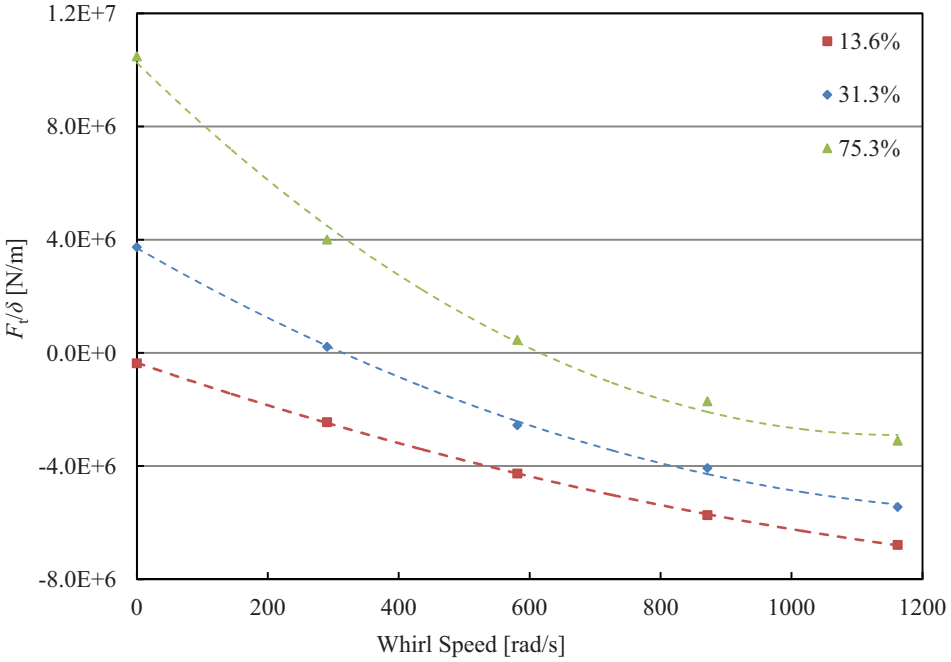

Figure 4-35 Predicted cross-coupled stiffness *vs*. pre-swirl rate (balance drum seal 0.1 eccentricity)

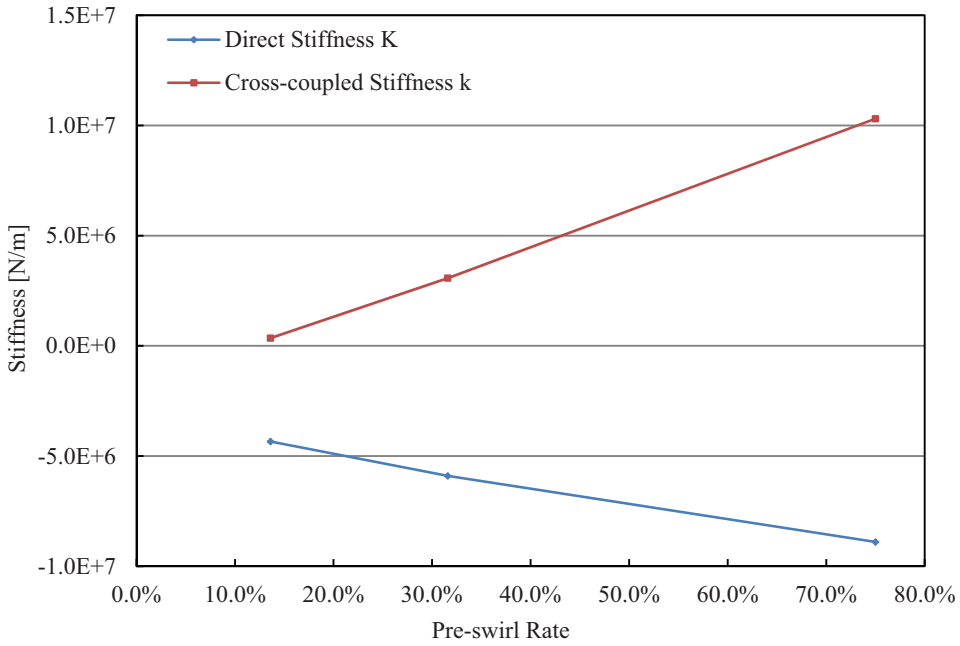

Figure 4-36 Predicted stiffness *vs*. pre-swirl rate (balance drum seal, 0.1 eccentricity)

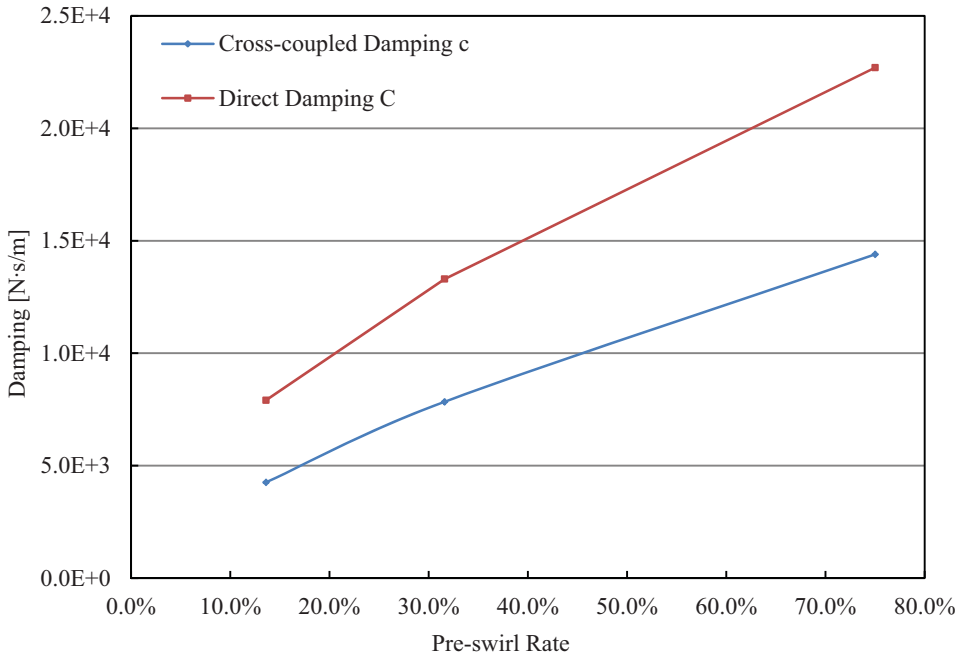

Figure 4-37 Predicted damping *vs*. pre-swirl rate (balance drum seal, 0.1 eccentricity)

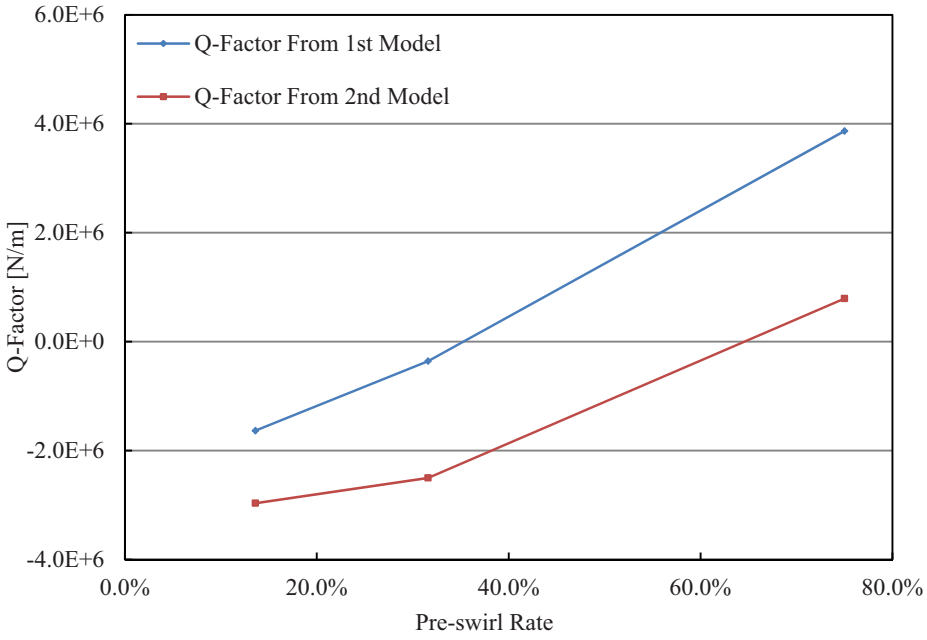

Figure 4-38 Q-Factor *vs*. pre-swirl rate (balance drum seal, 0.1 eccentricity)

4.8 Summary

The second-order rotordynamic model was firstly established for seals with high pre-swirl rates and then the rotordynamic characteristics of the three types of labyrinth seals were analyzed. Some relationships between influencing factors and the four rotordynamic coefficients were concluded:

1) Both direct and cross-coupled stiffness are increased with the increasing pre-swirl rate. The direct damping is increased but the cross-coupled damping is decreased with the increasing pre-swirl rate. The increase of cross-coupled stiffness adds an unstable factor to the rotor but the increase of direct damping serves to make the rotor more stable.

2) The increasing eccentricity decreases direct stiffness and cross-coupled stiffness. The cross-coupled damping decreases with eccentricity when the pre-swirl rate is low however it increases significantly with eccentricity in a high pre-swirl condition. The direct damping doesn't show too much change with the increase of eccentricity in low pre-swirl condition however it drops significantly in high pre-swirl condition, which decreases the stability of the rotor.

3) The direct stiffness always increases with clearance, while the cross-coupled stiffness increases at low pre-swirl but decrease with clearance at high pre-swirl. It indicates that bigger clearance help to make the rotor more stable when the pre-swirl is high. In the low pre-swirl condition the cross-coupled damping increases with clearance; while the direct damping decreases with clearance, which indicates that the clearance should not be too big to keep the rotor stable when the pre-swirl rate is low. Unfortunately, no clear relationship between damping and clearance was shown in the high pre-swirl condition.

4) The labyrinth seal with the tooth-on-rotor has bigger cross-coupled stiffness and direct damping than that with tooth-on-stator. Bigger cross-coupled stiffness is an unstable factor for the rotor while bigger direct damping serves to keep the rotor stable. The Q-Factor shows that the tooth-on-rotor configuration could be more stable.

5) For the stepped eye seal, both the direct and cross-coupled stiffness are increased with the pre-swirl, which may lead to rotor instability. On the other hand, the direct damping decreases with the pre-swirl and helps to maintain the rotor stable.

6) The drum balance seal performs similarly as the stepped eye seal: all the four coefficients increase with the increasing pre-swirl. So it would be difficult to directly predict the influence of pre-swirl on the stability. The rotor stability analysis is required.

7) The calculation of Q-Factor for the straight eye seal and the balance drum shows that a high pre-swirl in the labyrinth seal could decrease the rotor stability.

5 Rotor Stability Analysis

5.1 Equation of Motion and Logarithmic Decrement

In a rotordynamic analysis, the equation of motion of a rotor system can usually be written as

$$[M]\{\ddot{q}\}+[C]\{\dot{q}\}+[K]\{q\}=\{F\} \tag{5.1}$$

where [*M*], [*C*], and [*K*] are the system overall mass, damping, and stiffness matrices respectively. {*F*} is the external force vector, which may include the fluid forces from bearings, aerodynamic effects, and seals. To determine the eigenvalues and eigenvectors, the characteristic equation of eq (5.1) can be rewritten as

$$\begin{bmatrix}[I] & 0\\ [C] & [M]\end{bmatrix}\begin{Bmatrix}\dot{q}\\ \ddot{q}\end{Bmatrix}+\begin{bmatrix}0 & [I]\\ [K] & 0\end{bmatrix}\begin{Bmatrix}q\\ \dot{q}\end{Bmatrix}=\begin{Bmatrix}0\\ 0\end{Bmatrix} \tag{5.2}$$

In general, the eigenvalues of eq (5.2) are conjugate complex and can be given as

$$\lambda_i=\sigma_i+j\omega_i,\quad \overline{\lambda_i}=\sigma_i-j\omega_i \tag{5.3}$$

where σ is the system damping exponents and i represents the i^{th} mode. The corresponding conjugate eigenvectors can be noted as $\{\psi_i\}$ and $\{\overline{\psi}_i\}$. The logarithmic decrement of the rotor system is then defined as

$$\delta_i=-2\pi\frac{\sigma_i}{\omega_i} \tag{5.4}$$

The logarithmic decrement is used to determine the system stability: a negative logarithmic decrement indicates system instability.

According to [48], for the rotor system including fluid bearings, aerodynamic effects, and seals, δ_i can be given as

$$\delta_i = \frac{\pi \omega_i c_i^* + \Delta k_i}{\omega^2 m_i^* + \omega_i \Delta c_i / 2} \tag{5.5}$$

where m_i^*, c_i^*, Δk_i, and Δc_i are defined as

$$\begin{aligned}
m_i^* &= \left\{\overline{\psi}_i\right\}^T \left[M^*\right] \left\{\psi_i\right\} = \left\{\psi_i\right\}^T \left[M^*\right] \left\{\overline{\psi}_i\right\} \\
c_i^* &= \left\{\overline{\psi}_i\right\}^T \left[C^*\right] \left\{\psi_i\right\} = \left\{\psi_i\right\}^T \left[C^*\right] \left\{\overline{\psi}_i\right\} \\
k_i^* &= \left\{\overline{\psi}_i\right\}^T \left[K^*\right] \left\{\psi_i\right\} = \left\{\psi_i\right\}^T \left[K^*\right] \left\{\overline{\psi}_i\right\} \\
\Delta m_i &= \left\{\overline{\psi}_i\right\}^T \left[\Delta M\right] \left\{\psi_i\right\} = -\left\{\psi_i\right\}^T \left[\Delta M\right] \left\{\overline{\psi}_i\right\} \\
\Delta c_i &= \left\{\overline{\psi}_i\right\}^T \left[\Delta C\right] \left\{\psi_i\right\} = -\left\{\psi_i\right\}^T \left[\Delta C\right] \left\{\overline{\psi}_i\right\} \\
\Delta k_i &= \left\{\overline{\psi}_i\right\}^T \left[\Delta K\right] \left\{\psi_i\right\} = -\left\{\psi_i\right\}^T \left[\Delta K\right] \left\{\overline{\psi}_i\right\}
\end{aligned} \tag{5.6}$$

where M^*, C^*, and K^* are the symmetric parts of overall mass, damping, and stiffness matrices; while ΔM, ΔC, and ΔK are the asymmetric parts. For a symmetric rotor, Δk_i only consists components from bearing, aerodynamic force, and seal thus can be expressed as

$$\begin{aligned}
\Delta k_i &= \sum_{j=1}^{n_B} \left(\left\{\overline{\psi}_{Bi}\right\}_j^T \left[\Delta K_B\right]_j \left\{\psi_{Bi}\right\}_j \right) + \sum_{j=1}^{n_A} \left(\left\{\overline{\psi}_{Ai}\right\}_j^T \left[\Delta K_A\right]_j \left\{\psi_{Ai}\right\}_j \right) + \sum_{j=1}^{n_S} \left(\left\{\overline{\psi}_{Si}\right\}_j^T \left[\Delta K_S\right]_j \left\{\psi_{Si}\right\}_j \right) \\
&= \sum_{j=1}^{n_B} \left(\Delta k_{Bi}\right)_j + \sum_{j=1}^{n_A} \left(\Delta k_{Ai}\right)_j + \sum_{j=1}^{n_S} \left(\Delta k_{Si}\right)_j
\end{aligned} \tag{5.7}$$

where subscriptions of B, A, and S represents bearing, aerodynamic force and seal. n_B, n_A, and n_S are total numbers of bearings, aerodynamic forces, and seals. Eq (5.5) and (5.7) clearly show the influences of bearing, aerodynamic force, and seal on the stability of the rotor.

In order to study the potential effects from the balance drum seal on a typical compressor in the practical working condition, a typical tilting pad bearing and aerodynamic force was employed while the seal rotordynamic coefficients are obtained from previous calculation.

In this study, the rotor stability was conducted in DyRoBeS_Rotor [49].

5.2 The Rotor-Bearing-Seal System

5.2.1 The Compressor Rotor

A typical centrifugal compressor rotor was employed for the stability analysis. The finite element model was built in DyRoBeS_Rotor including the rotor, the bearings, the aerodynamic force, and the balance drum seal.

As shown in Figure 5-1, the rotor has five stages, a coupling disk and a collar for the thrust bearing. The spring shown on station 2 and 10 are tilting pad bearings, the spring on section 6 represents the aerodynamic force and the spring shown on station 10 corresponds to the balance drum seal. The rotordynamic coefficients of these three types of springs will be further discussed from section 5.2.2 to section 5.2.4.

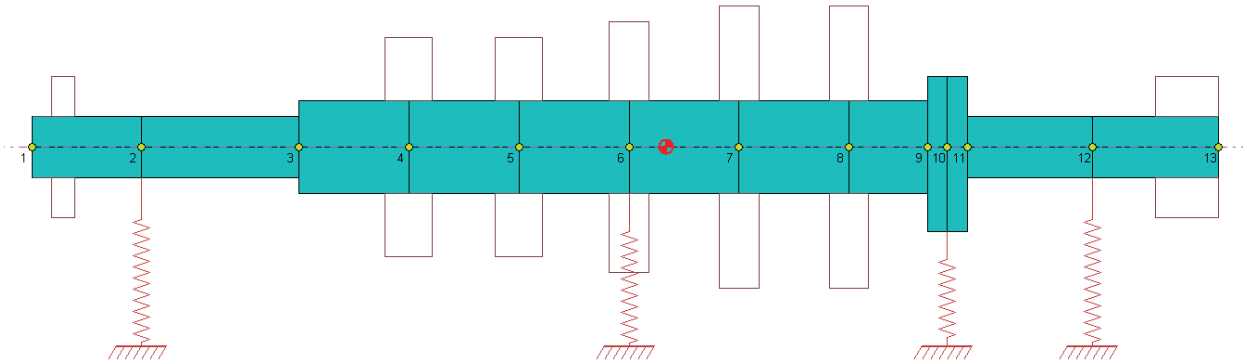

Figure 5-1 Finite element model of the rotor-bearing-seal system

5.2.2 The Tilting Pad Bearing

A 5-pad tiling pad bearing was employed in this study. The parameters of a bearing could have significant influence on the bearing dynamic properties so the parameters were carefully selected to guarantee the bearing is general enough for the calculated compressor rotor. The speed dependent rotordynamic coefficients were calculated with DyRoBeS_BePerf and imported into DyRoBeS_Rotor for the stability analysis. Input parameters for the calculation are shown in Figure 5-2. The British unit was used for convenient input in the software.

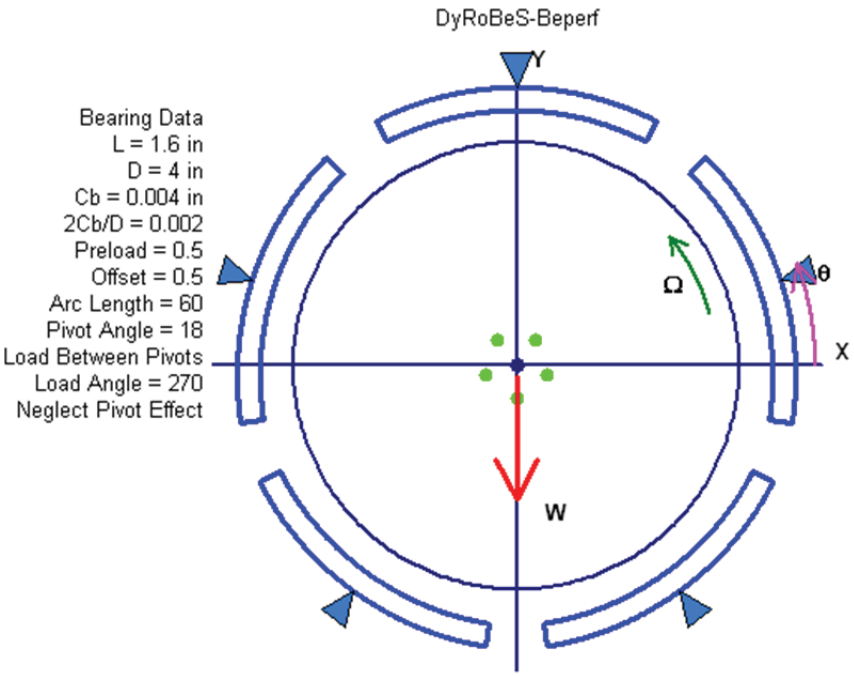

Figure 5-2 The tilting pad bearing

5.2.3 The Aerodynamic Force

The aerodynamic cross-coupling force caused by the impeller clearance variation was also included and lumped at station 6, which is close to the center of the rotor. The aerodynamic forces were modeled as springs and typical rotordynamic coefficients for the 5-stage radial compressor were employed, as shown in Table 5-1.

Table 5-1 Rotordynamic coefficients input for the aerodynamic force

Coefficients	Input
K_{xx}, K_{yy} (lb_f/in)	0
K_{xy}, K_{yx} (lb_f/in)	$\pm 9\times10^3$
C_{xx}, C_{yy} (lb_f·s /in)	0
C_{xy}, C_{yx} (lb_f·s/in)	0

5.2.4 The Balance Drum Seal

The balance drum seal usually has the most significant influence on the stability among all seals on a rotor. One of the reasons is that the balance drum seal usually has the biggest cross-coupled stiffness as it has bigger tooth number and longer geometry to generate bigger pressure drop. The other reason is that the balance drum is usually placed close to the bearing and their effects may be coupled.

The rotordynamic coefficients for the balance drum seal has been obtained from previous numerical simulation including cases with 0 and 75% pre-swirl rates. The input data has been transferred from SI unit to British unit for convenient input in the software.

Table 5-2 Rotordynamic coefficients input for the balance drum seal

Coefficients	13.6% Pre-swirl Rate	75.0% Pre-swirl Rate
K_{xx}, K_{yy} (lb_f/in)	-2.48×10^{4}	-5.08×10^{4}
K_{xy}, K_{yx} (lb_f/in)	$\pm1.99\times10^{3}$	$\pm5.88\times10^{4}$
C_{xx}, C_{yy} (lb_f·s/in)	4.52×10^{1}	1.32×10^{2}
C_{xy}, C_{yx} (lb_f·s/in)	$\pm2.43\times10^{1}$	$\pm8.22\times10^{1}$

Note: the cross-coupled terms have opposite signs.

5.3 Stability Analysis

Figure 5-3 and Figure 5-4 separately present the stability maps for the rotor with a low and high pre-swirl balance drum seal. It is shown that for the low pre-swirl case only one mode may become unstable at high rotating speed while that mode becomes always unstable when high pre-swirl rate is applied on the balance drum seal.

Figure 5-5 shows the three-dimensional mode shape of the unstable mode. It is the first-order model with forward precession. This is also a bending mode. This result totally agrees with conclusion given by Chen and Gunter [50] that in most applications, if the system becomes

unstable, the rotor whirls in its first mode with a forward precession. The first unstable mode could be either a rigid body mode or a bending mode, depending on the potential energy distribution.

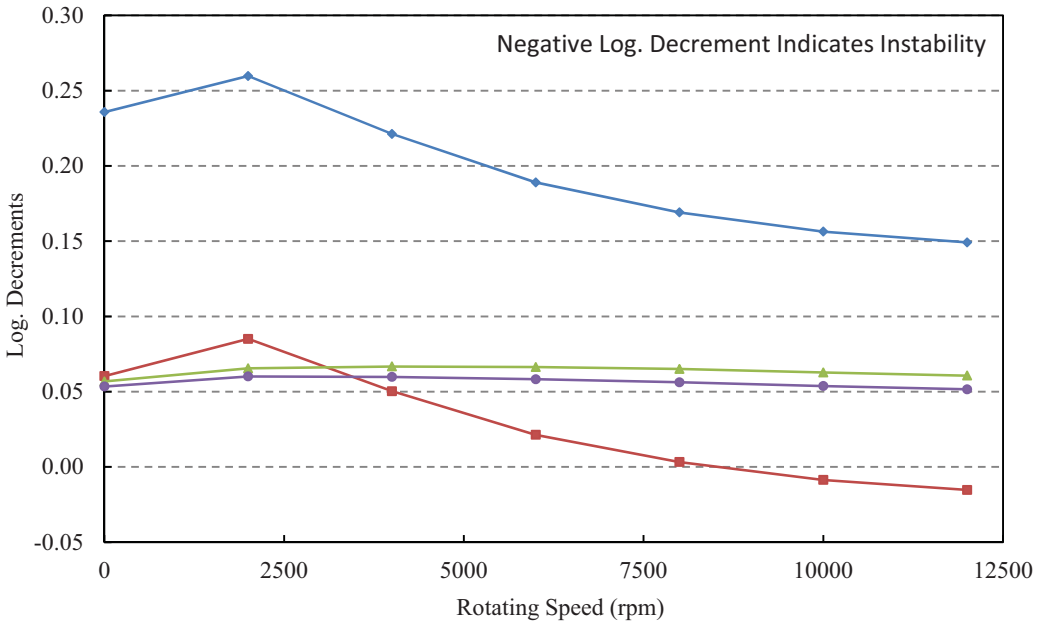

Figure 5-3 Stability map of the rotor system with 13.6% pre-swirl balance drum seal

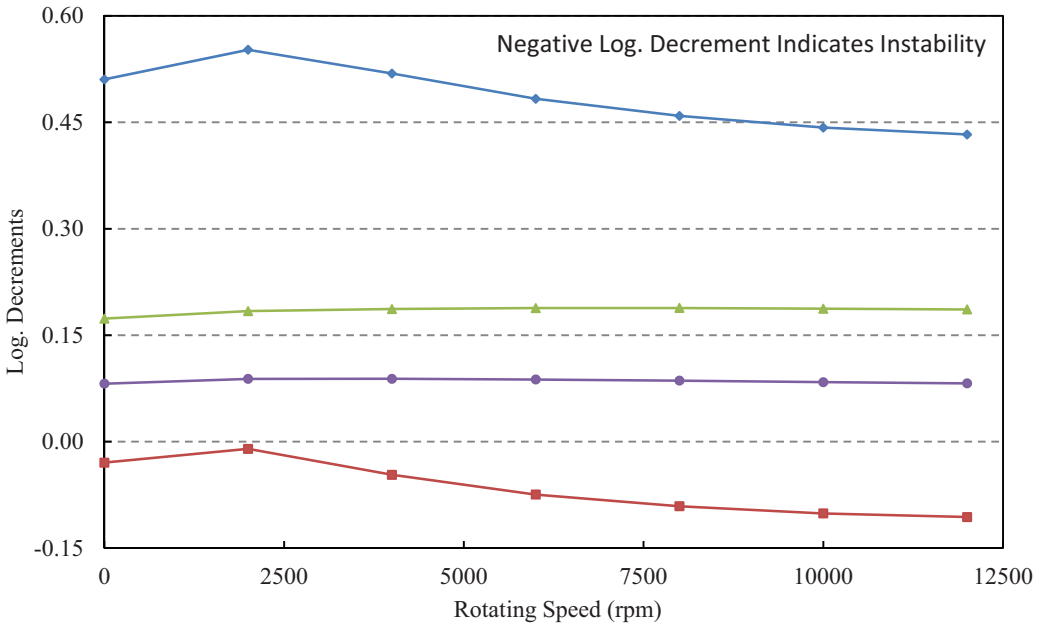

Figure 5-4 Stability map of the rotor system with 75.0% pre-swirl balance drum seal

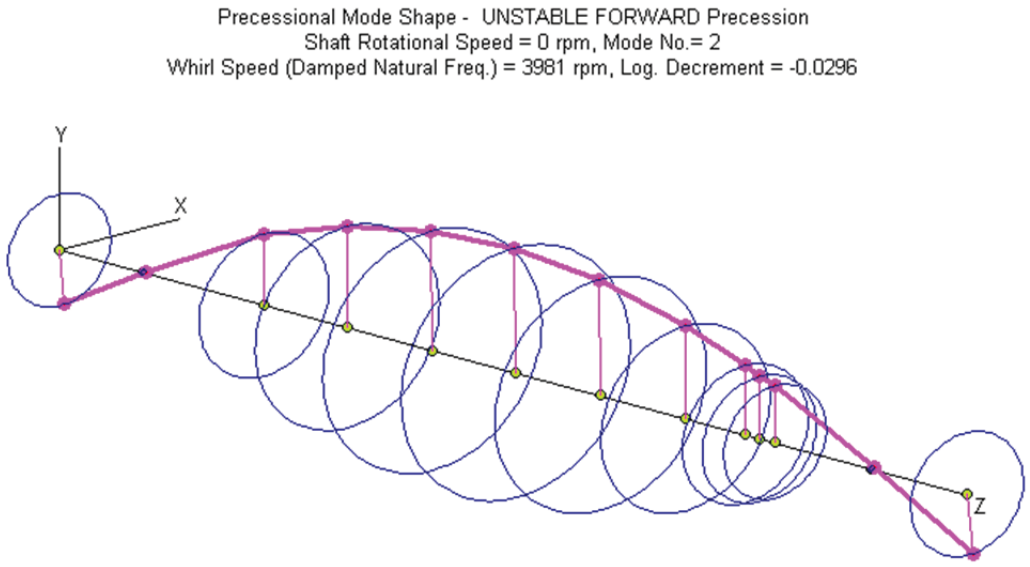

Figure 5-5 Unstable mode (1st mode, forward precession)

5.4 Summary

The theory on the rotor stability analysis was firstly introduced. Then a typical centrifugal compressor was modeled as a finite element model in the DyRoBeS. Proper bearing and aerodynamic forces were chosen for the calculation.

The rotor stability analysis was finally conducted and rotor instability happened when the high pre-swirl was applied on the balance drum seal. The result confirms that the pre-swirl does have significant influence on the rotordynamic coefficients of the labyrinth seal and thus affects the rotor's dynamic behavior even may lead to instability.

6 Conclusions

6.1 Summary of Results

In this dissertation three-dimensional numerical solutions were conducted with the commercial CFD software, ANSYS-CFX, to investigate the influences of pre-swirl rate, eccentricity, clearance, and tooth location on rotordynamic coefficients of labyrinth seals. Three types of labyrinth seals were modeled and a systematical numerical process was developed and verified.

The fluid field was studied first. The pressure distributions and leakages were compared with bulk-flow results and showed good agreements. An extra small vortex was detected at the downstream edge of each tooth, which may be related to the tooth profile thus it may be helpful for seal design in the future. It was found that the pre-swirl has a very slight influence on the leakage for all the three types of seal.

Radial and tangential forces on the rotor were extracted from the fluid field results. It is shown that the traditional first-order rotordynamic model works well for low pre-swirl cases but does not accurately reflect the characteristics when the pre-swirl rate becomes as high as that for a compressor eye seal or balance drum seal (70%). Thus a second-order model including inertia terms was proposed and applied to the rotordynamic analysis in this research.

The rotordynamic analysis on the three labyrinth seals confirmed that the pre-swirl has a significant influence on the rotordynamic coefficients. For all the three seals, both the direct and cross-coupled stiffness are increased with the pre-swirl rate and the bigger cross-coupled stiffness is a main parameter to cause the rotor system to become unstable; the direct damping is also increased with pre-swirl which serves to keep the rotor stable. So Q-Factors were calculated for some cases and the increasing Q-Factors showed that the overall influence of the pre-swirl is to increase the rotor instability.

Besides the pre-swirl, the eccentricity and clearance also have effects on the rotordynamic coefficients of the seal. Moreover the high pre-swirl could enhance their influences.

The stability analysis result confirms that the rotor system may become unstable if equipped labyrinth seals with high pre-swirl rate (about 70%). In another word, the pre-swirl has a big influence on the rotordynamic properties. The de-swirling equipment is suggested to apply in compressors.

6.2 Future Work

Since the existence of the small vortex at the downstream edge of each tooth has never been reported before, more work is required to prove the existence of it. Furthermore, the physical mechanism of the small vortex is still not clear and worth more investigation to find out the reason causing it.

Damper seals such as honeycomb seals are more and more popular for use in modern turbo machines so it is of interest to study the rotordynamic characteristics of damper seals considering high pre-swirl.

The second-order model has been built but it needs to be further validated via experiments. A bulk-flow approach considering inertia effects should be employed to predict the rotordynamic coefficients of current models to compare with the three-dimensional numerical method.

References

[1] Bloch, H. P., 2006, *A Practical Guide to Compressor Technology*, Wiley.

[2] Kirk, R. G., 1988, "Evaluation of Aerodynamic Instability Mechanisms for Centrifugal Ccompressors .2. Advanced Analysis," *Journal of Vibration Acoustics Stress and Reliability in Design-Transactions of the Asme*, **110**(2), pp. 207-212.

[3] Guinzburg, A., Brennen, C. E., Acosta, A. J., and Caughey, T. K., 1993, "The Effect of Inlet Swirl on the Rotordynamic Shroud Forces in a Centrifugal Pump," *J. Eng. Gas. Turbines Power-Trans. ASME*, **115**(2), pp. 287-293.

[4] Childs, D., 1993, *Turbomachinery Rotordynamics*, Wiley.

[5] Muszynska, A., 2005, *Rotordynamics*, Taylor & Francis.

[6] Li, J., Yan, X., Feng, Z., Jiang, S., Kong, X., and Sun, Q., 2009, "State-of-the Art of Turbomachinery Damper Seals Technology and Their Rotordynamic Characteristics," *Thermal Turbine*, **38**(1), pp. 5-14.

[7] Yan, X., Li, J., Song, L., and Feng, Z., 2009, "Investigations on the Discharge and Total Temperature Increase Characteristics of the Labyring Seals with Honeycomb and Smooth Lands," *Journal of Turbomachinery*, **131**(041009), pp. 1-8.

[8] Li, J., Kong, S., Yan, X., Obi, S., and Feng, Z., 2010, "Numerical Investigations on Leakage Performance of the Rotating Labyringth Honeycomb Seal," *Journal of Engineering for Gas Turbines and Power*, **132**(062501), pp. 1-10.

[9] Gamal, A. J. M. and Vance, J. M., 2008, "Labyrinth Seal Leakage Tests: Tooth Profile, Tooth Thickness, and Eccentricity Effects," *Journal of Engineering for Gas Turbines and Power*, **130**(1), pp. 1-11.

[10] Kim, T. S. and Cha, K. S., 2009, "Comparative Analysis of the Influence of Labyrinth Seal Configuration on Leakage Behavior," *Journal of Mechanical Science and Technology*, **23**, pp. 2830-2838.

[11] Alford, J. S., 1965, "Protecting Turbomachinery from Self-excited Rotor Whirl " *Journal of Engineering for Power*, **87**, pp. 333-344.

[12] Benckert, H. and Wachter, J., 1980, "Flow Induced Spring Coefficients of Labyrinth Seals for Application in Rotor Dynamics," *NASA CP*, **2133**, pp. 189-212.

[13] Rajakumar, C. and Sisto, F., 1990, "Experimental Investigations of Rotor Whirl Excitation Forces Induced by Labyrinth Seal Flow," *Journal of Vibration, Acoustics, Stress, and Reliability in Design*, **112**(4), pp. 263-272.

[14] Childs, D. W. and Scharrer, J. K., 1986, "Experimental Rotordynamic Coefficient Results for Teeth-on-Rotor And Teeth-on-Stator Labyrinth Gas Seals," *J. Eng. Gas. Turbines Power-Trans. ASME*, **108**(4), pp. 599-604.

[15] Childs, D. W. and Scharrer, J. K., 1988, "Theory Versus Experiment for The Rotordynamic Coefficients of Labyrinth Gas Seals .2. A Comparison to Experiment," *Journal of Vibration Acoustics Stress and Reliability in Design-Transactions of the Asme*, **110**(3), pp. 281-287.

[16] Soto, E. A. and Childs, D. W., 1999, "Experimental rotordynamic coefficient results for (a) a labyrinth seal with and without shunt injection and (b) a honeycomb seal," *J. Eng. Gas. Turbines Power-Trans. ASME*, **121**(1), pp. 153-159.

[17] Kwanka, K., 2000, "Dynamic Coefficients of Stepped Labyrinth Gas Seals," *Journal of Engineering for Gas Turbines and Power*, **122**(3), pp. 473-477.

[18] Wanger, N. G., Steff, K., Gausmann, R., and Schmidt, M., 2009, "Investigations on The Dynamic Coefficients of Impeller Eye Labyrinth Seals," Proc. *Proceedings of The Thirty-eighth Turbomachinery Symposium*, pp. 54-69.

[19] Wagner, N. G., Jongh, F. M. d., and Moffat, R., 2000, "Design, Testing, and Field Experience of A High-Pressure Natural Gas Reinjection Compressor," Proc. *Proceedings of 29th Turbomachinery Symposium*, Texas A&M University.

[20] Zhang, W., Yang, J., Cao, H., and Sun, D., 2011, "Experimental identification of fluid-induced force in labyrinth seals," *Journal of Mechanical Science and Technology*, **25**(10), pp. 2485-2494.

[21] Iwatsubo, T., 1980, "Evaluation of Instability Forces of Labyrinth Seals in Turbines or Compressors," Proc. *Proc. Rotordynamic Instability Problems in High Performance Turbomachinery*, NASA, pp. 139-167.

[22] Wyssmann, H. R., Pham, T. C., and Jenny, R. J., 1984, "Prediction of Stiffness and Damping Coefficients for Centrifugal Labyrinth Seal," *Journal of Engineering for Gas Turbines and Power*, **106**(4), pp. 920-926.

[23] Scharrer, J. K., 1988, "Theory Versus Experiment for The Rotordynamic Coefficients of Labyrinth Gas Seals .1. A 2 Control Volume Model," *Journal of Vibration Acoustics Stress and Reliability in Design-Transactions of the Asme*, **110**(3), pp. 270-280.

[24] Childs, D. W. and Scharrer, J. K., 1986, "An Iwatsubo-Based Solution for Labyrinth Seals: Comparison to Experimental Results," *Journal of Engineering for Gas Turbines and Power*, **108**(2), pp. 325-331.

[25] Kirk, R. G., 1990, "A Method for Calculating Labyrinth Seal Inlet Swirl Velocity," *Journal of Vibration and Acoustics-Transactions of the Asme*, **112**(3), pp. 380-383.

[26] Yücel, U., 2004, "Calculation of leakage and dynamic coefficients of stepped labyrinth gas seals," *Applied Mathematics and Computation*, **152**(2), pp. 521-533.

[27] Ha, T., 2001, "Rotordynamic analysis for stepped-labyrinth gas seals using Moody's friction-factor model," *Journal of Mechanical Science and Technology*, **15**(9), pp. 1217-1225.

[28] Eser, D. and Dereli, Y., 2007, "Comparisons of rotordynamic coefficients in stepped labyrinth seals by using Colebrook-White friction factor model," *Meccanica*, **42**(2), pp. 177-186.

[29] Picardo, A. and Childs, D. W., 2005, "Rotordynamic coefficients for a tooth-on-stator labyrinth seal at 70 bar supply pressures: Measurements versus theory and comparisons to a hole-pattern stator seal," *J. Eng. Gas. Turbines Power-Trans. ASME*, **127**(4), pp. 843-855.

[30] Rhode, D. L. and Sobolik, S. R., 1986, "Simulation of Subsonic Flow Through a Generic Labyrinth Seal," *Journal of Engineering for Gas Turbines and Power*, **108**(4), pp. 674-680.

[31] Rhode, D. L., Hensel, S. J., and Guidry, M. J., 1992, "Labyrinth Seal Rotordynamic Forces Using A 3-Dimensional Navier-Stokes Code," *Journal of Tribology-Transactions of the Asme*, **114**(4), pp. 683-689.

[32] Rhode, D. L., Hensel, S. J., and Guidry, M. J., 1993, "3-Dimensional Computaions of Rotordynamic Force Distributions in A Labyrinth Seal," *Tribology Transactions*, **36**(3), pp. 461-469.

[33] Ishii, E., Kato, C., Kikuchi, K., and Ueyama, Y., 1997, "Prediction of rotordynamic forces in a labyrinth seal based on three-dimensional turbulent flow computation," *Jsme International Journal Series C-Mechanical Systems Machine Elements and Manufacturing*, **40**(4), pp. 743-748.

[34] Moore, J. J., 2003, "Three-Dimensional CFD Rotordynamic Analysis of Gas Labyrinth Seals," *Journal of Vibration and Acoustics*, **125**(4), pp. 427-433.

[35] Kirk, R. G. and Guo, Z., 2004, "Calibration of Labyrinth Seal Bulk Flow Desing Analysis Predictions to CFD Simulation Results," Proc. *IMECHE 8th International Conference on Vibrations in Rotating Machinery*.

[36] Hirano, T., Guo, Z. L., and Kirk, R. G., 2005, "Application of computational fluid dynamics analysis for rotating machinery - Part II: Labyrinth seal analysis," *J. Eng. Gas. Turbines Power-Trans. ASME*, **127**(4), pp. 820-826.

[37] Kirk, R. G. and Guo, Z., 2009, "Influence of Leak Path Friction on Labyrinth Seal Inlet Swirl," *Tribology Transactions*, **52**(2), pp. 139-145.

[38] Huang, D. and Li, X., 2004, "Rotordynamic Characteristics of a Rotor with Labyrinth Gas Seals. Part 3: Coupled Fluid-Solid Vibration," *Proceedings of the Institution of Mechanical Engineers, Part A: Journal of Power and Energy* **218**(3), pp. 187-197.

[39] Huang, D. and Li, X., 2004, "Rotordynamic Characteristics of a Rotor with Labyrinth Gas Seals. Part 1: Comparison with Child's Experiments," *Proceedings of the Institution of Mechanical Engineers, Part A: Journal of Power and Energy* **218**(3), pp. 187-197.

[40] Huang, D. and Li, X., 2004, "Rotordynamic Characteristics of a Rotor with Labyrinth Gas Seals. Part 2: A Non-linear Model," *Proceedings of the Institution of Mechanical Engineers, Part A: Journal of Power and Energy* **218**(3), pp. 187-197.

[41] Wilcox, D. C., 2000, *Turbulence Modeling for CFD*, DCW Industries, Inc.

[42] ANSYS, 2010, *Release 12.1. Documentation for ANSYS CFX*.

[43] Spalart, P. R. and Shur, M., 1997, "On the Sensitization of Turbulence Models to Rotation and Curvature," *Aerospace Science Tech*, **1**(5), pp. 297-302.

[44] Guo, Z. and Kirk, R. G., 2005, "CFD Evaluation of Trubomachinery Secondary Flow Leak Path and Labyrinth Seal Entry Swirl," Proc. *ISCORMA-3 International Symposium on Stability Control of Rotating Machinery*, Bently Pressurized Bearing Company, pp. 1-11.

[45] Thompson, E. D., 2009, "Study of Forces and Dynamic Coefficients in Whirling and Eccentric Labyrinth Seals Using ANSYS-CFX," M.S., Virginia Tech, Blacksburg.

[46] Celik, I. B., Ghia, U., Roache, P. J., and Freitas, C. J., 2008, "Procedure for Estimation and Reporting of Uncertainty Due to Discretization in CFD Applications," *Journal of Fluids Engineering-Transactions of the Asme*, **130**(7), p. 078001.

[47] Roache, P. J., 1997, "Quantification of uncertainty in computational fluid dynamics," *Annual Review of Fluid Mechanics*, **29**(1), pp. 123-160.

[48] Iwatsubo, T. and Sheng, B. C., 1995, "Evaluation of Seal Effects on the Stability of Rotating Fluid Machinery," *International Journal of Rotating Machinery*, **1**(2), pp. 145-152.

[49] DyRoBeS, 2009, *Release 13.01. Documentation for DyRoBeS*, Eigen Technologies, Inc.

[50] Chen, W. J. and Gunter, E. J., 2005, *Introduction to Dynamics of Rotor-Bearing Systems*, Trafford.

Appendix A—Grid Study

The grid study has been introduced in detail in section 2.5 taking the straight eye seal as an example. In the Appendix 1, all the grid study results for the stepped eye seal and the balance drum seal will be presented in the forms of figure and table. Please refer to the section 2.5 for detailed explanation and calculation process, which are the same for the three seals.

A1.1 Grid Study on the Stepped Eye Seal

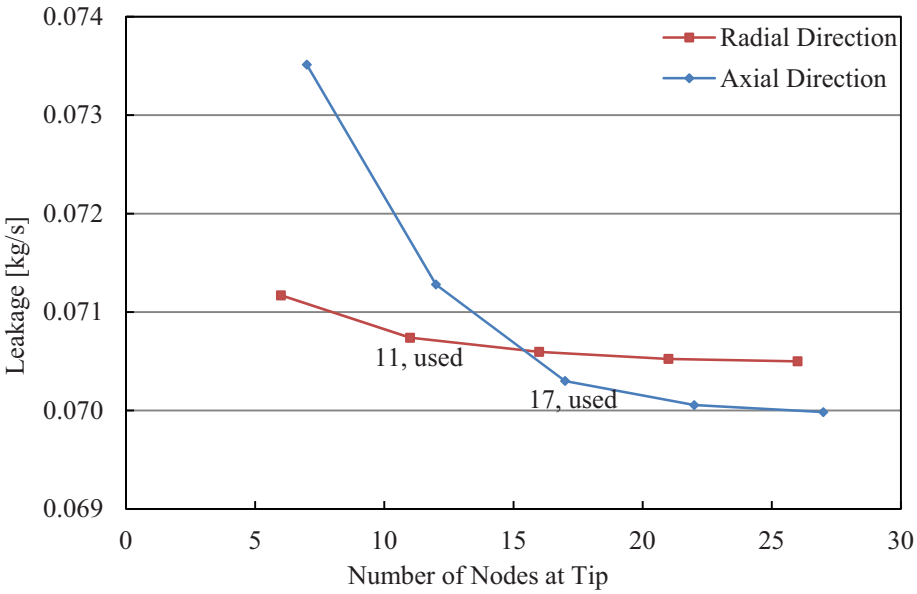

Figure A1-1 Grid independence study of nodes at tooth tip for the stepped eye seal

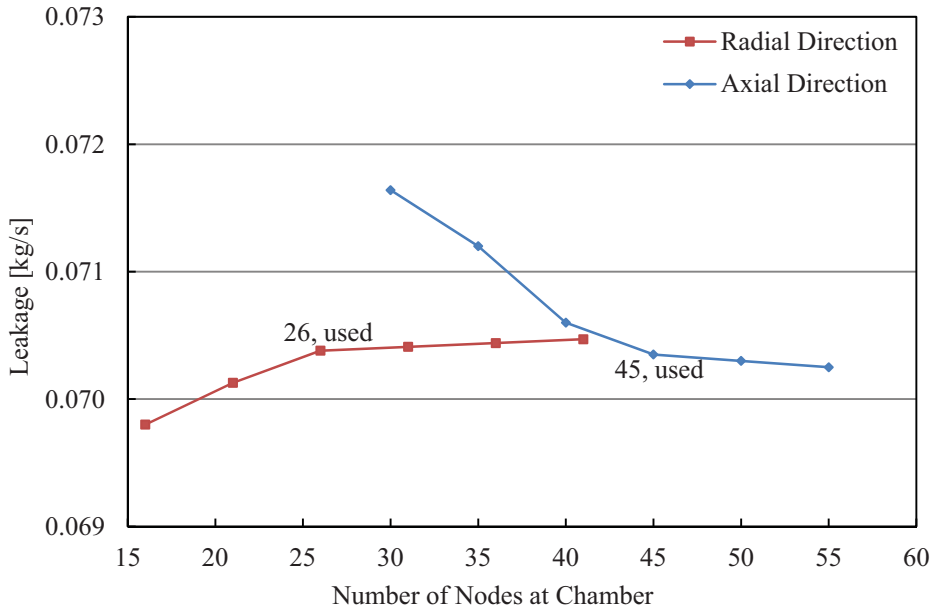

Figure A1-2 Grid independence study of nodes at chamber for the stepped eye seal

Table A1-1 Comparison of the three meshes in each chamber for the stepped eye seal

	Number of elements, *N*	**Average grid size, *h* (mm)**	**Refinement factor, *r***
Course	1505	0.211	1.30
Medium (used)	2540	0.163	1.32
Fine	4409	0.123	

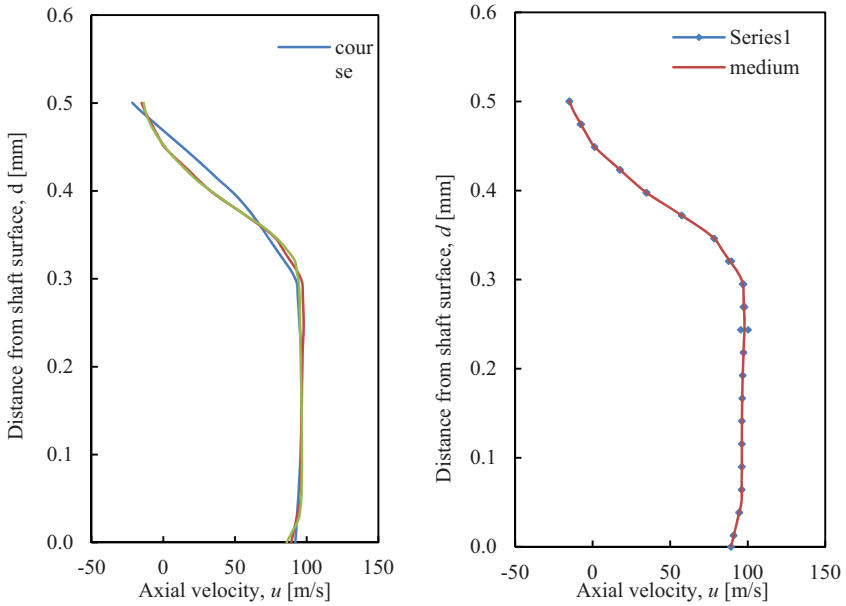

Figure A1-3 Axial velocity profile at the 1st tooth and errors for the stepped eye seal

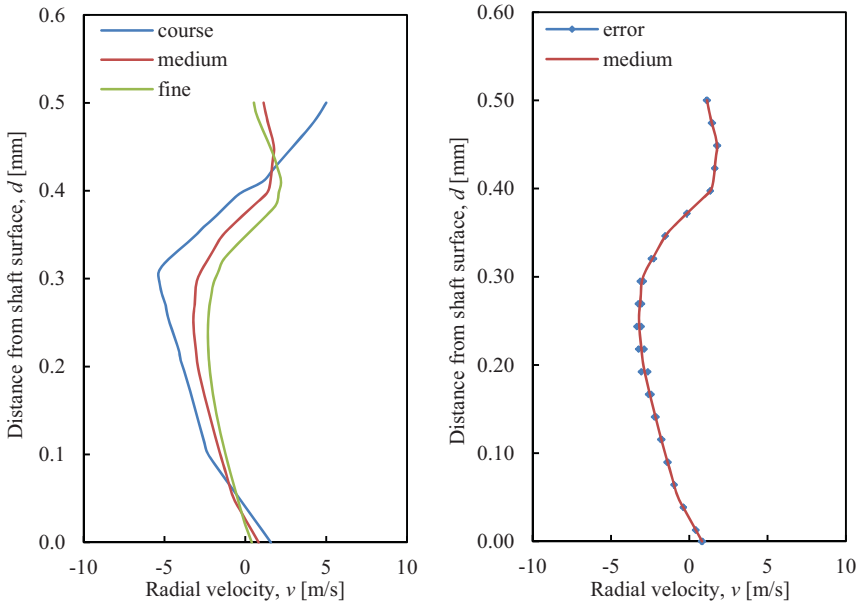

Figure A1-4 Radial velocity profile at the 1st tooth and errors for the stepped eye seal

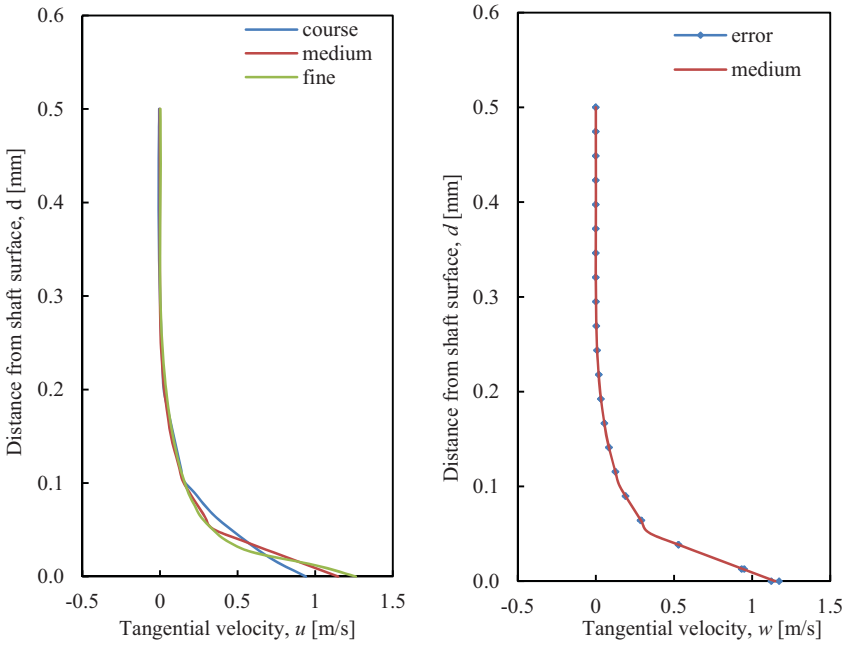

Figure A1-5 Tangential velocity profile at the 1st tooth and errors for the stepped eye seal

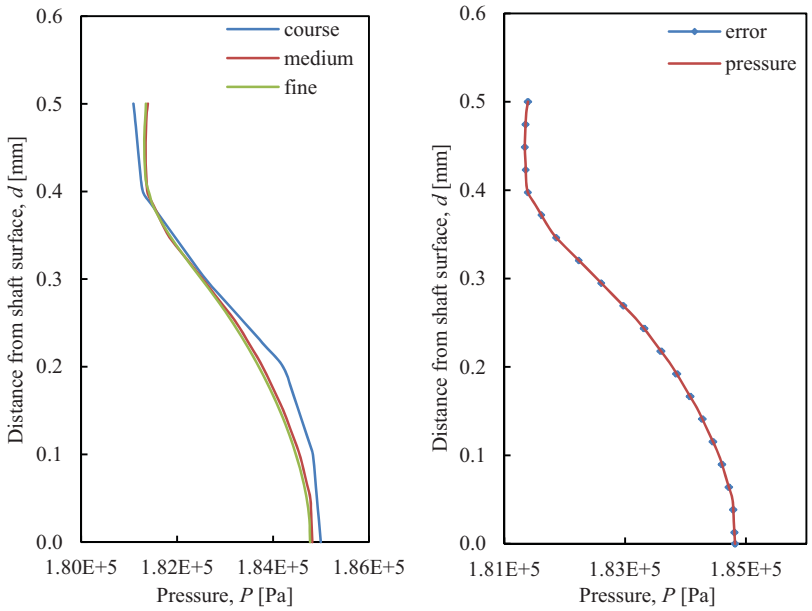

Figure A1-6 Pressure profile at the 1st tooth and errors for the stepped eye seal

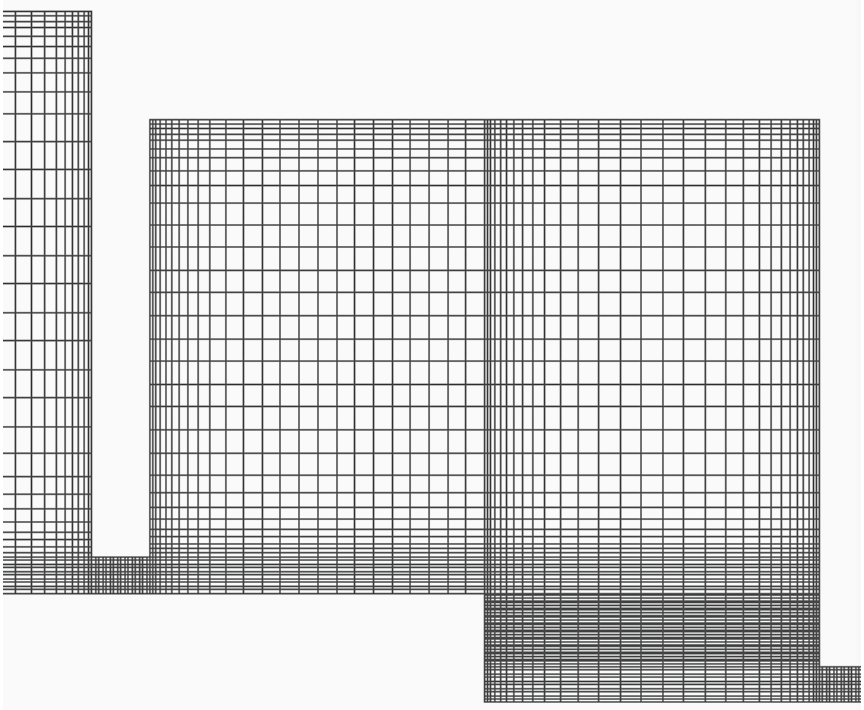

Figure A1-7 Mesh used for the stepped eye seal

A1.2 Grid Study on the Balance drum Seal

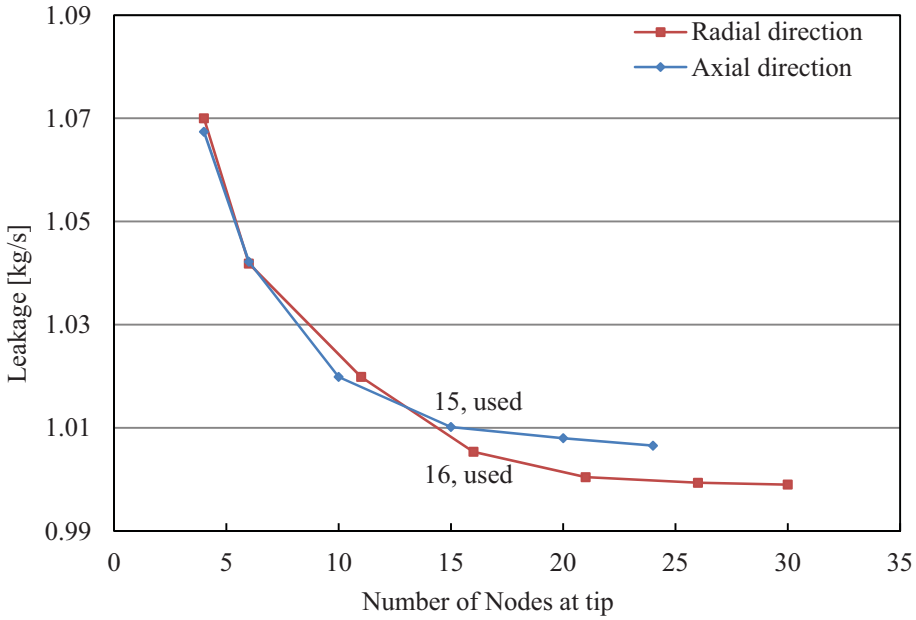

Figure A1-8 Grid independence study of nodes at tip for the balance drum seal

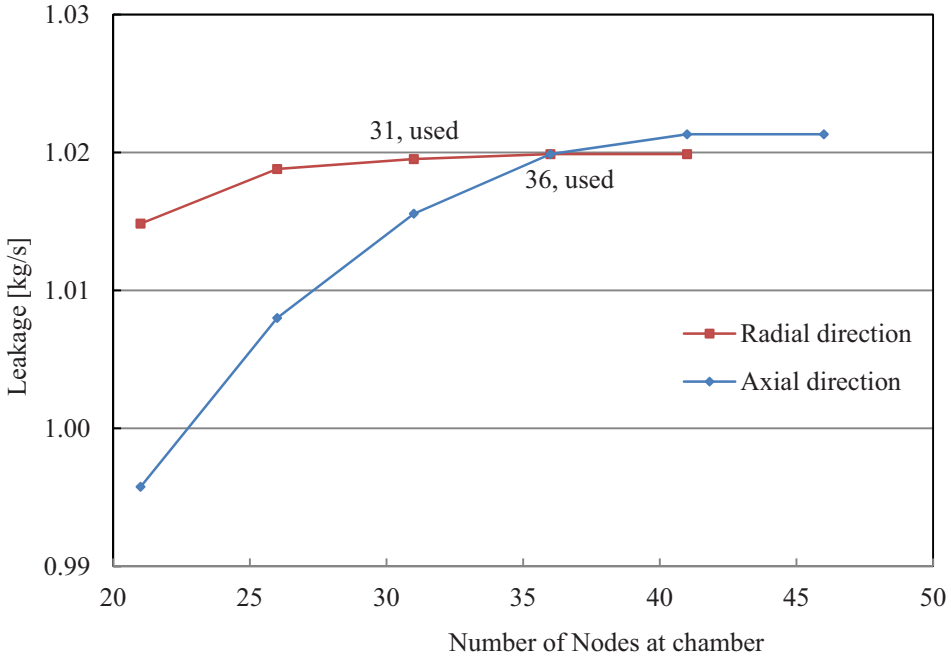

Figure A1-9 Grid independence study of nodes at chamber for the balance drum seal

Table A1-2 Comparison of the three meshed in each chamber for the balance drum seal

	Number of elements, *N*	**Average grid size, *h* (mm)**	**Refinement factor, *r***
Course	1376	0.087	1.30
Medium (used)	2325	0.067	
Fine	4000	0.051	1.31

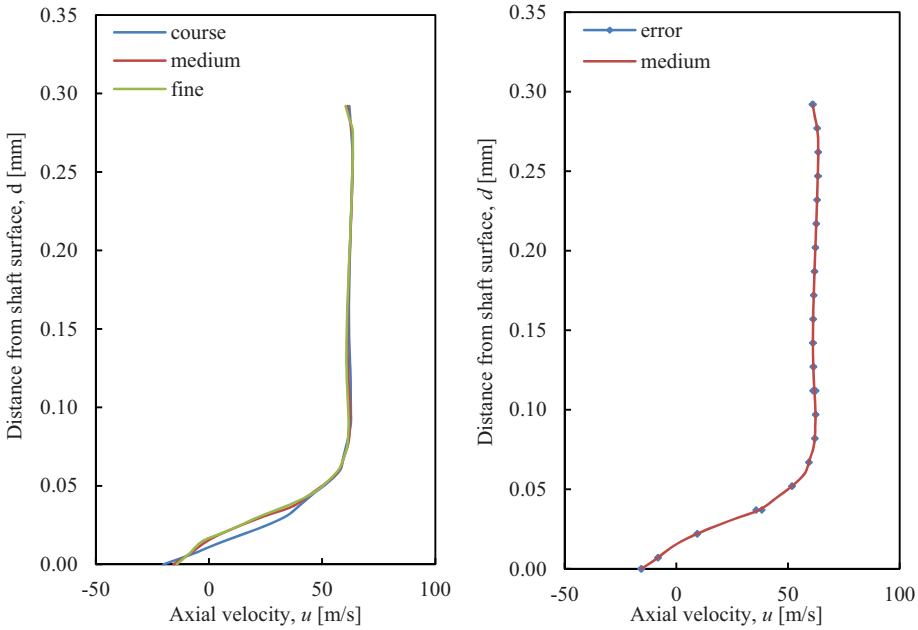

Figure A1-10 Axial velocity profile at the 1st tooth and errors for the balance drum seal

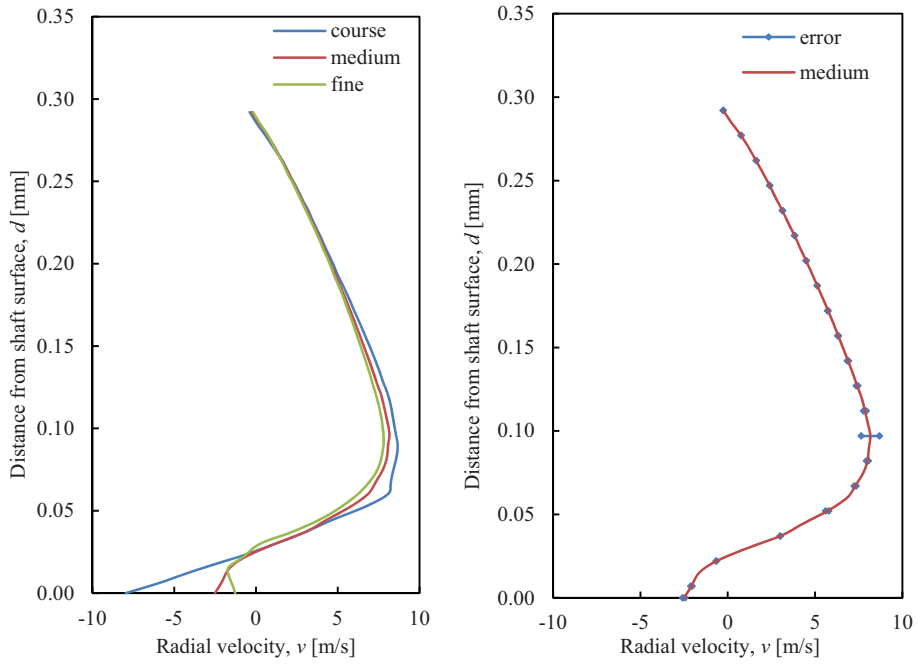

Figure A1-11 Radial velocity profile at the 1st tooth and errors for the balance drum seal

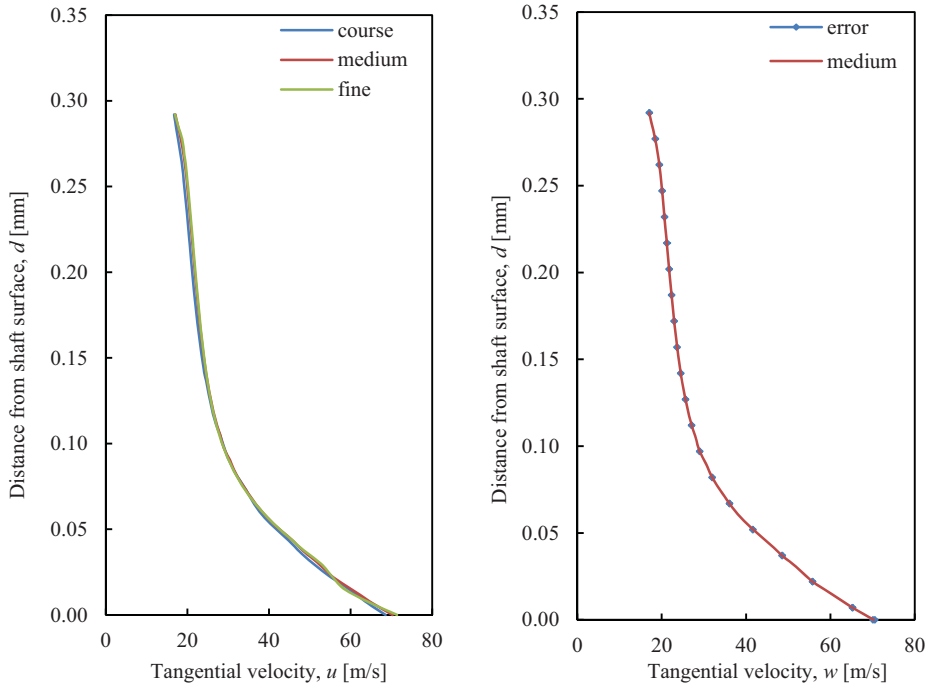

Figure A1-12 Tangential velocity profile at the 1st tooth and errors for the balance drum seal

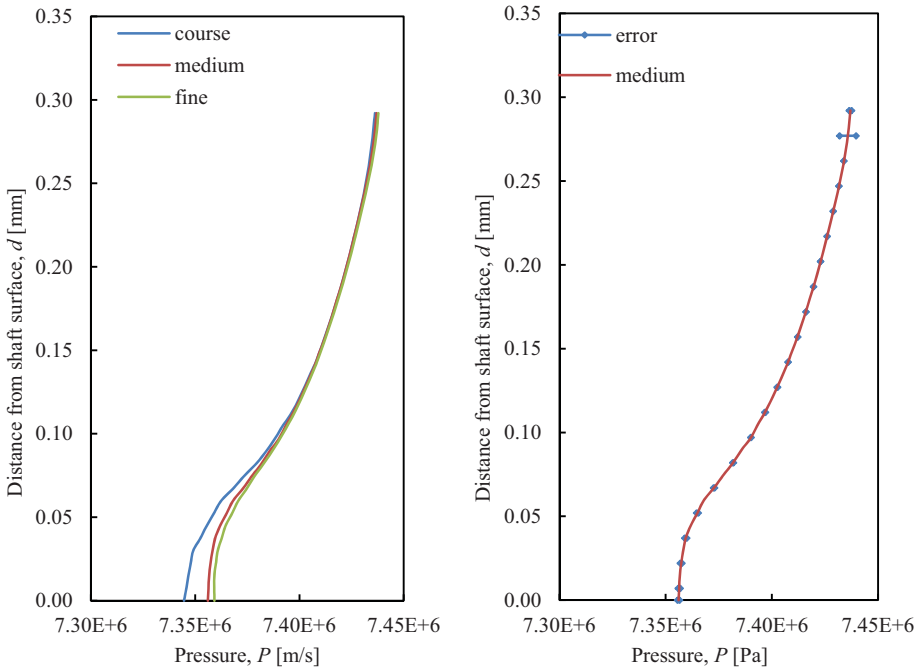

Figure A1-13 Pressure profile at the 1st tooth and errors for the balance drum seal

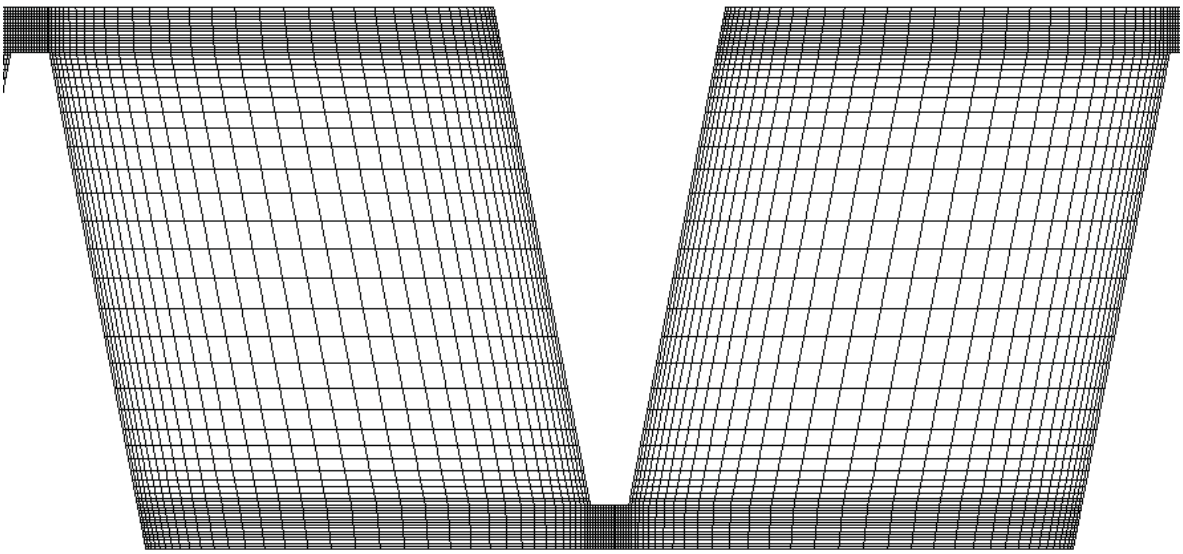

Figure A1-14 Mesh used for the balance drum seal for the balance drum seal

Appendix B—Predicted Seal Coefficients

Table A2-1 Predicted rotordynamic coefficients at different pre-swirl rates (tooth-on-stator, 0.1 eccentricity)

Pre-swirl Rate	Direct Stiffness *K* (N/m)		Cross-coupled Damping *c* (N·s/m)		Cross-coupled Stiffness *k* (N/m)		Direct Damping *C* (N·s/m)	
	1st order model	2st order model	1st order model	2st order model	1st order model	2st order model	1st order model	2st order model
3.00%	6.01E+06	6.22E+06	1.33E+03	1.21E+02	8.56E+05	7.60E+05	1.89E+03	2.55E+03
17.2%	5.54E+06	5.75E+06	1.21E+03	2.46E+02	2.30E+05	1.27E+05	2.36E+03	3.07E+03
46.8%	6.11E+06	6.48E+06	5.41E+02	2.00E+03	1.14E+06	1.42E+06	3.51E+03	5.44E+03
62.7%	6.48E+06	7.03E+06	2.31E+02	4.06E+03	2.31E+06	2.58E+06	4.08E+03	5.93E+03
73.6%	6.92×106	7.59E+06	1.16E+03	5.79E+03	3.01E+06	3.31E+06	4.25E+03	6.29E+03

Note: this table is plotted in Figure 4-6 and Figure 4-7

Table A2-2 Predicted rotordynamic coefficients at different eccentricities (tooth-on-stator)

Eccentricity	Direct Stiffness *K* (N/m)		Cross-coupled Damping *c* (N·s/m)		Cross-coupled Stiffness *k* (N/m)		Direct Damping *C* (N·s/m)	
	3% pre-swirl rate	73.6% pre-swirl rate	3% pre-swirl rate	73.6% pre-swirl rate	3% pre-swirl rate	73.6% pre-swirl rate	3% pre-swirl rate	73.6% pre-swirl rate
0.1	6.22E+06	7.59E+06	1.21E+02	5.79E+03	7.60E+05	3.31E+06	2.55E+03	6.29E+03
0.3	6.11E+06	7.46E+06	5.00E+02	5.40E+03	6.95E+05	3.18E+06	2.80E+03	6.03E+03
0.5	6.05E+06	7.07E+06	8.97E+02	5.00E+03	7.33E+05	2.32E+06	2.95E+03	4.97E+03
0.7	5610000	6.14E+06	9.98E+02	4.29E+03	7.78E+05	2.00E+06	2.85E+03	3.85E+03

Note: this table is plotted in Figure 4-13, Figure 4-14, Figure 4-15, and Figure 4-16

Table A2-3 Predicted rotordynamic coefficients at different clearances (tooth-on-stator, 0.1 eccentricity)

Clearance (μm)	Direct Stiffness K (N/m)		Cross-coupled Damping c (N·s/m)		Cross-coupled Stiffness k (N/m)		Direct Damping C (N·s/m)	
	3% pre-swirl rate	73.6% pre-swirl rate	3% pre-swirl rate	73.6% pre-swirl rate	3% pre-swirl rate	73.6% pre-swirl rate	3% pre-swirl rate	73.6% pre-swirl rate
146	3.66E+06	5.65E+06	1.11E+03	4.61E+03	1.14E+06	3.29E+06	4.02E+03	8.72E+03
292	6.22E+06	7.59E+06	1.21E+02	5.79E+03	7.60E+05	3.31E+06	2.55E+03	6.29E+03
438	7.74E+06	7.22E+06	8.42E+02	1.16E+03	5.21E+05	2.41E+06	2.22E+03	6.56E+03

Note: this table is plotted in Figure 4-21, Figure 4-22, Figure 4-23 and Figure 4-24

Table A2-4 Predicted rotordynamic coefficients at different pre-swirl rates (tooth-on-rotor, 0.1 eccentricity)

Pre-swirl Rate	Direct Stiffness K (N/m)		Cross-coupled Damping c (N·s/m)		Cross-coupled Stiffness k (N/m)		Direct Damping C (N·s/m)	
	1st order model	2st order model	1st order model	2st order model	1st order model	2st order model	1st order model	2st order model
11.3%	6.08E+06	6.18E+06	1.52E+02	5.57E+02	1.36E+04	6.51E+04	2.34E+03	2.69E+03
37.7%	7.48E+06	8.16E+06	1.72E+03	6.39E+03	3.03E+06	3.70E+06	4.85E+03	9.46E+03
54.6%	7.74E+06	8.64E+06	2.01E+03	8.27E+03	6.03E+06	6.68E+06	6.98E+03	1.15E+04
75.3%	8.41E+06	9.39E+06	2.91E+03	9.66E+03	7.72E+06	8.82E+06	7.68E+03	1.53E+04

Note: this table is plotted in Figure 4-27 and Figure 4-28

Table A2-5 Predicted rotordynamic coefficients at different pre-swirl rates (Stepped Eye Seal)

Pre-swirl Rate	Direct Stiffness K (N/m)		Cross-coupled Damping c (N·s/m)		Cross-coupled Stiffness k (N/m)		Direct Damping C (N·s/m)	
	1st order model	2st order model	1st order model	2st order model	1st order model	2st order model	1st order model	2st order model
0.68	8.07E+03	8.70E+03	1.17E+02	4.88E+01	8.65E+02	4.42E+02	6.35E+01	2.04E+01
7.70	1.15E+04	1.26E+04	5.68E+01	1.67E+02	1.94E+04	2.02E+04	1.22E+02	2.01E+02
14.15	1.55E+04	1.76E+04	1.47E+02	3.59E+02	5.17E+04	5.31E+04	2.72E+02	4.10E+02
20.27	2.11E+04	2.46E+04	2.96E+02	6.62E+02	8.49E+04	8.71E+04	4.39E+02	6.62E+02

Note: this table is plotted in Figure 4-30, Figure 4-31, Figure 4-32, and Figure 4-33

Table A2-6 Predicted rotordynamic coefficients at different pre-swirl rates (Balance Drum Seal)

Pre-swirl Rate	Direct Stiffness K (N/m)		Cross-coupled Damping c (N·s/m)		Cross-coupled Stiffness k (N/m)		Direct Damping C (N·s/m)	
	1st order model	2st order model	1st order model	2st order model	1st order model	2st order model	1st order model	2st order model
13.60%	4.12E+06	4.34E+06	2.80E+03	4.26E+03	6.92E+05	3.49E+05	5.55E+03	7.91E+03
31.60%	5.29E+06	5.90E+06	3.65E+03	7.84E+03	2.91E+06	3.07E+06	7.80E+03	1.33E+04
75.00%	7.60E+06	8.90E+06	5.44E+03	1.44E+04	8.60E+06	1.03E+07	1.13E+04	2.27E+04

Note: this table is plotted in Figure 4-34, Figure 4-35, Figure 4-36, and Figure 4-37